Novel infrared solid-state lasers based on lanthanide doped crystalline materials

SAMI SLIMI

ADVERTIMENT. L'accés als continguts d'aquesta tesi doctoral i la seva utilització ha de respectar els drets de la persona autora. Pot ser utilitzada per a consulta o estudi personal, així com en activitats o materials d'investigació i docència en els termes establerts a l'art. 32 del Text Refós de la Llei de Propietat Intel·lectual (RDL 1/1996). Per altres utilitzacions es requereix l'autorització prèvia i expressa de la persona autora. En qualsevol cas, en la utilització dels seus continguts caldrà indicar de forma clara el nom i cognoms de la persona autora i el títol de la tesi doctoral. No s'autoritza la seva reproducció o altres formes d'explotació efectuades amb finalitats de lucre ni la seva comunicació pública des d'un lloc aliè al servei TDX. Tampoc s'autoritza la presentació del seu contingut en una finestra o marc aliè a TDX (framing). Aquesta reserva de drets afecta tant als continguts de la tesi com als seus resums i índexs.

ADVERTENCIA. El acceso a los contenidos de esta tesis doctoral y su utilización debe respetar los derechos de la persona autora. Puede ser utilizada para consulta o estudio personal, así como en actividades o materiales de investigación y docencia en los términos establecidos en el art. 32 del Texto Refundido de la Ley de Propiedad Intelectual (RDL 1/1996). Para otros usos se requiere la autorización previa y expresa de la persona autora. En cualquier caso, en la utilización de sus contenidos se deberá indicar de forma clara el nombre y apellidos de la persona autora y el título de la tesis doctoral. No se autoriza su reproducción u otras formas de explotación efectuadas con fines lucrativos ni su comunicación pública desde un sitio ajeno al servicio TDR. Tampoco se autoriza la presentación de su contenido en una ventana o marco ajeno a TDR (framing). Esta reserva de derechos afecta tanto al contenido de la tesis como a sus resúmenes e índices.

WARNING. Access to the contents of this doctoral thesis and its use must respect the rights of the author. It can be used for reference or private study, as well as research and learning activities or materials in the terms established by the 32nd article of the Spanish Consolidated Copyright Act (RDL 1/1996). Express and previous authorization of the author is required for any other uses. In any case, when using its content, full name of the author and title of the thesis must be clearly indicated. Reproduction or other forms of for profit use or public communication from outside TDX service is not allowed. Presentation of its content in a window or frame external to TDX (framing) is not authorized either. These rights affect both the content of the thesis and its abstracts and indexes.

UNIVERSITAT ROVIRA i VIRGILI

Novel infrared solid-state lasers based on lanthanide-doped crystalline materials

SAMI SLIMI

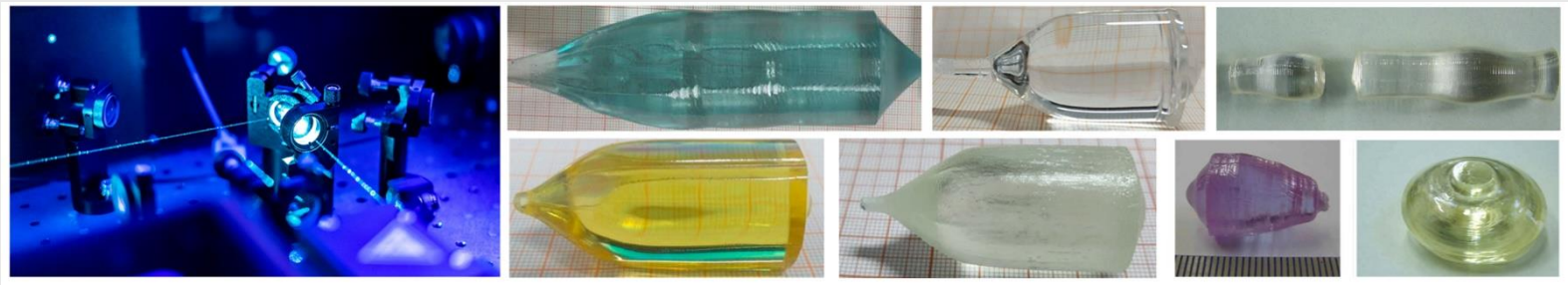

Doctoral Thesis
2024

UNIVERSITAT ROVIRA I VIRGILI
Novel infrared solid-state lasers based on lanthanide doped crystalline materials
SAMI SLIMI

Novel infrared solid-state lasers based on lanthanide-doped crystalline materials

---

SAMI SLIMI

DOCTORAL THESIS

Supervised by:

Prof. Dr. Xavier Mateos Ferré
Dr. Rosa Maria Solé Cartañà

Departament de Química Física i Inorgànica
Física i Cristal·lografia de Materials (FiCMA)

UNIVERSITAT ROVIRA i VIRGILI

Tarragona
2024

UNIVERSITAT ROVIRA I VIRGILI
Novel infrared solid-state lasers based on lanthanide doped crystalline materials
SAMI SLIMI

Novel infrared solid-state lasers based on lanthanide-doped crystalline materials

SAMI SLIMI

©Sami Slimi, 2024
Física i Cristal·lografia de Materials (FiCMA)
Departament de Química Física i Inorgànica
Universitat Rovira i Virgili
C/ Marcel·lí Domingo, 1 E-43007, Tarragona, Spain

UNIVERSITAT ROVIRA I VIRGILI
Novel infrared solid-state lasers based on lanthanide doped crystalline materials
SAMI SLIMI

UNIVERSITAT ROVIRA i VIRGILI

FAIG CONSTAR que aquest treball, titulat "**Nous làsers d'estat sòlid a l'infraroig proper en materials cristal·lins dopats amb ions lantànids**", que presenta **Sami Slimi** per a l'obtenció del títol de Doctor, ha estat realitzat sota la meva direcció al Departament **Química Física i Inorgànica** d'aquesta universitat.

HAGO CONSTAR que el presente trabajo, titulado "**Nuevos láseres de estado sólido en el infrarrojo basados en materiales cristalinos dopados con iones lantánidos**", que presenta **Sami Slimi** para la obtención del título de Doctor, ha sido realizado bajo mi dirección en el Departamento de **Química Física e Inorgánica** de esta universidad.

I STATE that the present study, entitled "**Novel infrared solid-state lasers based on lanthanide-doped crystalline materials**", presented by **Sami Slimi** for the award of the degree of Doctor, has been carried out under my supervision at the Department of **Physical and Inorganic Chemistry** of this university.

[Tarragona], [15-08-2024]

El/s director/s de la tesi doctoral
El/los director/es de la tesis doctoral
Doctoral Thesis Supervisor/s

[signature]

Xavier Mateos Ferré

[signature]

Rosa Maria Solé Cartañà

UNIVERSITAT ROVIRA I VIRGILI
Novel infrared solid-state lasers based on lanthanide doped crystalline materials
SAMI SLIMI

[ENG]

Novel infrared solid-state lasers based on lanthanide-doped crystalline materials

– SAMI SLIMI –

Abstract

The main objective of this thesis work was the development of innovative and efficient diode-pumped solid-state lasers operating in the continuous-wave and passively *Q*-switched operation regimes in the near-infrared spectral range at ~1 μm and ~2 μm. For this purpose, laser crystals doped with ytterbium (Yb^{3+}) and neodymium (Nd^{3+}) were selected operating at ~1 μm, while other crystals doped with thulium (Tm^{3+}) and holmium (Ho^{3+}) were chosen for lasers at ~2 μm. Several crystalline materials from different crystals families were studied, such us garnet crystals (mixed aluminate garnets and gallium garnet matrices), double molybdates, oxoborates and fluorides, due to their ability to generate stable laser emission, their large interatomic distance favouring high doping levels with minimum luminescence quenching, and their high absorption and emission cross-sections. Different crystal growth methods used to develop the studied crystals are reported. In addition, deep investigation on their physicochemical, microstructural, and spectroscopic properties is presented. The laser experiments are reported at room temperature for most of the studied gain media and at cryogenic temperature for a special case of crystals.

Keywords: Crystal growth; Solid-state lasers; Nd^{3+}, Yb^{3+}, Tm^{3+} and Ho^{3+}- doped crystalline materials; Optical spectroscopy; Optical absorption; Luminescence; Near infrared laser; Diode-pumped laser.

[ESP]

Nuevos láseres de estado sólido en el infrarrojo basados en materiales cristalinos dopados con iones lantánidos

– SAMI SLIMI –

Resumen

El objetivo principal de este trabajo de tesis fue el desarrollo de láseres de estado sólido bombeados por diodos, innovadores y eficientes, que operan en los regímenes de operación de onda continua y conmutación Q pasiva en el rango espectral del infrarrojo cercano a aproximadamente 1 μm y 2 μm. Con este propósito, se eligieron cristales láser dopados con iterbio (Yb^{3+}) y neodimio (Nd^{3+}) que operan ~1 μm, y otros cristales dopados con tulio (Tm^{3+}) y holmio (Ho^{3+}) para láseres con emisión a ~2 μm. Se han estudiado varios materiales cristalinos de diferentes familias de cristales, tales como cristales de granate (granates de aluminato mixto y matrices de granate de galio), molibdatos dobles, oxoboratos y fluoruros, debido a su capacidad para generar una emisión láser estable, su gran distancia interatómica que favorece altos niveles de dopaje con mínimo bloqueo de luminiscencia, y sus altas secciones transversales de absorción y emisión. Se detallan los diferentes métodos de crecimiento de cristales utilizados para desarrollar los cristales estudiados, así como una profunda investigación de sus propiedades fisicoquímicas, microestructurales y espectroscópicas. Los experimentos láser se realizaron a temperatura ambiente para la mayoría de los medios activos estudiados y a temperatura criogénica para un caso especial de cristales.

Palabras clave: Crecimiento de cristales; Láseres de estado sólido; Materiales cristalinos dopados con Nd^{3+}, Yb^{3+}, Tm^{3+} y Ho^{3+}; Espectroscopía óptica; Absorción óptica; Luminiscencia; Láser de infrarrojo cercano; Láser bombeado por diodos.

[CAT]

Nous làsers `d'estat sòlid a l'infraroig proper en materials cristal·lins dopats amb ions lantànids

– SAMI SLIMI –

Resum

L'objectiu principal d'aquest treball de tesi ha sigut el desenvolupament de làsers d'estat sòlid novedosos i eficients bombats per díodes que operin en els règims tant d'ona contínua com de commutació del factor *Q* de forma passiva en el rang d'infraroig proper, al voltant de ~1 μm i ~2 μm. Amb aquest propòsit, es van triar cristalls làser dopats amb iterbi (Yb^{3+}) i neodimi (Nd^{3+}) que operen al voltant d' 1 μm, i altres cristalls dopats amb tul·li (Tm^{3+}) i holmi (Ho^{3+}) per a làsers amb emissió al voltant de 2 μm. S'han estudiat diversos materials cristal·lins de diferents famílies de cristalls, com ara cristalls de granat (granats d'aluminat mixte i matrius de granat de gal·li), molibdats dobles, oxoborats i fluorurs, degut a la seva capacitat per generar una emissió làser estable, la seva gran distància interatòmica que afavoreix alts nivells de dopatge amb mínim bloqueig de luminiscència, i les seves altes seccions transversals d'absorció i emissió. Es detallen els diferents mètodes de creixement de cristalls utilitzats per obtenir els cristalls estudiats, així com una profunda investigació de les seves propietats fisicoquímiques, microestructurals i espectroscòpiques. Els experiments làser es van realitzar a temperatura ambient per a la majoria dels medis actius estudiats i a temperatura criogènica per a un cas especial de cristalls.

Paraules clau: Creixement de cristalls ; Làsers d'estat sòlid ; Materials cristal·lins dopats amb Nd^{3+}, Yb^{3+}, Tm^{3+} i Ho^{3+}; Espectroscòpia òptica ; Absorció òptica; Luminescència, Làser d'infraroig proper ; Làser bombat per díode.

UNIVERSITAT ROVIRA I VIRGILI
Novel infrared solid-state lasers based on lanthanide doped crystalline materials
SAMI SLIMI

Preface

This Ph.D. research, documented in this thesis, was conducted within the Física i Cristal·lografia de Materials (FiCMA) group at the Department of Physical and Inorganic Chemistry, Universitat Rovira i Virgili, Tarragona, Spain. It was supervised by Dr. Prof. Xavier Mateos Ferré and Dr. Rosa Maria Solé Cartañà.

This thesis has been carried out in collaboration with the following groups and researchers:

- Dr. Valentin Petrov, Dr. Uwe Griebner and Dr. Weidong Chen at the Max-Born Institute for Nonlinear Optics and Short Pulse Spectroscopy (Berlin, Germany),
- Dr. Pavel Loiko and Prof. Patrice Camy at the CIMAP laboratory, Université de Caen (Caen, France),
- Dr. Venkatesan Jambunathan, Dr. Martin Smrz and Prof. Tomas Mocek at the HILASE Center, Institute of Physics ASCR (Dolní Brezany, Czech Republic), and
- Dr. Haohai Yu and Dr. Huaijin Zhang at Fujian Institute of Research on the Structure of Matter, Chinese Academy of Sciences (Fujian, China).

This work was financially supported by

Agencia de Gestió d'Ajuts Universitaries i de Recerca, AGAUR, de la Generalitat de Catalunya through the fellowships 2022FI_B200021, 2021FI_B100170 and 2020FI_B00522.

Spanish Government (PID2019-108543RB-I00) and (PID2022-141499OB-I00)

Sami Slimi
Tarragona, 2024

UNIVERSITAT ROVIRA I VIRGILI
Novel infrared solid-state lasers based on lanthanide doped crystalline materials
SAMI SLIMI

Acknowledgments

Firstly, I would like to express my deepest gratitude to my thesis advisors, Prof. Dr. Xavier Mateos and Dr. Rosa Maria Solé. Their guidance, support, and expertise have been fundamental throughout the course of my research. Their insightful feedback, encouragement, and dedication have greatly enriched this work and helped me navigate the complexities of my study. I am profoundly grateful for the time they invested in mentoring me and for their unwavering commitment to my academic and professional growth. This achievement would not have been possible without their invaluable contributions and mentorship.

I would also like to express my sincere gratitude to Prof. Dr. Magdalena Aguiló and Prof. Dr. Francesc Díaz. Their leadership and vision have been instrumental in shaping the research environment that has greatly contributed to the success of my work.

My thesis work was also greatly support from Dr. Pavel Loiko and Dr. Venkatesan Jambunathan. I am deeply thankful for the insightful discussions and assistance they provided during my time in the laboratory, as well as their help through email correspondence.

I am deeply thankful to Dr. Valentin Petrov for providing me with the opportunity to work at the Max Born Institute in Germany and to Prof. Tomas Mocek for welcoming me into the Hilase laboratories in the Czech Republic during my research visit. I would also like to express my appreciation to Dr. Weidong Chen.

I would also like to extend my thanks to my friends and colleagues in the FiCMA lab—Ghassen, Antonio, Moha, Zhonghuan, and David. The incredible moments we shared will always be unforgettable. A special thanks goes to Nicole and Gemma as well. This team truly felt like a second family to me.

I want to give a heartfelt thanks to my girlfriend Abir for her unwavering support throughout these years and wish her all the best with her own thesis. After a long period of being apart, you followed me to Spain, and now that we're here together, let's build a wonderful future for ourselves.

I want to express my deepest gratitude to my parents for their unwavering belief in me, their countless sacrifices, and their unconditional love. From my earliest days through to the major milestones I've achieved, their steadfast support and encouragement have been an unceasing source of strength and motivation. Their sacrifices have laid the foundation for my success, and their belief in me has fueled my determination. I hope that this achievement brings some comfort to my mother, who has always been my emotional anchor, especially given the distance between us now. Despite the physical separation, their love and support have been a constant presence in my life, guiding me and inspiring me every step of the way.

I want to offer my sincere gratitude to my brothers, Aymen and Engineer Chaouki (or as I affectionately call him, Chakchouk), for their steadfast support and encouragement throughout this journey. I wish them both a long, fulfilling life and all the best in everything they do. Finaly, I would like to dedicate this section to the memory of my beloved brother, Moez. His presence and influence remain deeply missed. Although he is no longer with us, his legacy of resilience and love lives on in everything I do. This achievement is as much his as it is mine, and I hope to honor his memory by making the most of the opportunities he believed in for me.

UNIVERSITAT ROVIRA I VIRGILI
Novel infrared solid-state lasers based on lanthanide doped crystalline materials
SAMI SLIMI

Contents

CHAPTER 1

CHAPTER 1: General introduction and Overview

1.1 Introduction

The rapid advancement of infrared laser technology has led to its extensive application across various sectors. Near-infrared (NIR) lasers are employed in many areas of applications such as laser weaponry, clinical surgery, precision manufacturing, and secure communications, spectral analysis and spectroscopy, medical therapies, and remote sensing technologies [1–9].

A key element for the development of innovative applications and devices in NIR spectral ranges is the laser sources by continuous improved characteristics in terms of spectral and temporal ranges, power, efficiency, and stability of the output signal. Material science is in the heart of the laser development in the sense that the main element of lasers is the active medium. This active material can be of different nature: a gas or liquid, also it can be based on semiconductors or on rare-earth (RE) or transition-metal -doped dielectric materials. Such matrices in laser technology may possess crystalline, amorphous like glasses, or ceramic structures and can be shaped into various forms such as bulk crystals and glasses, thin films (crystalline or glassy), or optical fibers. Diverse techniques for producing IR lasers are facilitated by effectively employing these active media, such as i) semiconductor quantum cascade lasers, which are notable for their compact size and efficiency despite their complex architecture and limitations in output power and beam quality, ii) free electron lasers, although bulky and expensive, they can achieve high power and offer tunability, iii) chemical lasers that produce high-energy output with superior beam quality using chemical reactions, but they necessitate costly materials and generate harmful byproducts, iv) frequency-doubling lasers that offer a broad tuning range and high frequencies down to the deep UV, yet their intricate designs contribute to prohibitive costs and, v) solid-state lasers, including, among others, the slab and thin-disk geometries that utilize a straightforward mechanism to deliver high-power and efficient laser performance.

Solid-state lasers fall into two primary categories, differentiated by their gain medium: those using rare earth (RE) ions (referred sometimes as lanthanide ions (Ln)) and those using transition-metal (TM) ions. Lasers doped with TM ions typically struggle with inadequate pumping sources and difficulties in achieving high-energy outputs at standard room temperature, primarily because of the quick decay of the upper level laser [10–12]. In contrast, lasers utilizing RE ions such as Ce, Dy, Ho, Nd, Tm, Sm, Pr, Eu, Tb, Er, and Yb have demonstrated efficient laser output generation [13–17]. These ions feature elaborate energy level arrangements, enabling them to produce multiple emission signals and thereby allow for the building of lasers that operate across a range of wavelengths. NIR solid-state lasers, which incorporate REs are notable for their compact size, high energy conversion efficiency, excellent beam quality, wide range of tunability, and diverse modes of operation, making them a central subject of ongoing research in this field. Since the appearance of lasers, the pursuit of developing materials with appropriate structural, microstructural, physicochemical, spectroscopic, and optical qualities has been paramount, constituting the foundational elements of these devices. Concurrently, extensive research has been conducted worldwide on various methods to synthesize these types of laser materials. This includes efforts to grow bulk crystals and epitaxial crystalline thin films, as well as advancements in glass technology for developing new glass compositions and processes for crafting complex optical fiber designs. Progress in

materials science is crucial for broadening the selection of new crystal gain media available for NIR solid-state lasers.

Typically, laser emission in the near-infrared at ~1μm is achieved using solid-state materials doped with trivalent RE ions such as Yb (laser wavelength λ_L~1μm) or Nd (λ_L ~0.9, 1.06 and 1.3 μm). The Yb^{3+} ions, when doped into solid-state laser materials [18–21], provide several advantages over traditional other dopants. One of the key benefits is their simple electronic structure, which reduces non-radiative losses and results in high quantum efficiency. This simplicity also minimizes the effects of up-conversion and concentration quenching, allowing for higher doping concentrations and more efficient energy storage. The development and refinement of Yb-doped solid-state lasers have led to significant advances driven by their reliability, compact size, and capability to generate high power levels. The Nd^{3+} ions offer several laser lines in this spectral region from the $^4F_{3/2}$ upper laser level into the $^4I_{13/2}$, $^4I_{11/2}$, and $^4I_{9/2}$ manifolds. The strongest and most used laser transition $^4F_{3/2} \rightarrow {}^4I_{11/2}$ emits between 1050 and 1100 nm [21]. This wavelength is advantageous for a range of applications due to its ability to be efficiently absorbed and its relatively low interaction with atmospheric water vapor, making it ideal for long-distance transmission and precision tasks. Nd-doped solid-state lasers are well known for their high efficiency, good beam quality, and the ability to produce both continuous and pulsed outputs. These attributes make them invaluable in a variety of fields, including materials processing [22–24], where they are used for cutting, welding, and engraving; in the medical field for procedures like laser surgery and skin resurfacing; and in scientific research for spectroscopy and the pumping of other laser systems [25–27].

Tm and Ho -doped (or a combination (co-doping) of them) solid-state lasers are among the most efficient sources in the range of λ_L~1.9-2.1 μm. Based on the type of gain medium they can be bulk, fiber, slab, thin-disk or waveguide lasers. Trivalent Tm^{3+} and Ho^{3+} ions, when doped into suitable host materials, can be excited into higher energy states by various pumping sources such as diode lasers and fiber lasers. These excited ions then emit laser in the ~2 μm region through radiative transitions between specific electronic states. The choice of the host material, typically crystals or ceramics, and the doping concentration are critical to achieving desired laser properties like tunability of emission wavelength and high slope efficiencies. Such 2 μm lasers are extremely versatile. In medical applications, they are used for cutting and ablating soft tissues with high precision and minimal collateral damage, which is crucial in surgeries. In environmental monitoring, these lasers serve as powerful tools for detecting gases and pollutants through differential absorption lidar techniques.

The goal of this thesis work was to develop novel inorganic crystal materials doped with RE ions and explore their efficiency for lasers, at room and cryogenic temperatures, in the NIR range at ~1μm using Nd^{3+} and Yb^{3+} ions, and in the ~1.9-2.1 μm range using Tm^{3+} and Ho^{3+} ions. To achieve this, several crystalline materials were chosen as laser hosts, such as garnet crystals (mixed aluminate garnets and gallium garnet matrices), double molybdates, oxoborates and fluorides, owing to their excellent spectroscopic properties.

1.2 Key achievements

The key outcomes of this thesis are summarized below. The units used here and throughout the thesis are consistent with those applied in the respective scientific articles.

1. An ytterbium doped mixed yttrium–lutetium aluminum garnet, with novel composition denoted as $(Y_{0.638}Lu_{0.212}Yb_{0.150})_3Al_5O_{12}$, was grown by the Czochralski method (Cz) where a detailed structural characterization, and a deep spectroscopic examination were performed. Efficient continuous-wave laser operation (CW) at λ_L~1µm, with tunable output wavelength, was successfully achieved under Ti: sapphire pumping. Furthermore, with microchip geometry, power scaling with a maximum output power of approximately 9 W at 1.05 µm was achieved, exhibiting a slope efficiency of 76%.

2. Demonstration of the first laser operation of ytterbium-doped potassium yttrium double molybdate crystal (Yb:$KY(MoO_4)_2$) grown by LTG Cz method. CW laser operation was achieved in microchip geometry using a thin crystal plate (thickness: 286 µm) under diode pumping.

3. Demonstration of growth, structure, polarized spectroscopy and efficient CW laser operation of an Yb^{3+}-doped disordered calcium gadolinium borate crystal, Yb^{3+}: $Ca_3Gd_2(BO_3)_4$ (Yb: GdCB). This laser crystal featured laser scaling capability (output power of 5.58 W at ~1057 nm with a slope efficiency of 51.7%) with broadband emission properties.

4. The first demonstration of optical spectroscopy and CW laser operation of an ytterbium-doped yttrium gallium garnet (Yb:YGG) crystal at cryogenic temperatures. The cryogenic CW laser was achieved by using a volume Bragg grating (VBG)-stabilised laser diode emitting at 969 nm as the laser pump source. At 120 K, a maximum output power of 17.50 W was reached at λ_L 1024 nm.

5. Demonstration of CW and passively *Q*-switched operation of a compositionally "mixed" heavily doped 16.6 at. % Yb:$(Y,Lu)_3Al_5O_{12}$ garnet crystal at cryogenic temperatures. At 140 K, in the CW regime, a maximum output power of 10.65 W was achieved at λ_L 1029 nm with a slope efficiency of 56%. Passive *Q*-switching of this crystal using Cr:YAG saturable absorber resulted in an energy/duration of 0.15 mJ/201 ns, at a repetition rate of 39.7 kHz.

6. Demonstration of the first CW laser operation of mechanically cleaved crystal-plates of Nd: $CsGd(MoO_4)_2$ in a microchip-type laser cavity. The laser delivered up to 0.54 W at λ_L 1066 nm with a high slope efficiency of 60.4% featuring low laser threshold of 70 mW and a linearly polarized laser emission.

7. Report on the crystal growth, spectroscopy and first laser operation of a novel double molybdate compound – Tm:$KY(MoO_4)_2$. CW laser was achieved in such thin films and plates of this crystal yielding a maximum output power of 0.88 W at ~1.9 µm with a slope efficiency of 65.8% and a linearly polarized laser output.

8. Development and characterization of a novel laser crystal with broadband emission properties at ~2 µm – a Tm^{3+}, Li^+-codoped calcium tantalum gallium garnet (Tm:CLTGG).

9. Demonstration of the growth, structure refinement, optical spectroscopy and a tunable CW laser operation of a Tm^{3+}, Ho^{3+}-codoped disordered calcium niobium gallium garnet (CNGG) crystal emitting in the eye-safe spectral range.

10. Demonstration of laser characteristics and performance in CW regime of a Tm:YLF crystal for ~ 2µm laser using an innovative microchip laser setup operating at cryogenic temperatures.

1.3 Thesis synopsis

Following a brief introduction and a summary of the key achievements in Chapter 1, Chapter 2 of this thesis provides an overview of the applications of lasers operating in the NIR range. It delves into the fundamentals of rare-earth -doped solid-state lasers that emit within this range. Chapter 3 details the experimental techniques used to fabricate and characterize the laser gain media. Chapter 4 highlights key results, including the growth of the crystals, physical and spectroscopic characterization, and laser performance of the studied materials. The thesis concludes with a summary of findings and suggestions for future work

CHAPTER 2

CHAPTER 2: Rare earth-doped materials for near infrared lasers: State-of-art and literature review

2.1. Applications of infrared lasers

The development of modern laser systems in near infrared (NIR) ranges has been driven by many factors, particularly scientific advances, and demand in applications. In terms of their applications, we are dealing with a wide range of uses in remote sensing, defense, and medicine. These specific areas will be discussed in detail further below.

2.1.1. Clinical applications of near-and mid-infrared lasers

The impact of a laser on tissue depends on both the tissue's characteristics and the laser's properties. Tissue properties include its structure, water content, thermal conductivity, heat capacity, density, and its ability to absorb, scatter, or reflect energy. Key laser properties that should be controlled in clinical applications are power density, pulse energy for pulsed lasers, and wavelength. Different biological targets absorb light differently, with their optimal absorption spectra varying based on the laser's wavelength. In human tissues, water, collagen, and hydroxyapatite absorb mid infrared light, while visible light and NIR lasers primarily target hemoglobin and melanin [28]. Figure 2.1 displays the infrared absorption spectra of water, collagen, and hydroxyapatite in human bone and dental tissues. For CO_2 lasers, water is the main chromophore [29]. Achieving selective photothermolysis involves targeting specific chromophores in the tissue with a laser wavelength that they absorb, ensuring minimal damage to surrounding tissues.

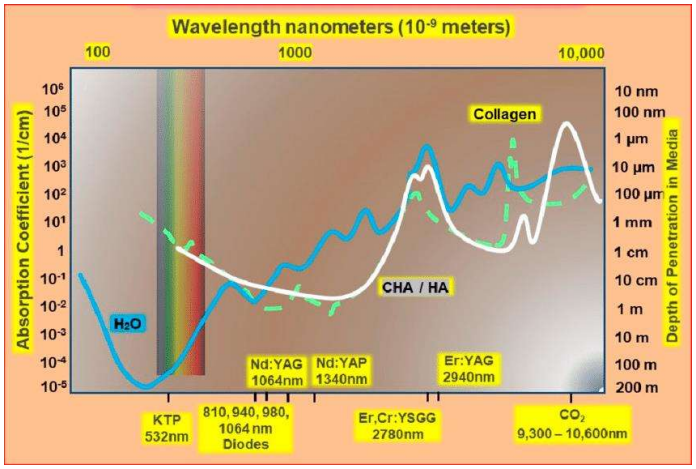

Figure 2.1. Absorption spectra for major tissue components relevant to the management of bone and dental hard tissues, with absorbance levels compared to irradiation wavelengths. The key tissue components highlighted are water, in blue, collagen in green, and both hydroxyapatite (HA) and carbonated HA (CHA), shown in white [30].

The shift towards minimally invasive procedures in healthcare has highlighted the importance of NIR lasers across various medical specialties. These lasers are essential in the operating room and are extensively used in ophthalmology, stone fragmentation, cancer treatment, and cosmetic procedures. In the realm of lithotripsy, for example, lasers have revolutionized the treatment of urinary and biliary stones through methods such as photoacoustic/photomechanical and photothermal effects. The pulsed Ho:YAG laser, which emits at 2.1 μm that is effectively

absorbed by water, is particularly prominent in this area and has been the subject of extensive research [31]. It has proven more effective in endoscopic removal of ureteral stones than pneumatic lithotripsy, according to research by Cimino [32], Figure 2.2(a). Teichman's review confirms the laser's safety and efficacy [33], making it a preferred method for both ureteral and biliary stones. Another notable example is the Q-switched Nd: YAG laser (Figure 2.2(b)), which operates similarly but creates larger shockwaves, enhancing its effectiveness [34].

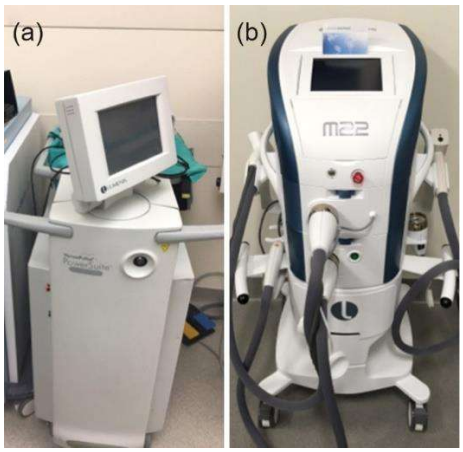

Figure 2.2. A commercial Ho:YAG lithotripsy laser [32] (a) and a Nd: YAG dermatologic laser [35](b).

2.1.2. LIDAR Systems Based on Infrared Solid-State Lasers

Lidar (Light Detection and Ranging) is a remote sensing technology that measures distance by illuminating a target with infrared laser light and analyzing the reflected light. It is widely used in various fields, including autonomous vehicles, environmental monitoring, and topographic mapping, see Figure 2.3. The focus of this introduction is on lidar systems that utilize infrared solid-state lasers, highlighting their principles, advantages, and applications [36–38].

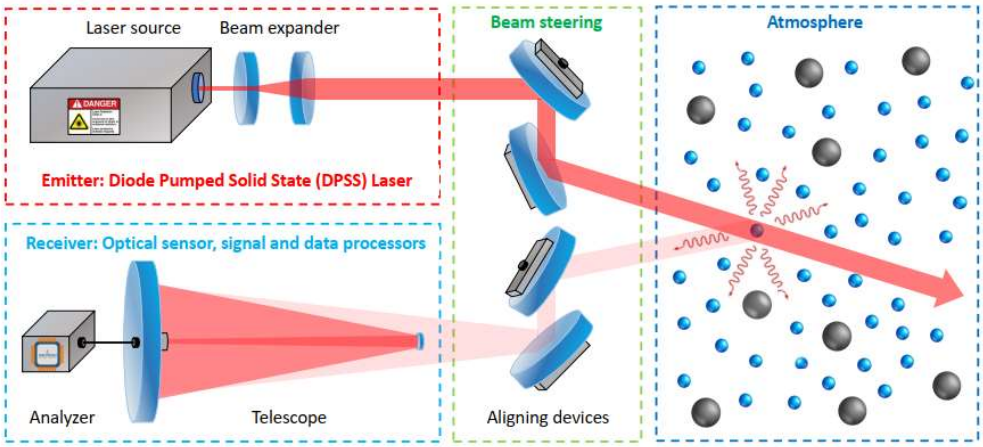

Figure 2.3. Atmospheric LIDAR working principle [39] .

Lidar systems operate by emitting laser pulses toward a target and measuring the time it takes for the reflected pulses to return to the sensor. This time-of-flight measurement is then converted into distance information. The basic components of a lidar system include:

- Infrared laser Source
- Scanner and Optics: Direct the laser pulses and collect the reflected signals.
- Photodetector: Converts the reflected light into electrical signals.
- Timing Electronics: Measure the time interval between emission and reception of the pulses.
- Data Processing Unit: Analyzes the data to generate distance and three-dimensional information.

The lasers at the core of Lidar systems should provide coherent light necessary for accurate distance measurements. The choice of laser source is critical for the performance of a Lidar system, influencing factors such as range, resolution, and the ability to penetrate different types of media (e.g., vegetation, fog, and atmospheric particles) [40–42]. Infrared solid-state lasers emitting in the range 1-2.1 μm are a popular choice for Lidar systems due to their specific advantages:

- Wavelength: Infrared wavelengths are less affected by atmospheric conditions such as fog, rain, and dust, providing more reliable data.
- Eye Safety: Lasers operating at 1550 nm or at ~2 μm are generally considered eye-safe at higher power levels, making them suitable for applications where human exposure is a concern.
- Compactness and efficiency: Solid state lasers are compact, efficient, and can be easily integrated into various platforms, from drones to autonomous vehicles.

Ho and Tm doped lasers have garnered significant interest for Lidar applications [37,43,44]. These lasers operate in the eye-safe wavelength region, making them suitable for applications where human safety is a concern. Additionally, the unique properties of Ho and Tm lasers, such as high efficiency, tunable wavelengths, and the ability to generate high peak powers, make them ideal candidates for advanced Lidar systems. High repetition frequency, high energy, and single longitudinal mode 2.1 μm lasers can be used for wind and atmospheric pollutant measurements. Recently, a high-power coherent Lidar based on Tm,Ho:YLF has been reported [44].

2.1.3. Pump source for OPO and OPA lasers systems

Optical conversion in optical parametric oscillators (OPO) and amplifiers (OPA) is an extensively utilized and versatile method for generating tunable-efficient laser sources [45–47]. This technique is particularly crucial in the mid infrared (mid-IR) part of the spectrum, which lacks a broad range of solid-state coherent laser sources, with quantum cascade lasers and chalcogenide-based lasers doped with transition metals being the primary options. Non-linear optical crystals like Zinc Germanium Phosphide (ZGP) are well-suited for mid-IR conversion when pumped near 2 μm [48,49], benefiting from a variety of high-power pump lasers, mainly Ho and Tm lasers, known for their superior beam quality [50–52]. ZGP crystals stand out for their excellent thermal and mechanical properties, making them ideal for high-power and high-energy demands. Recent improvements in crystal growth techniques have notably reduced residual pump absorption at 2 μm to 0.02 cm^{-1} and raised the laser-induced damage threshold for nanosecond pulses to 4–5 J/cm^2. These lasers are increasingly sought after in areas like remote sensing, free-space communication, and defense countermeasures. The effectiveness of

these advancements is exemplified by a newly developed OPO system that uses a 2 µm Ho:LLF laser, as illustrated in Figure 2.4.

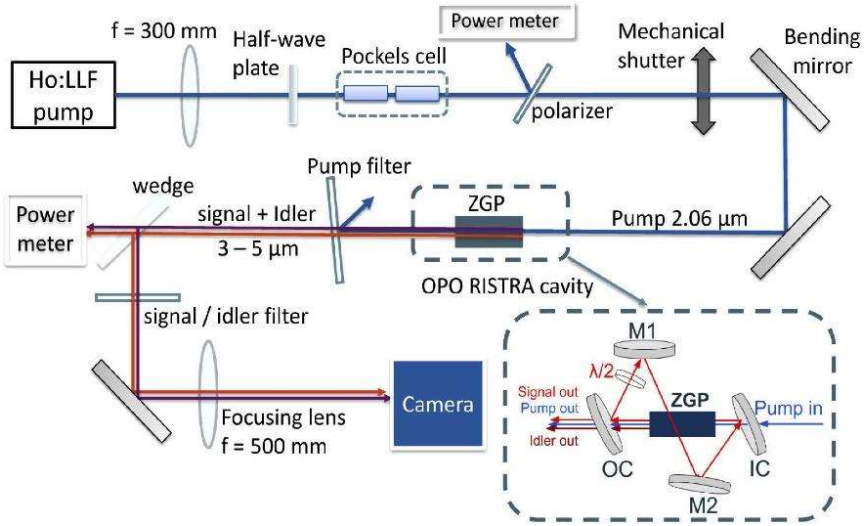

Figure 2.4. Experimental setup of recently developed OPO cavity based on ZGP nonlinear crystal pumped by 2 µm Ho:LLF laser [53]

Yb-doped lasers are widely used in high-power applications due to their excellent thermal management properties and high efficiency. Yb lasers typically operate in the 1.03–1.08 µm wavelength range, depending on the host medium. The broad emission spectrum of Yb lasers also enables tunability, making them ideal for pumping OPOs where fine control over the pump wavelength can optimize the OPO performance, an example of such approach is presented in Figure 2.5(a). Nd-doped lasers, particularly those pulsed operated in the Q-switched regime with nanosecond (ns) and picosecond (ps) pulse duration and with high repetition rate, are another popular choice for OPO pumping, see an example Nd pumped OPO laser in Figure 2.5(b). These lasers typically emit at 1.064 µm and can be efficiently pumped by diode lasers. The choice of Nd lasers as pump sources for OPOs is often driven by their well-established technology and compatibility with widely used nonlinear crystals, such as KTP (potassium titanyl phosphate) and LBO (lithium triborate), PPLN (periodically poled lithium niobate), which efficiently convert the pump wavelength to other wavelengths via parametric processes.

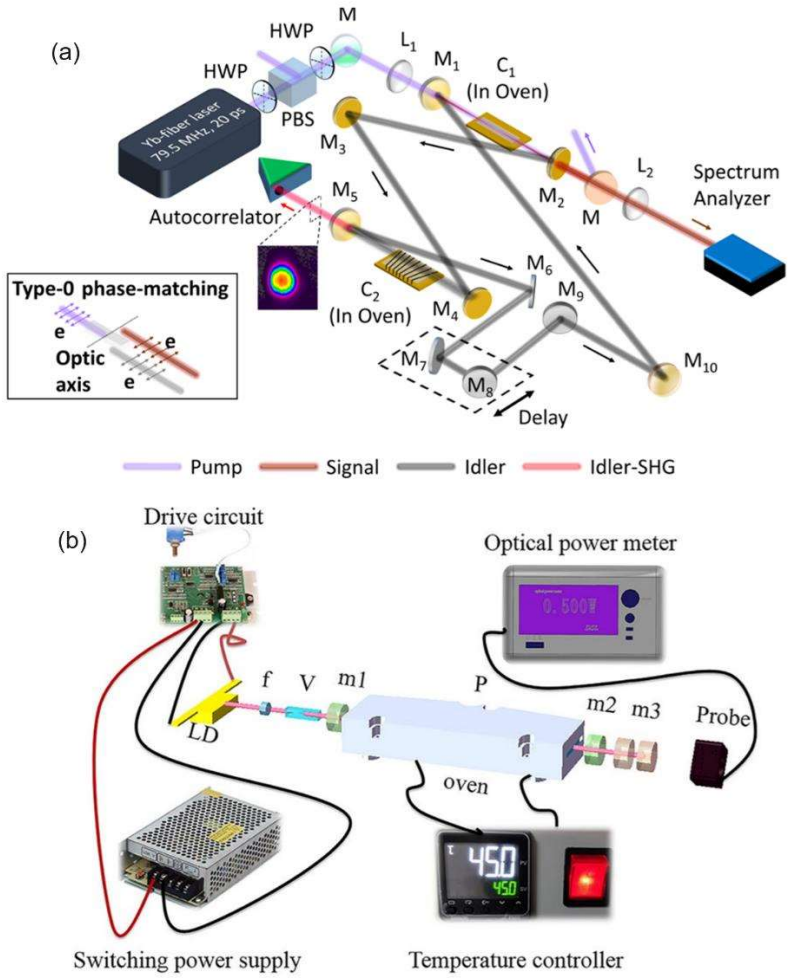

Figure 2.5. (a) Experimental setup for intracavity picosecond idler-resonant OPO pumped by an Yb-fiber laser; (b) Experimental schematic diagram an OPO pumped by Nd vanadate laser [54,55].

2.1.4. IR Lasers in materials processing engineering

NIR-and mid-IR lasers are used in material processing and can be classified into two main categories based on the required energy and the resulting effects. The first category involves applications that require low energy and induce minimal microstructural changes in small areas without altering the material's state. Examples include semiconductor annealing, polymer curing, and marking integrated circuit substrates. The second category requires substantial energy to cause state changes and phase transformations in larger areas, such as cutting, welding, surface hardening, alloying, and cladding. In these applications, the processes involve significant energy input due to the rapid phase changes. Different types of lasers can be used for both categories, either in continuous wave (CW) or pulsed mode, as long as the appropriate power/energy density and interaction time are applied for the specific wavelength [56–58].

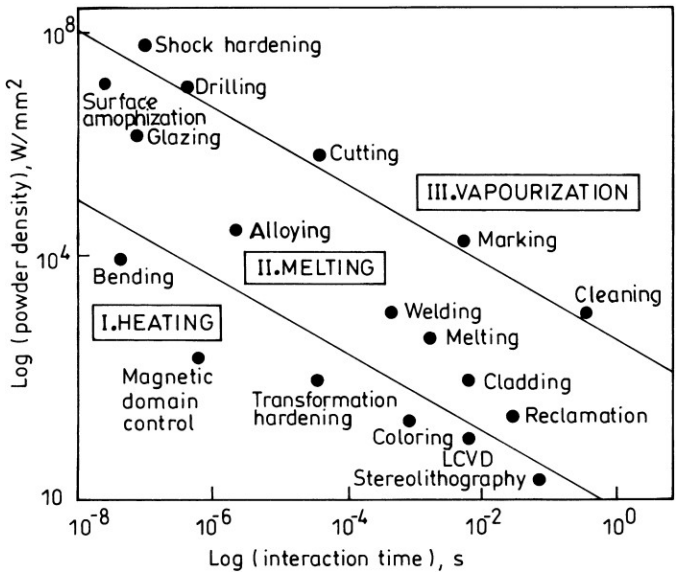

Figure 2.6. Process map (schematic) in terms of laser power density as a function of interaction time for different examples of laser material processing [59].

The different processes for laser treatment of materials can be categorised in terms of laser power and interaction time, as shown in Figure 2.6. These procedures are grouped into three main classes: heating (without melting or vaporising), melting (without vaporising) and vaporising. Processes such as transformation hardening, bending and magnetic domain control, which require surface heating without melting, require low power density lasers. On the other hand, operations such as surface melting, glazing, coating, welding and cutting, which involve melting, require high power density lasers. In addition, processes such as cutting and drilling, which vaporise the material, require very high-power density, which is delivered in very short interaction or pulse times.

While it might seem convenient to use a single scalar parameter like energy density (power density multiplied by time) for simplification, this approach is impractical. The critical factor is not just the total energy delivered but how it interacts with the material in both time and space. For example, an energy density of 10^2 J/mm² could result in either surface hardening or surface melting, depending on the specific combination of power density and interaction time [59]. Thus, the level of energy and the manner in which it is applied are key to obtaining the necessary changes in the material. For example, a commercial Q-switched laser system, TruMark 5020, based on a Nd:YAG crystal laser with a wavelength of 1064 nm was used for laser ablation processing of surfaces, and four pulse rates (L1: 400 kHz, L2: 200 kHz, L3: 100 kHz, L4: 10 kHz) could be chosen in this system, from low to high laser fluences [60]. In the same report, we found that laser glasses doped with Nd, Er and Yb were used for surface processing to bond metallic materials.

2.2. Solid-state lasers: fundamental and rare earths-based NIR lasers

2.2.1. Interaction of light with matter

2.2.1.1. Absorption and emission of light

Figure 2.7 illustrates the spectroscopic processes occurring in ions, atoms or molecules, such as ground-state absorption (GSA), spontaneous emission, stimulated emission (SE), and multiphonon relaxation.

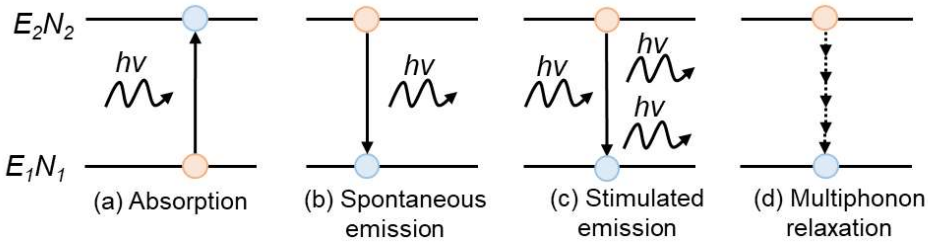

Figure 2.7. Spectroscopic processes occurring in a two-level system (ionic, atomic or molecular).

When a photon with energy $E_{phot} = hv$ encounters an ion, atom or molecule with two distinct energy levels, as illustrated in Figure 2.7(a), absorption occurs if the condition $E_{phot} = E_2 - E_1$ is fulfilled. This causes the specimen to become excited, a phenomenon referred to as GSA. The alteration in the electronic population of the lower energy state, N_1, can be represented as follows:

$$\left(\frac{dN_1}{dt}\right)_{abs} = -W_{12}N_1 = -\sigma_{12}FN_1, \text{ Eq.2.1}$$

The transition probability between 1 and 2 levels is given by W_{12}, whereas F is the photon flux, and σ_{abs} is the GSA cross-section.

If an ion is already in an excited state, it can emit a photon exhibiting properties identical to those of the absorbed photon (same frequency, propagation direction, and polarization). This process is called stimulated emission (SE), Figure 2.7(c). The population N_2 of the excited state changes as:

$$\left(\frac{dN_2}{dt}\right)_{SE} = -W_{21}N_2 = -\sigma_{21}FN_2, \text{ Eq.2.2}$$

where W_{21} is the transition probability from 2 to 1 level, and σ_{SE} is the SE cross-section.

Radiative transitions also encompass the process of excited-state absorption (ESA). In a three-level system, this requires the condition $E_3 - E_2 = E_2 - E_1$ to be met. This indicates that a photon with a specific energy can be absorbed by a specimen that is already in an excited state.

2.2.1.2. Energy transfer process

The upper laser level can be populated not only by absorbing pump photons but also through various energy transfer mechanisms. These additional processes, which may enhance or reduce efficiency through redistribution of the electronic population, involve nonradiative interactions between closely situated laser ions. Typically, these interactions require high doping levels in the laser gain medium making the separation among ions to be short enough to favors the transfer of energy. The following description will explore scenarios where an excited donor ion transfers energy to an acceptor ion that is either in a ground state or partially excited:

- **Energy migration**

Energy migration involves transferring the entire excitation energy from a donor to an acceptor specimen (ion, atom or molecule). The acceptor can either be of the same nature as the donor, as shown Figure 2.8(a), or a different laser specimen with resonant energy levels, often occurring for instance in codoped systems with a sensitizer ion when talking of solid-state laser

systems. The energy may move sequentially between ions, allowing it to travel through the laser material, with each donor ion experiencing nonradiative de-excitation. This process can decrease laser efficiency if the energy reaches areas of the material with defects, leading to nonradiative decay.

- **Upconversion**

Upconversion in optical materials typically occurs via one of the following mechanisms:

- ESA upconversion: an ion in the material absorbs a photon and moves to an intermediate energy level. A second photon is then absorbed, promoting the ion to a higher energy state, from which it can emit a photon of higher energy.
- Or energy transfer upconversion (ETU): when energy transfer occurs between two ions. One ion in an excited state transfers its energy to another ion, elevating the second ion to a higher energy state, which can then emit a higher-energy photon.

This process is depicted in of Figure 2.8(b). In contrast, excited state absorption upconversion involves the sequential absorption of pump photons by a specimen, pushing it beyond the usual pump level. While upconversion is often seen as a parasitic loss, it can also be harnessed beneficially in upconversion lasers. Depending on the energy level arrangement, this elevated excitation can be achieved using a single pump laser or multiple wavelengths to target specific transitions.

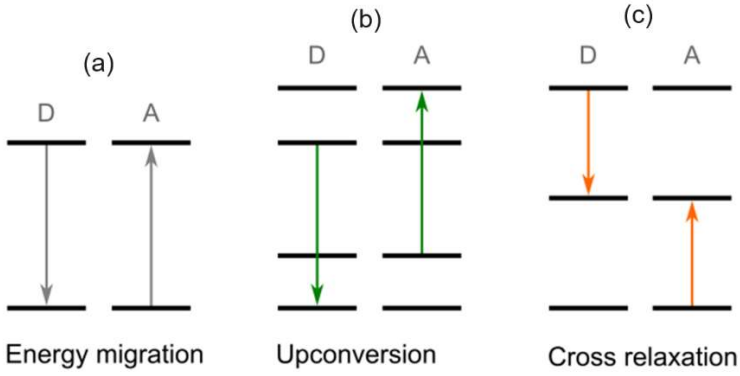

Figure 2.8. Examples of the nonradiative energy transfer processes: (a) energy migration; (b) upconversion; (c) cross relaxation, with labelled donor D and acceptor A.

- **Cross relaxation**

In cross relaxation, energy is transferred such that both the donor and acceptor find themselves in intermediate energy levels above the ground state. A schematic representation where both specimens achieve the same energy level is depicted in Figure 2.9(c). This process, like energy transfer upconversion, occurs between adjacent ions. However, it differs because the acceptor's final energy level is lower than the donor's starting level, and the acceptor does not need to be initially excited. The relevance of this mechanism, especially in Tm^{3+}-doped lasers, will be explained in the subsequent section.

2.2.1.3. Four and quasi-three level lasers systems

Four-level lasers operate through an energy level system depicted in Figure 2.9(a). This setup typically includes a single pump level, E3, where rapid transitions occur to the upper laser level, E2, and to the ground state, E0. These quick transitions keep the populations at E3 and E1

minimal, facilitating the easy achievement of population inversion at the upper laser level. When this inverted medium is positioned between two resonator mirrors, stimulated emission begins, triggered by photons that are spontaneously emitted and then reflect between the mirrors. This interaction leads to a swift increase in the laser field within the resonator due to a cascade effect of photon production. With one mirror being partially transparent, the laser field can be released, creating the familiar laser beam [61,62].

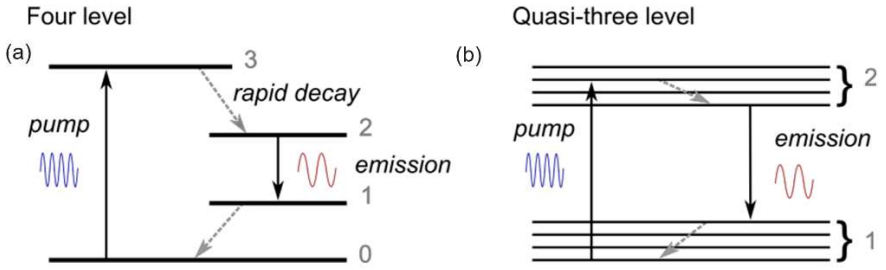

Figure 2.9. Schematic diagrams of the four (a) and quasi-three level (b) systems.

A quasi-three-level laser system involves a distribution of energy levels slightly different from that of a four-level system. In this arrangement, the upper and lower laser levels consist of two Stark levels. The pump level can either be part of the same Stark manifold as the upper lasing level or at a higher energy level, as illustrated in Figure 2.9(b). When the pump and upper lasing levels are in the same manifold, this process is called in-band pumping. However, unlike four-level systems, the ground level and lower laser level in a quasi-three-level system are not fully decoupled. This resulted in a temperature-dependent population at the lower laser level, including a significant thermal population. As a result, the reabsorption of the laser emission must be considered during the analysis. Additionally, in the case of highly inverted media, re-emission at the pump wavelength should also be considered.

2.2.2. Rare-earth ions -doped solid-state materials for efficient NIR lasers

2.2.2.1. Ytterbium and neodymium: dopant ions applied near 1µm lasers

For high average power operation Yb^{3+}-doped crystals are most interesting because the Yb^{3+} ion exhibits very small Stokes limit, i.e. small quantum defect (different between the pump energy photons and laser energy photons) and hence very small heat generation in the laser crystal, see Figure 2.10.

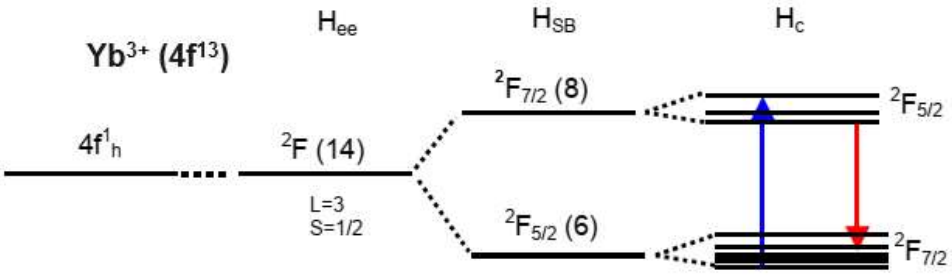

Figure.2.10. Levels scheme of Yb^{3+}: Free ion state, electron-electron interactions (H_{ee}), division caused by spin-orbit interaction (H_{SB}), and modifications by the crystal field (H_c). Arrows on the

diagram denote pump and laser transitions. Parentheses around numbers show the degeneracy of each level [63].

The discovery of the laser oscillation in Yb^{3+} doped gain materials was a notable advancement in laser technology, with the development of a diode-pumped, Yb:YAG laser at room temperature in 1991 [64] reigniting interest in Yb-doped materials for diode pumping at RT. Yb^{3+}-doped solid-state lasers present several advantages compared to other rare-earth lasers. They possess only two energy states: the ground state $^2F_{7/2}$ and the excited state $^2F_{5/2}$, separated in energy by roughly 10,000 cm^{-1}. This simplicity avoids excited-state absorption of both pump and laser light. The absorption band near 970 nm is well-suited for diode pumping due to the well-stablished technology of diode lasers operating at this wavelength, and the emission cross-sections are adequate for showing net gain. Notably, the quantum efficiency of the upper laser state, $^2F_{5/2}$, is nearly perfect, and the minimal Stokes shift and small quantum defect lead to reduced heat generation, making Yb^{3+} ideal for high-power laser applications. The broad emission band of Yb^{3+} allows for laser tunability and the production of ultrashort pulses. Additionally, the upper laser level's radiative lifetime spans from several hundred microseconds to a few milliseconds across different crystals, enhancing energy storage efficiency which is advantageous for Q-switched laser operation.

Hundreds of lasers have been realized with Nd^{3+} ions, mainly in oxide crystal hosts. The Nd ion is capable of producing several NIR laser transitions, particularly around 900 nm, 1060 nm, and 1300 nm. The primary and most utilized transition is from the $^4F_{3/2}$ to $^4I_{11/2}$ energy levels, emitting in the 1050 nm to 1100 nm range, as illustrated in Figure 2.11, depending on the specific host lattice. Nd lasers are commonly pumped with diode lasers around ~800 nm, which is beneficial for designing compact and high power laser systems due to the existence of matured technology of laser diodes operating in this spectral range. [65–67].

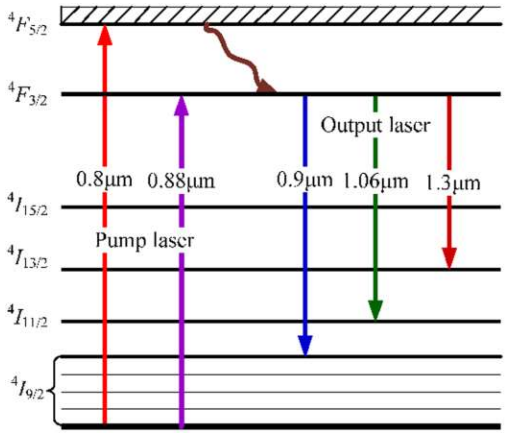

Figure 2.11. Energy-level diagram of Nd^{3+} ions. Arrows pointing up denote absorption processes while arrows pointing down denote emission processes [68].

2.2.2.2. Thulium and holmium: laser ions emitting in the ~2–2.1 µm spectral region

To develop a laser source that emits in the ~2–2.1 µm wavelength range, exploring the spectroscopic properties of Tm^{3+}-doped gain media is necessary. This section provides an overview of the Tm^{3+} laser ion, including a concise history of its use in laser sources. Additionally, a brief overview of Ho^{3+} laser ions and Tm, Ho -codoped systems will be

discussed to broaden the understanding of various lanthanide dopants capable of emitting in the mid-IR region.

Thulium ion (Tm^{3+})

The development of Tm^{3+}-doped gain media, a cornerstone in laser technology, has its roots stretching back to the early 1960s. Specifically, in the years 1962 and 1963, foundational experiments led by Johnson and his colleagues pioneered the use of Tm^{3+}:$CaWO_4$ and Tm^{3+}:SrF_2 as laser materials, which were notably operated at the cryogenic temperature of 77 K, cooled by liquid nitrogen, as documented in their seminal work [69]. It was not until the 1970s, however, that such lasers were successfully operated at room temperature, marking a significant technological advancement [70]. These laser systems primarily utilized flashlamps for pumping and incorporated Cr^{3+} ions as sensitizers to facilitate the energy absorption and transfer processes necessary for laser action. A notable shift occurred in the 1980s with the advent of the Ti:sapphire laser, which introduced the capability for direct excitation of Tm^{3+} ions around 800 nm [71]. This development significantly streamlined the excitation process by eliminating the need for intermediate sensitizers. In more recent developments, the use of high-power AlGaAs laser diodes, which were originally developed for Nd^{3+}-doped lasers, has proved to be highly effective in pumping Tm^{3+}-doped gain media. This adaptation has led to substantial improvements in efficiency, leveraging the advanced capabilities of these diodes.

Further refining the efficiency of Tm^{3+}-doped lasers, the process of cross-relaxation plays a crucial role, particularly in the efficient population of the $^3F_4$ upper laser level when using 800 nm laser radiation, as detailed in Figure 2.12. This mechanism involves the transfer of energy within the $^3H_4$ manifold to a nearby Tm^{3+} ion, which simultaneously elevates from the ground state to the same energy level. Such interactions, often described as "two-for-one" pumping, have the potential to theoretically enhance the power efficiency up to 80%, significantly exceeding the quantum defect limit that typically constrains efficiency due to the energy disparity between the pump and emitted laser photons.

An additional aspect of Tm^{3+}-doped lasers is their capacity to produce blue upconversion light. This phenomenon occurs when the lasers are pumped around 800 nm, leading to emissions from the 1G4 manifold that result in the production of blue light near 480 nm. The process is initiated through excited state absorption at the $^3H_5$ level, which subsequently populates the $^1G_4$ level. However, the influence of upconversion on overall laser performance is moderated by the relatively brief lifetime of the $^3H_5$ manifold, which undergoes rapid nonradiative decay to the $^3F_4$ level, thus reducing the duration and impact of this upconversion pathway. The transition to the $^3H_5$ level itself is contingent upon prior energy relaxation within the $^3H_4$ level through cross-relaxation decay [72]. This intricate interplay of energy levels and transitions underpins the sophisticated operational dynamics of Tm^{3+}-doped lasers, showcasing their complex yet highly efficient nature.

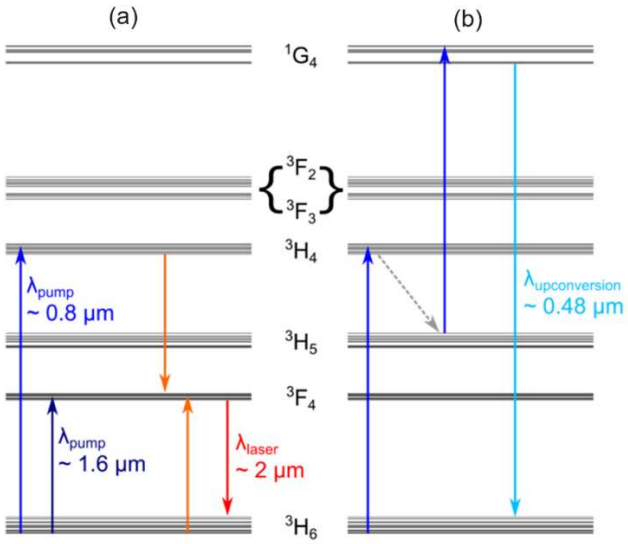

Figure.2.12. (a) Energy level diagram for Tm^{3+} ions illustrating the pumping processes at 0.8 µm and 1.6 µm for in-band pumping. The cross-relaxation mechanism for the "two-for-one" pump strategy is highlighted in orange; (b) Diagram for excited state absorption up-conversion depicting the filling of the $^1G_4$ manifold by 0.8 µm pump photons. A dashed grey line shows nonradiative relaxations [72].

The process of directly populating the upper laser level can be achieved through in-band pumping at wavelengths 1.6 µm. This technique notably diminishes the quantum defect and simultaneously circumvents issues associated with cross-relaxation, ultimately offering a theoretical efficiency that is on par with that observed in 800 nm pumping scenarios. The underlying mechanism that accounts for the blue upconversion emission observed during this in-band pumping process is considerably complex, involving a sequence of energy transitions across multiple metastable states that lead up to the $^1G_4$ level.

This phenomenon can be elucidated by examining the dynamics of excited state upconversion within the upper laser level. Initially, ion excitation occurs, moving to the $^3H_4$ level. Subsequently, this is followed by a nonradiative decay to the $^3H_5$ level. The process continues as further upconversion transpires through the $^3F_2$, and $^3F_2$ manifolds. This pathway mirrors the sequence of events typically seen with 800 nm pumping, where similar transitions and manifolds are involved, albeit initiated by a different pumping wavelength. Through these successive transitions, the system effectively facilitates the generation of higher energy photons, manifesting as blue upconversion emissions.

Holmium (Ho^{3+})

The exploration and development of holmium (Ho^{3+})-doped laser gain media commenced during the 1960s, a period noted in the literature [73]. Although these Ho^{3+}-doped lasers were conceptualized around the same time as Tm^{3+}-doped lasers, it wasn't until the subsequent decade of the 1970s that Ho^{3+}-doped lasers demonstrated the capacity to operate at room temperature. However, these lasers were limited to pulsed operation modes during this initial phase of development [74]. In contrast to Tm^{3+}, Ho^{3+} do not possess significant absorption bands in the NIR spectrum. Consequently, in-band pumping strategies have been adopted,

specifically around the wavelength of 1.9 µm, which effectively facilitates the $^5I_7$ to $^5I_8$ laser transition near 2.1 µm as illustrated in Figure 2.13.

This method of pumping at 1.9 µm not only supports the necessary energy transitions but also offers a high theoretical quantum efficiency. However, one of the substantial challenges in this domain involves locating efficient sources for this specific pumping wavelength. Although thulium-doped solid-state and fiber lasers have been traditionally employed to pump Ho3+-doped gain media, advancements in directly diode-pumped Ho^{3+}-doped lasers have been somewhat stagnant in recent years. This is in spite of the gradual increase in the availability of 1.9 µm laser diodes, which have seen limited new demonstrations reported in the literature over the last decade.

Moreover, the physical properties of holmium ions differ notably from those of other common dopants like thulium and ytterbium (Yb^{3+}), due to the less pronounced effect of lanthanide contraction in Ho^{3+}. This results in the 4f orbital of Ho^{3+} ions being more effectively shielded compared to those of Tm^{3+} and Yb^{3+}. A direct consequence of this shielding is the narrower linewidths of laser transitions observed in Ho^{3+}-doped media. This characteristic typically leads to longer pulse durations in Ho^{3+}-doped lasers when compared to those doped with thulium, further highlighting the unique operational dynamics and challenges associated with holmium as a laser dopant.

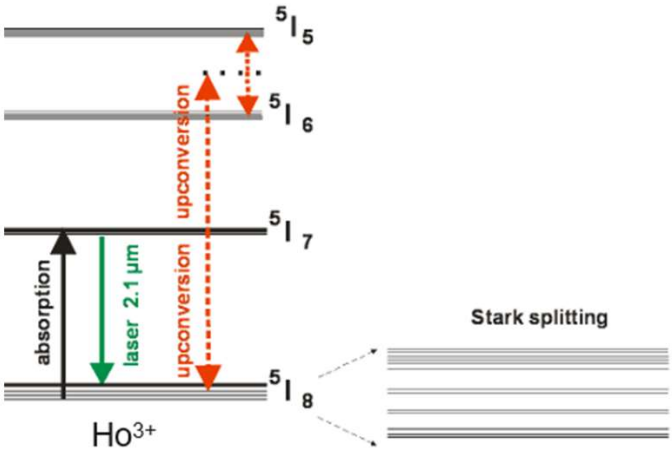

Figure.2.13. Energy level schemes and related 2.1 µm laser transitions of Ho^{3+} ions [75].

Tm, Ho-codoping systems

An alternative approach to produce long emission wavelengths from Ho^{3+} lasers with the convenient and practical use of 800 nm laser pumping is the use of Tm, Ho-codoped gain media. In these systems, laser excitation is achieved through established methods and pumping processes. The Tm^{3+} ions absorb the 800 nm pump radiation, leading to an efficienty population of the $^3F_4$ level via cross-relaxation. This energy can then rapidly migrate not only among Tm^{3+} ions but also to nearby ground-state Ho^{3+} ions by resonance, thereby populating the $^5I_7$ upper laser level of Ho^{3+} ions [76–78], as shown in Figure 2.14.

The development of Tm, Ho-codoped gain media has led to the production of lasers in the 2–2.1 µm spectral region, including CW, Q-switched and mode-locked lasers, with reported high efficiencies (XX%, search for a reference) and pulse durations ranging from 67 fs (79 fs before

extra-cavity compression) to 7.8 ps, using different host crystals and saturable absorbers [79–84]. Despite these successes, these lasers suffer from increased upconversion losses compared to single-doped Tm^{3+}lasers. In Tm, Ho-codoped materials, upconversion arises from two main processes: excited state upconversion, where an ~800 nm pump photon excites Ho^{3+} ions from the $^5I_7$ to the $^5S_2/^5F_4$ levels, producing visible fluorescence; and interionic energy-transfer upconversion, where Tm^{3+} ions transition takes place from the $^3F_4$ level to the ground state while simultaneously excitation of Ho^{3+} ions ocurres from the $^5I_7$ to the $^5I_5$ level, which can then emit fluorescence around ~900 nm [85].

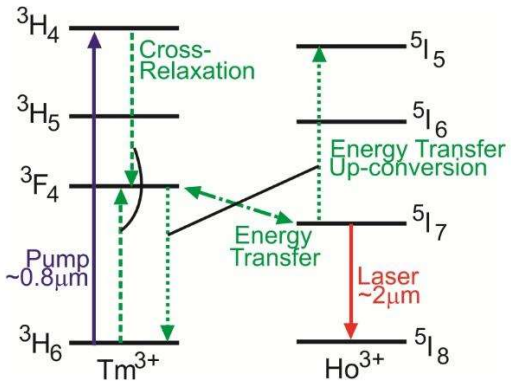

Figure.2.14. Energy levels diagram of the Tm, Ho codoped system with the energy levels involved in the absorption, cross-relaxation, energy transfer, up-conversion and laser generation around 2 μm processes [86].

2.2.2.3. Geometry of the gain medium in IR lasers

Choosing the right geometry for the gain medium is crucial for optimizing thermal management in solid-state lasers, considering the specific pump and laser wavelengths used. Effective heat removal requires a high ratio between the cooled surface and the pumped volume, along with minimal distance between them. Since Maiman's initial rod geometry demonstration of a solid-state laser [87], various geometries have been developed, but none is universally applicable. These geometries can generally be classified into the main types shown in Figure 2.15.

The rod geometry allows for the achievement of several kilowatts of CW output power [88]. However, it often suffers from limited beam quality due to radial heat gradients caused by lateral heat flow, as depicted in Figure 2.15(a). These gradients induce significant thermal lensing and may lead to rod cracking due to stress between the cooler surface and the hot pump channel.

Conversely, the slab geometry, considered in the context of this thesis and shown in Figure 2.15(b), provides efficient heat dissipation through the top and bottom surfaces of the gain medium. Modern diode-pumped slab lasers typically use edge pumping, leading to a more uniform heat distribution along the laser axis. Despite this, there remains a significant temperature gradient in the vertical direction. The zigzag slab laser concept was developed to counteract beam profile distortion, guiding the laser beam along a zigzag path via total internal reflection. This method averages out beam distortions, resulting in better beam quality. An output power of 15.3 kW with an M^2-value of 1.58 has been achieved using this approach in a single Nd:YAG slab [89].

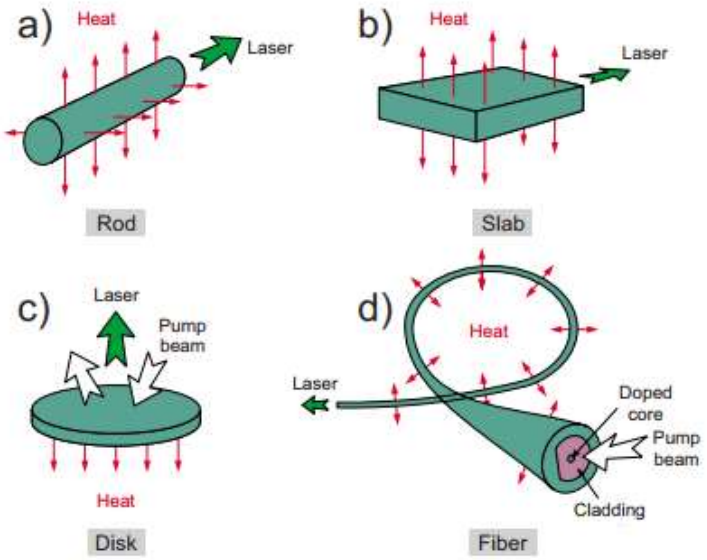

Figure 2.15. Schematic of the main geometries for solid-state laser materials [90].

The thin-disk laser design (Figure 2.15(c)) features a disk-shaped active medium, highly reflective on the back and water-cooled for effective heat dissipation [91]. The laser axis is perpendicular to the disk, which reduces heat gradient effects on beam quality. The disk is placed in a pump module that allows the pump light to pass 16–32 times, increasing absorption efficiency. This configuration is advantageous for quasi-three-level laser materials such as Yb: YAG, as it boosts pump intensity and lowers the typically higher laser threshold compared to four-level systems.

In standard high-power fiber lasers, the active medium consists of a thin, doped fiber core surrounded by two claddings, each with progressively lower refractive indices [92]. The pump light is introduced into the inner cladding either from the fiber ends or through tapered fibers attached to the cladding sides. The difference in refractive indices allows the inner cladding to act as a waveguide, directing the pump light. The pump light is absorbed only when it reaches the inner core, ensuring a uniform distribution of light along the fiber, as shown in Figure 2.15(d).

2.2.2.4. Spectral behavior of rare–earth ions in solids

The spectral lines of an emitting system may broaden due to various factors, appearing as either homogeneous or inhomogeneous broadening. Homogeneous broadening results in uniform broadening across individual atoms and the entire system, with each atom emitting the same central frequency, ν_0. In contrast, inhomogeneous broadening arises when resonant frequencies vary among individual atoms, causing the system's overall spectral line to broaden, even if each atom's line remains constant. Homogeneous broadening is characterized by a Lorentzian distribution, while inhomogeneous broadening is characterized by a Gaussian distribution. Figure 2.16 visually represents these two broadening types.

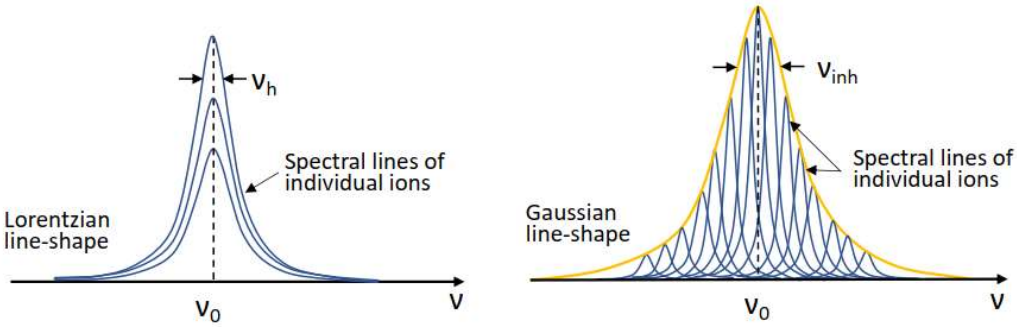

Figure.2.16. Spectral broadening behavior: (a) homogeneous and (b) inhomogeneous [93].

Consider this detailed explanation: An activator ion, when incorporated into a compound with an ordered structure and replacing matrix ions in equivalent positions, forms an ideal simple single crystal. Here, all interaction centers are identical, and the spectral line for each center appears identical in position and shape, leading to homogeneously broadened lines. However, real crystals often have slight defects, causing activator centers to differ slightly, especially at low temperatures, resulting in a superposition of slightly shifted lines, known as inhomogeneous broadening. The mechanisms of this broadening include structural disorder, heterovalent activation, and solid-solution crystals.

Structural disorder can occur when activator ions occupy non-equivalent positions, leading to multisite behavior, such as in cubic sesquioxides like Y_2O_3, rare-earth cations occupy two non-equivalent sites with C_2 and C_{3i} symmetry, leading to different crystal field strengths and even different selection rules for electric and magnetic dipole transitions [94]. It can also result from random distribution of host cations at one or more sites, causing variations in the surrounding composition and inhomogeneous broadening like the behavior observed in glasses, as seen in $CaGdAlO_4$, in which Ca^{2+} and Gd^{3+} cations are randomly distributed on identical lattice sites with C_{4v} symmetry [95].

Heterovalent activation involves ions with different charges but similar sizes replacing each other, necessitating charge compensation to maintain neutrality. This can lead to crystals with either single or multiple centers, as observed in rare-earth -doped cubic CaF_2 and its fluoride-type analogs [96].

Solid-solution crystals, also called compositionally mixed crystals, involve host materials forming substitutional isostructural series from parent compounds A and B, resulting in a compositionally disordered structure $A_{1-x}B_x$. These systems do not display well-defined line resolution but instead exhibit broad spectral bands due to overlapping lines, such as in cubic Y_2O_3 - Lu_2O_3 - Sc_2O_3 solid-solutions. This PhD thesis explores materials that exhibit all these types of inhomogeneous line broadening mechanisms.

2.2.3. Cryogenic lasers

Solid-state lasers operated at cryogenic temperatures offer attractive properties for high-power and efficient operation. This enables laser architectures with high average power scaling. Although initially considered impractical, cooling enhances key laser material properties such as thermal conductivity (k), thermal expansion factor (α) and temperature-dependent refractive index change, thermo-optic coefficient (dn/dT). Moreover, rare-earth -based lasers that are quasi-three-level systems at room temperature often become four-level at cryogenic

temperatures, improving efficiency [97,98] minimizing reabsorption phenomena. The use of cryogenics has become more practical as the technology has become commercialized.
There are four key reasons for operating solid-state lasers at temperatures significantly below room temperature. First, many rare-earth ions have laser transition levels near the ground state, making them quasi-three-level lasers at room temperature. However, at cryogenic temperatures, these lower laser levels become thermally depopulated, reducing the laser threshold, as shown in Figure 2.17.

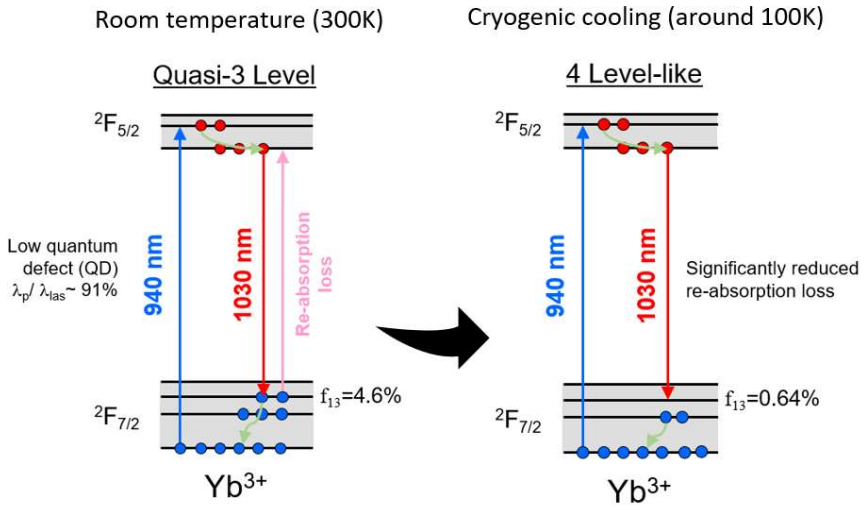

Figure.2.17. Yb^{3+}-electronic population distribution at cryogenic temperatures.

Secondly, for certain lasers, particularly those based on transition-metal ions like Co:MgF_2 [99] and Fe:ZnSe [100], the lifetimes of metastable levels significantly increase at lower temperatures due to reduced nonradiative relaxation rates, which in turn lowers the laser threshold. Third, the approach of cooling the active medium to cryogenic temperatures partially overcomes the aforementioned issues with reabsorption and low transition cross-sections. The transition cross-sections increase at low temperatures [101]. Lastly, cryogenic cooling reduces thermo-optic effects at a given power level, as the thermo-optic properties of the gain medium improve at lower temperatures. Crystalline dielectrics generally exhibit much higher thermal conductivity and lower α at liquid nitrogen temperatures compared to room temperature, resulting in a reduced thermo-optic coefficient (dn/dT). As shown in Figure 2.18, these attributes—thermal conductivity, α, and dn/dT—improve as the temperature decreases, specifically for undoped YAG. This improvement enhances the power scalability of solid-state lasers when operating at cryogenic temperatures compared to room temperature.

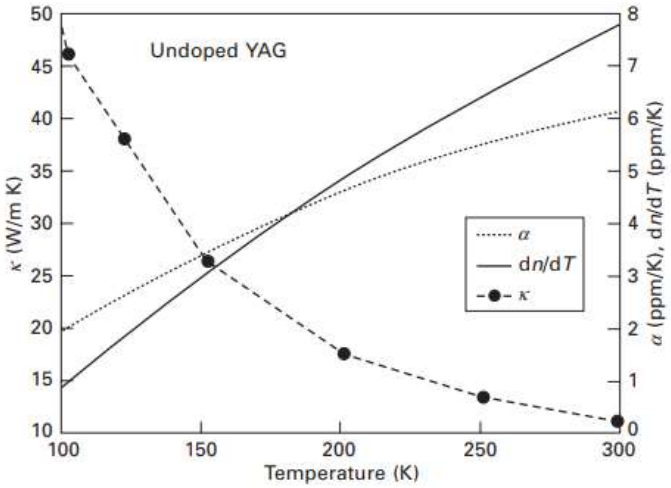

Figure.2.18. Plots of thermal conductivity *k*, coefficient of thermal expansion *α*, and *dn/dT* as a function of temperature for undoped YAG [98].

2.3. Hosts materials for rare-earth doped solid-state lasers

To realize an efficient solid-state laser, several key material characteristics are necessary. The laser-active medium must be manufactured in large scales with high optical quality, avoiding parasitic absorptions and scattering centers. High mechanical and chemical stability are crucial for crafting polished laser rods, slabs, and waveguides. For high-power applications, materials with high thermal conductivity and high damage threshold are essential. Moreover, a small d*n*/d*T* and low nonlinear refractive index (n^2) are advantageous for achieving a Gaussian beam profile and preventing self-focusing. It is difficult to find materials that meet all these criteria simultaneously. For example, sapphire and diamond offer the highest thermal conductivity among dielectrics but cannot be doped with rare-earth ions due to their large ionic size relative to the available lattice sites. Additionally, the crystal structure and local site symmetry for the active ion greatly influence the optical properties of the laser medium. In the sections that follow, different crystals families of laser host materials investigated in this PhD thesis will be described, highlighting their structural, thermal, and physical properties.

2.3.1. Garnet crystals

Garnet crystals are a class of materials that have become indispensable in the field of solid-state laser technology. Their unique combination of optical, thermal, and mechanical properties makes them excellent host materials for various rare-earth ions used as active laser elements.
Garnets crystals crystallize in the cubic system (space group $Ia\bar{3}d$). The general formula for garnet minerals can be represented as $A_3B_2(XO_4)_3$, where A and B denote different cations, and X can represent various anions depending on the specific type of garnet. Garnets exhibit a large variety of chemical compositions due to the substitutional flexibility within their crystal lattice [102–104]. This characteristic leads to a wide range of natural and synthetic garnet species, see in Figure 2.19 examples of well-known garnets used in the field of solid-state lasers. Garnets are easy to be grown by the conventional Czochralski growth method or by other methods such as the optical floating zone method [105,106].

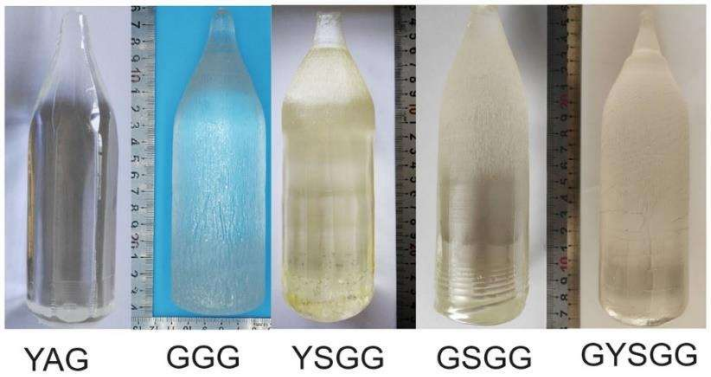

Figure 2.19. Photographs of some grown undoped garnet crystals by Czochralski method: YAG– $Y_3Al_5O_{12}$;GGG–$Gd_3Ga_5O_{12}$; YSGG–$Y_3Sc_2Ga_3O_{12}$; GSGG–$Gd_3Sc_2Ga_3O_{12}$; GYSGG–$GdY_2Sc_2Ga_3O_{12}$.

The crystal structure of the garnet crystals is shown in Figure 2.21. In the garnet lattice, ''A'' sites are occupied by large cations (such as Ca^{2+}, Mg^{2+}, Fe^{2+}, Y^{3+}, Gd^{3+}, Na^{+}, Li^{+}, etc.) and surrounded by eight anions, forming a dodecahedral polyhedron. The dodecahedron, specifically in the context of garnets, is often referred to as a distorted cubic polyhedron or a cuboctahedron due to its 12 identical faces, each being a regular pentagon. ''B'' sites accommodate small cations (like Al^{3+}, Fe^{3+}, Cr^{3+}, Ga^{3+}, etc.) where an octahedral environment resides, each surrounded by six oxygen atoms, forming a regular octahedron [104]. This sixfold coordination creates a robust framework that contributes to the crystal's structural strength. The X anion forms the center of a tetrahedron, surrounded by four oxygen atoms. These tetrahedral units are interconnected by sharing corners with the adjacent tetrahedra, forming a continuous framework, Figure 2.20. The XO_4 tetrahedra are rigid units that maintain the overall structure's integrity. In silicate garnets, these are SiO_4 tetrahedra, whereas, in aluminates or gallium garnets, they are AlO_4 or GaO_4 tetrahedra, respectively [107].

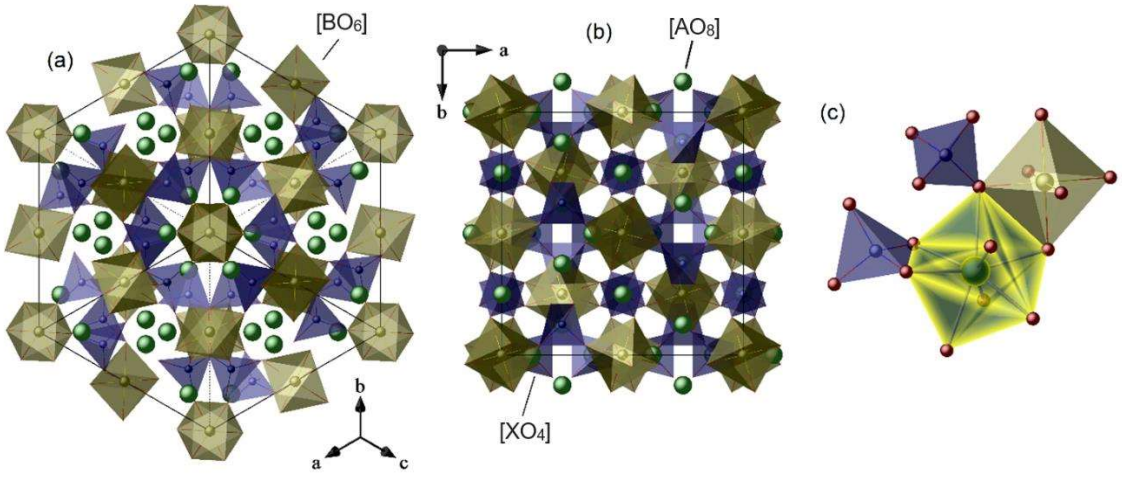

Figure 2.20. Crystal structure of garnets: (a) [111] direction view; (b) projection on the ***a-b*** crystallographic plane; (c) connection among polyhedra [AO_8], [BO_6] and [XO_4] [108] .

The coefficient of thermal expansion (α) is a significant parameter for crystal materials, impacting their growth and high-temperature use. Crystals with high anisotropy in thermal expansion are prone to cracking during growth and processing, which can shorten the lifespan

of crystal components and lower the damage threshold of laser gain media. To alleviate these issues, laser systems typically incorporate effective cooling solutions and use materials with low thermal expansion coefficients. For garnet crystals, α is measured along the [111] direction. As depicted in Figure 2.21, garnet crystals like YAG, GGG, and YSGG, etc., are characterized with relatively low thermal expansion compared to other laser crystals [109,110] making them suitable for efficient laser operation under strong pumping conditions.

In solid-state lasers, uneven temperature distribution within the gain medium due to asymmetrical cooling may cause thermal stress (strain and compression) causing eventually its cracking. This temperature variation alters the refractive index via the medium's thermo-optic coefficient, resulting in a significant thermal lens effect that restricts laser output power and beam quality [109,111]. For garnet crystals used in lasers, thermal conductivity is a critical physical property. As shown in Table 2.1, at room temperature and 1000 K, YAG has higher thermal conductivity than GGG, while YSGG surpasses GSGG. This is because oxides with smaller cation atomic masses have greater thermal conductivity than those with larger masses.

Table 2.1 Thermal conductivities for some garnet crystals at RT and 1000 K [108].

k [W m^{-1} K^{-1}]	YAG	GGG	YSGG	GSGG	GYSGG
298 K	11.72	8.98	6.83	5.45	4.66
1000 K	3.26	2.39	2.46	2.30	2.01

The optical characteristics of laser gain media are essential parameters to consider. According to Figure 2.21, the transmission curves of undoped garnet crystal hosts at room temperature show clear transparency within the 320–3000 nm wavelength range. Their high transparency makes them ideal candidates for laser hosts in the visible and infrared ranges.

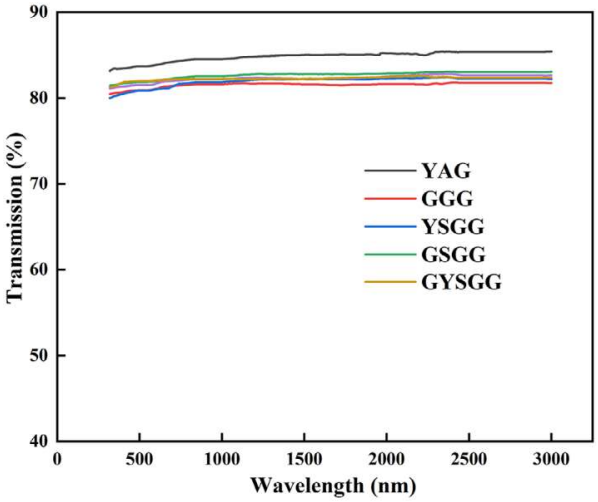

Figure 2.21. Transmission for several undoped garnet crystals [108].

2.3.2. Alkali rare-earth double molybdates, $MRE(MoO_4)_2$

The alkali (A^+) and rare-earth (RE^{3+}) double tungstates and molybdates, with the chemical formula $A^+RE^{3+}(XO_4)_2$ where X represents either tungsten (W) or molybdenum (Mo) [112], are particularly suitable for doping with active rare-earth ions for laser applications. These crystals boast a diverse range of structural types, including disordered forms, and offer several notable benefits [113,114]. Firstly, they contain substitutional rare-earth sites that allow for

high concentrations of laser-active RE^{3+} ions to be doped. Secondly, they exhibit strong anisotropy of their spectroscopic properties when interacting with polarized light. Thirdly, the large distances between RE^{3+} ions in their structure minimize the interaction among each other, leading to reduced concentration quenching and minimal non-radiative relaxations. Additionally, these materials are Raman-active, enhancing their suitability for various optical applications [115,116].

A prominent example of this class are the potassium rare-earth double molybdate crystals. These crystals exhibit various crystallographic structures (polymorphism). Recent studies conducted on the structure of these compounds using X-ray diffraction have identified several possible structures: $CaWO_4$ (scheelite): $I4_1/a$; α-$KBi(MoO_4)_2$: $P2_1/c$; $KY(MoO_4)_2$: *Pbna*; $KEu(MoO_4)_2$: $P\bar{1}$; $KAl(MoO_4)_2$: $P\bar{3}m1$; $KIn(MoO_4)_2$: *Pnam*.

The following phase diagram (Figure.2.22) summarizes the temperature conditions required to obtain each of the structures and the doping conditions with rare-earth ions, based on the distribution of the ionic radii of the dopant ions [117].

This detailed examination of the potassium rare-earth double molybdates is crucial for understanding their structural diversity. The identified crystallographic phases, such as scheelite-type $CaWO_4$ with space group *I41/a*, and the various others like α-$KBi(MoO_4)_2$ with space group *P21/c*, demonstrate the complexity and variability within this family of compounds. The study's findings provide insight into the specific temperature and doping conditions necessary to synthesize each unique structure, thereby enhancing our ability to tailor these materials for specific applications.

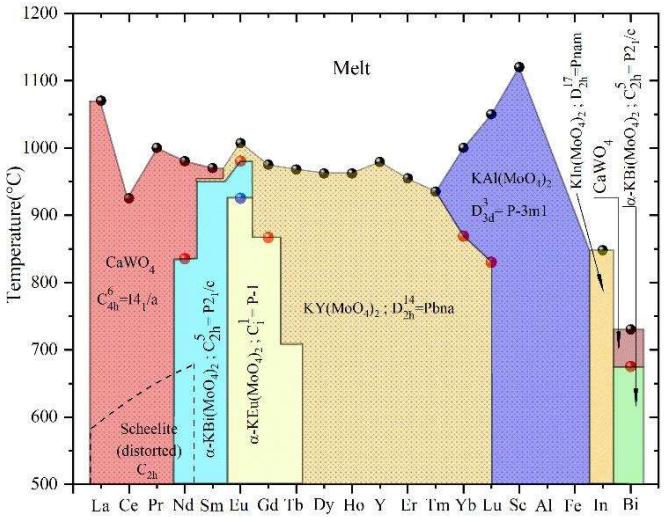

Figure.2.22. Phase Diagram of Potassium Double Molybdates.

The potassium-yttrium double molybdate, KYMo [$KY(MoO_4)_2$], crystallizes in the orthorhombic system with the space group *Pbna*. Its structure is similar to the monoclinic double molybdates, featuring an ordered arrangement of cations. In this structure, Y^{3+} and K^+ ions occupy distinct atomic sites. The Y^{3+} ions, coordinated by eight oxygen atoms, are in a C_2 symmetry site, with the symmetry axis perpendicular to the (001) axis. The YO_8 octahedra align parallel to the (010) axis, connecting through shared edges. The Mo^{6+} ions reside at the center of irregular tetrahedra, surrounded by four oxygen atoms, and these tetrahedra connect to the YO_8 octahedra by sharing vertices. This connection forms a layer parallel to the **b**-axis,

consisting of the $[Y(MoO_4)_2]^-$ radical. The layers, spaced approximately <a/2> apart, are interconnected by KO_6 octahedra, as depicted in Figure 2.23.

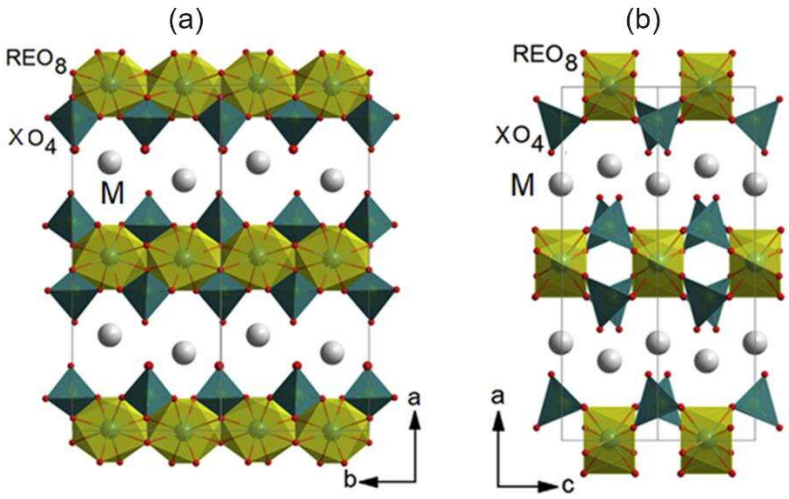

Figure.2.23. Orthorhombic structure (Pbna) of KYMo crystal. Projections on the (a) **a-b** and (b) **a-c** planes.

Initial research on KYMo crystals concentrated on their structural characteristics. Subsequently, studies reported the laser activity and spectroscopy of Nd^{3+}-doped KYMo crystal [118]. The crystals' layered structure results in perfect cleavage, which limits their use in bulk lasers. Nevertheless, this property led to the proposal of thin-film lasers using KYMo materials. Detailed investigations into the vibronic properties of undoped KYMo crystals were also conducted. Additionally, doped variants with Dy^{3+}, Pr^{3+}, Er^{3+}, and Tm^{3+} ions have been documented [119–122].

In this thesis, cesium-based alkali rare-earth double molybdate crystals have also been explored, denoted as $CsRE(MoO_4)_2$, known for their "loose" structures that facilitate unique properties such as strong acousto-optic coupling, high magnetic anisotropy, and mica-like natural cleavage. These features make them suitable for various applications. For instance, crystals with layered structures provide strong anisotropy in spectroscopic properties and easy mechanical cleavage, making them ideal for thin-film and microchip lasers. $CsRE(MoO_4)_2$ exemplify this class and crystallize in the monoclinic system, with a specific space group of *P2/c* for RE elements ranging from Ce to Lu, as illustrated in Figure 2.24.

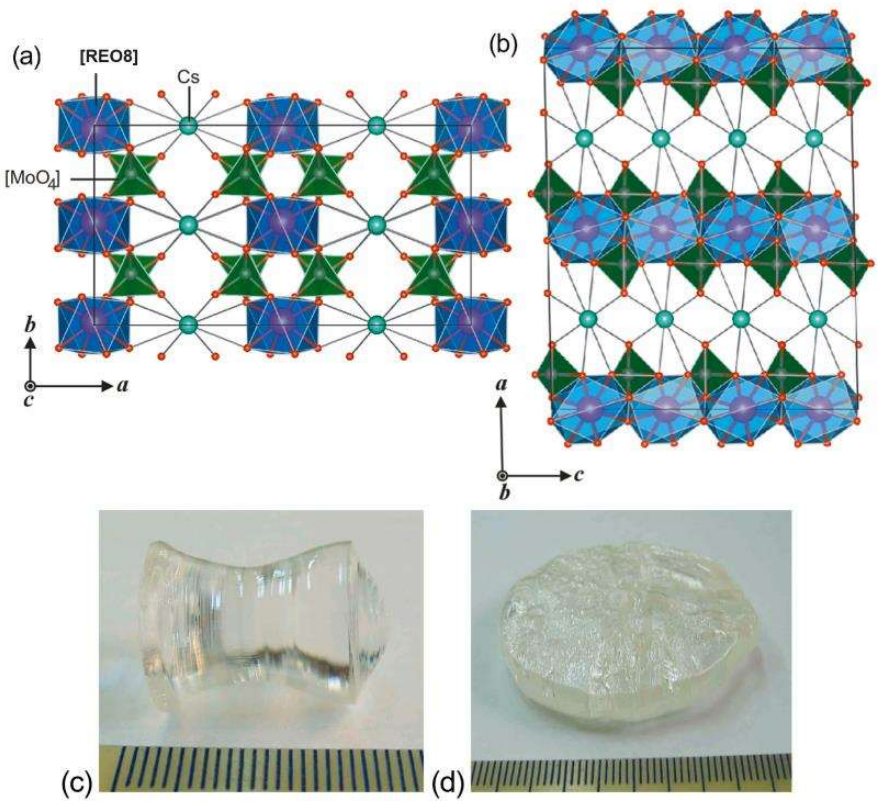

Figure.2.24. Crystal structure of CsREMo: a supercell (2a ×2b ×2c) in projection on (a) **a-b** plane, (b) **a-c** plane; Photographs of as-grown undoped CsGdMo crystal: (c) [100] direction and (d) Growth on a Pt wire − Growth with low thermal gradient Czochralski method [123] .

Limited studies have focused on $CsGd(MoO_4)_2$-type crystals (abbreviated as CsGdMo). *Klevtsova et al*.[124] briefly described the crystalline structure of $CsPr(MoO_4)_2$, representative for the rare-earths ranging from Ce to Lu. Research by *Ivannikova et al.* [125] on undoped CsGdMo involved growing the crystals through Czochralski processes. *Klevtsov et al.*[112] provided a summary of the structural diversity among $CsRE(MoO_4)_2$ (RE = La to Lu, In, Sc, Fe, Cr, Al) crystals. *Pavlyuk et al*.[126] documented the laser emission characteristics of $CsNd(MoO_4)_2$ crystal under Ruby laser pulsed pumping, highlighting an emission wavelength of 1065.8 nm and a laser threshold of 49 mJ during ns pulse excitation. The material's structure, which results in weak concentration quenching, enables high-efficiency laser emission even with 100 at.% Nd^{3+} content. Originally, the structural type of $CsPr(MoO_4)_2$ was categorized as orthorhombic, and recent developments have seen a surge in interest in CsGdMo, notably in studies like those by *Zhao et al.* [127] on Yb^{3+}-doped specimens focusing on growth and polarized optical spectroscopy.

2.3.3. Calcium rare-earth orthoborate, $Ca_3RE_2(BO_3)_4$

Borates are highly regarded as laser hosts due to their favorable chemical and physical properties, including a relatively high damage threshold. The double borate family of crystals, $Ca_3RE(BO_3)_4$ (where RE stands for La, Gd, or Y), are promising materials for this purpose. They feature appropriate hardness, robust chemical stability, and are moisture-resistant. Additionally, these crystals have a congruent melting point, allowing them to be efficiently

grown using the Czochralski method. This facilitates the production of high optical quality crystals with large dimensions, as illustrated in Figure 2.25.

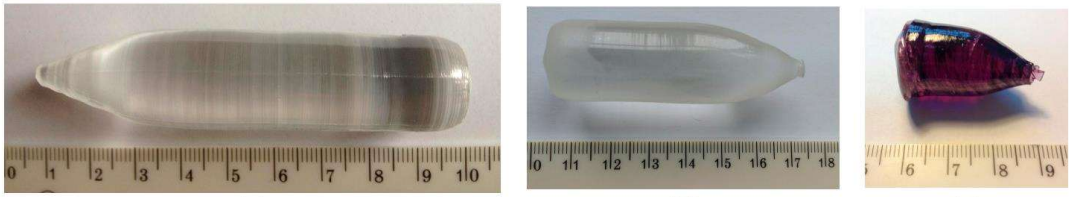

Figure.2.25 Example of large-size calcium rare earth borate crystals obtained with the Czochralski method: (a) $Ca_3Y_2(BO_3)_4$ crystal grown in argon using Ir crucible; (b) $Ca_3Gd_2(BO_3)_4$ crystal grown in air using Pt crucible; (c) $Ca_3Nd_2(BO_3)_4$ crystal grown in argon using Ir crucible [128].

Figure 2.26 illustrates the packing diagram of units cell in the $Ca_3RE_2(BO_3)_4$ crystal. The structure of $Ca_3Y_2(BO_3)_4$ features cations occupying three distinct statistical sites, like in $Ca_3La_2(BO_3)_4$ and $Ba_3La_2(BO_3)_4$ [129]. This structure includes three types of distorted M-oxygen polyhedrons and three sets of BO_3 planar triangles, with Ca^{2+} and Y^{3+} ions statistically distributed across these three sites, labeled M1, M2, and M3. Each site is coordinated by eight oxygen ions, forming distorted polyhedra. The electronic density values and the ion charges of Ca^{2+} and Y^{3+} allow for the calculation of their ratios at each site: M1 is composed of 0.61 Y and 0.39 Ca, M2 has 0.445 Y and 0.555 Ca, and M3 contains 0.25 Y and 0.75 Ca. RE^{3+} ions can substitute for Y^{3+} ions in these sites, and the statistical variation in the distribution of Ca^{2+}, Y^{3+}, and RE^{3+} ions may cause a broadening in the spectral width of the crystal.

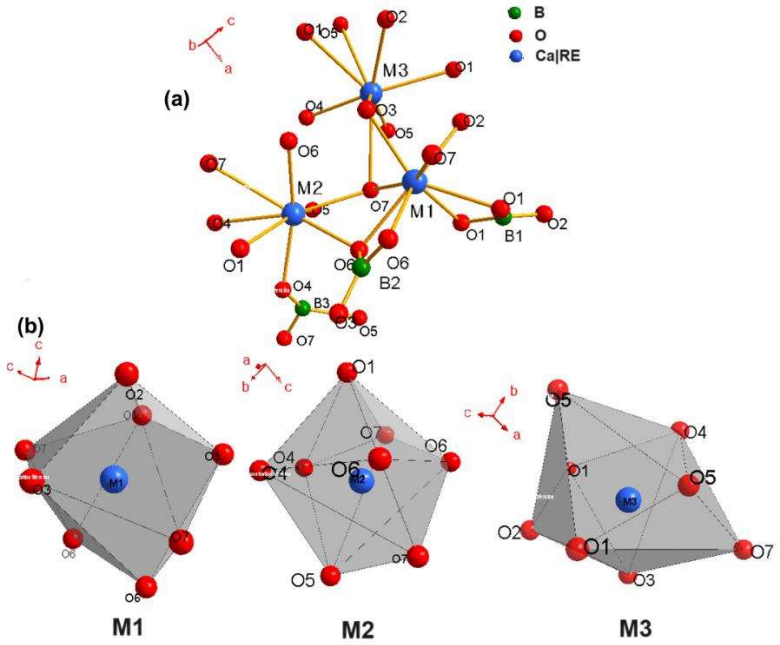

Figure 2.26. (a) Crystal structure of $Ca_3RE_2(BO_3)_4$; (b) coordination environments of the M1, M2, and M3 sites for the Ca^{2+} and RE^{3+} ions [128].

For $Ca_3RE_2(BO_3)_4$ (RE = Y, Gd, Nd) borate crystals, the thermal conductivity reduces with temperature, showing a decrease of about 15% across the series from Y to Nd, detailed in Figure 2.27. The absolute thermal conductivity values and their dependence on temperature are similar

to those typically seen in glasses. These thermal properties make these borate crystals viable options as potential laser materials, especially considering their capacity for heat dissipation during laser operation.

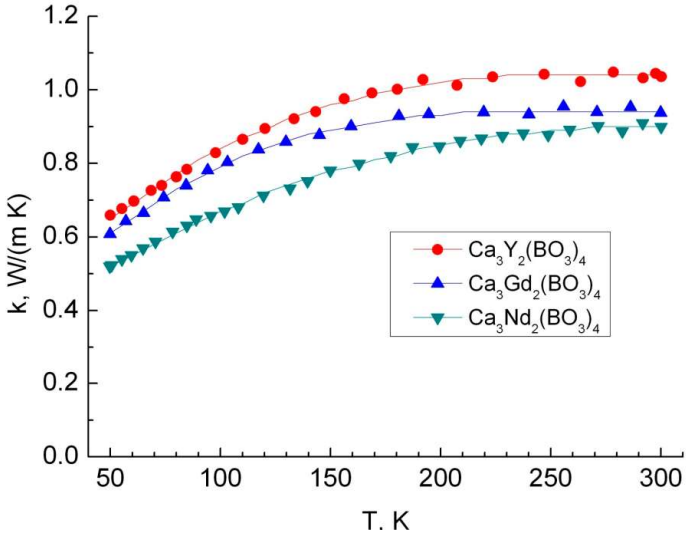

Figure 2.27. Temperature dependence of the thermal conductivity *k* for $Ca_3RE_2(BO_3)_4$ (RE = Y, Gd, Nd) crystals along the **c** axis [128].

2.3.4. Fluoride crystals

Fluoride crystals, such as Lithium Yttrium Fluoride ($LiYF_4$), Calcium Fluoride (CaF_2) and Barium Yttrium Fluoride (BaY_2F_8), have emerged as crucial laser hosts materials in the field of laser technology, offering unique properties that make them indispensable for various high-performance laser applications. These crystals, characterized by (i) their wide transparency range from the ultraviolet to the mid-infrared spectrum, typically spanning from 0.2 to 10 µm. This broad range allows for the generation and transmission of laser light across multiple wavelengths. (i) The low phonon energies of fluoride crystals (typically <500 cm^{-1}) reduce non-radiative transitions, leading to higher quantum efficiencies and enabling efficient laser operation at longer wavelengths. (iii) High Damage Threshold: many fluoride crystals possess high laser-induced damage thresholds, making them suitable for high-power laser systems. And (iv) Diverse Dopant Compatibility: Fluoride crystals can be doped with various RE ions, allowing for a wide range of lasing wavelengths and applications.

Lithium Yttrium Fluoride ($LiYF_4$), or YLF, is a notable crystalline material in solid-state laser technology, particularly valued as a laser gain medium when doped with rare earth ions. In this thesis we explored the cryogenic laser operation a Tm-doped YLF crystal, so in the following discussion we presented some key proprieties of this crystal including the crystal structure, anisotropic properties, thermo-optic characteristics, and thermal properties of YLF, underscoring its significance in laser applications.

YLF crystallizes in a tetragonal scheelite structure with lattice parameters of approximately a = b = 5.16 Å and c= 10.74 Å, exhibiting S_4 symmetry along the **c**-axis which leads to significant anisotropy in optical and thermal properties. The crystal structure of YLF is presented in Figure 2.28(a). RE^{3+} ions are doped in the YLF crystal in an orderly manner

and selected to replace the position of Y^{3+} (0.9 Å) ions because their ion radii are similar in size. At the same time, Er^{3+} ions occupy the crystallographic site of the S_4 symmetry [130]. YLF crystal could be easily grown by the Cz method in an inert gas environment like argon or nitrogen, Figure 2.28(b)

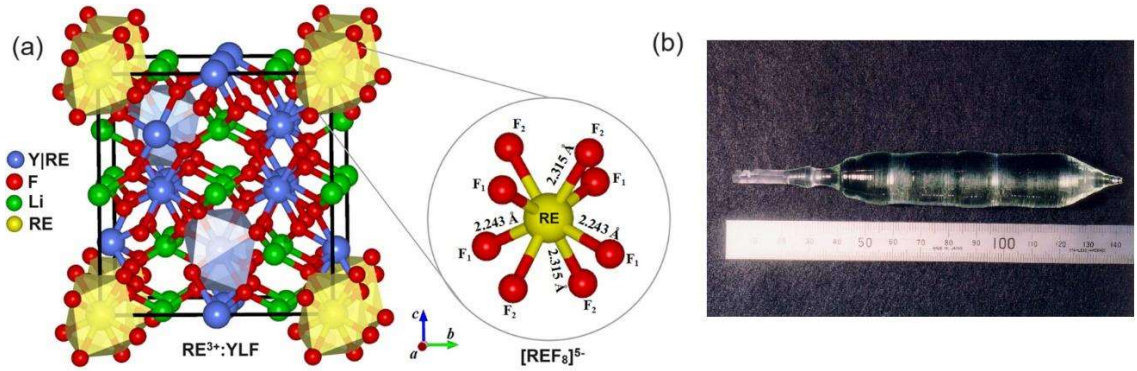

Figure 2.28. (a) View of the three-dimensional (3D) structure of RE^{3+}-doped $LiYF_4$[130]; (b) sample of undoped YLF crystal grown by Cz method [131].

YLF is a negative uniaxial crystal where absorption and emission spectra vary significantly for light polarized parallel (π) or perpendicular (σ) to the **c**-axis . the crystal has a birefringence ($\Delta n = n_e - n_o$) of around 0.02 and shows pronounced polarization-dependent absorption and emission. Its ordinary refractive index (n_o) = 1.45 and the extraordinary one is (n_e) ≈ 1.47. Thermo-optically, it has coefficients of $dn/dT_{(\pi)} = -4.3 \times 10^{-6}\ K^{-1}$ and $dn/dT_{(\sigma)} = -2.0 \times 10^{-6}\ K^{-1}$, which mitigate thermal lensing effects[132,133]. YLF exhibits weak thermal lensing compared to many oxide crystals. This property allows for better beam quality in high-power laser operations.

Thermally, YLF has a thermal conductivity of approximately 6 W/(m·K), moderate thermal shock resistance, and a melting point of around 819°C [131]. These properties make it suitable for high-power laser systems, including Nd, Er, Tm, Ho, and Yb lasers, each utilizing its distinct emission wavelengths for various applications, from high-energy pulsed systems to medical and sensing technologies. The combination of its unique anisotropic, thermo-optic, and thermal properties establishes $LiYF_4$ as a premier host material in the realm of solid-state lasers.

CHAPTER 3

CHAPTER 3: Experimental techniques

The experimental techniques used for growing and characterizing the laser crystals studied in this work are discussed in this chapter. The Optical Floating Zone Growth method implemented for growing the Yb-doped yttrium gallium garnet crystals (Yb:YGG) as well as the conventional Czochralski (CZ) ,used for the growth of the Yb-doped YLuAG crystal−Tm:CLTGG crystal− the garnet Tm,Ho-doped CNGG crystal− Tm:YLF crystal and the borate Yb:GdCB crystal, and its advanced version, the Low Thermal Gradient Czochralski (LTG-CZ), implemented for fabricating of the double molybdates gain media (Yb:KYMo, Tm: KYMo and Nd:CsGdMo) are described. Furthermore, structural, spectroscopic, and microscopic characterizations of the laser crystals are addressed. Finally, the techniques and experimental setup used for laser experiments are described.

3.1. Crystal growth methods

3.1.1. Optical Floating Zone Growth.

A variety of optical floating zone (OFZ) furnaces are available on the market, each offering distinct configurations designed to meet specific research and industrial needs. These furnaces typically feature either a two-mirror or four-mirror setup, where the mirrors are ellipsoidal in shape to precisely focus the energy onto the material being processed. The energy sources used in these systems are either incandescent tungsten halogen bulbs or xenon arc lamps, both of which are chosen for their ability to efficiently generate infrared energy. This infrared energy is particularly effective for heating because most oxide materials have a high absorption rate in this wavelength range, allowing for uniform and controlled heating. In recent advancements, OFZ furnace technology has begun to incorporate infrared laser diodes as a new energy source. This emerging technology offers several advantages, including enhanced control over the heating process and the potential for more efficient energy usage. The incorporation of infrared laser diodes also enables the development of innovative optical designs within the OFZ systems, allowing for even greater precision and flexibility in materials processing. These advancements in optical and energy source design reflect ongoing efforts to optimize OFZ furnaces for a wider range of applications [134–136]. More detailed information about commercially available furnaces can be found in references [137–139] and on the websites of various manufacturers.

Modern furnaces are now equipped with advanced technology, including high-resolution video cameras that allow researchers to observe the crystal growth process in real-time. This feature is crucial for monitoring the intricate details of the growth phase, ensuring that any irregularities or issues can be detected and addressed promptly. Moreover, many of these furnaces are integrated with remote control systems accessible via the Internet. This connectivity provides a significant advantage, particularly during long-duration experiments, as it allows scientists to adjust and fine-tune the growth conditions from any location. This remote capability not only enhances the precision of the experiment but also improves efficiency by reducing the need for constant on-site supervision, thus facilitating more effective management of the crystal growth process over extended periods.

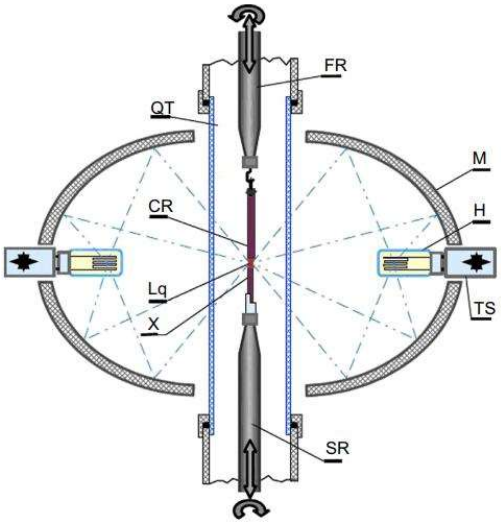

Figure 3.1. A schematic illustration of the OFZ setup includes the following components: M represents an elliptical mirror, H denotes an halogen tungsten lamp, TS is the x-y-z micrometer translation stage used for filament adjustment, QT stands for the vitreous silica tube (quartz glass), FR refers to the upper translation/rotation rod, CR is the ceramic feed rod, Lq signifies the liquid bridge or floating zone, X indicates the seed rod and crystal, and SR is the lower translation/rotation rod [140].

The OFZ setup is shown in Figure 3.1. In this crystal growth process, two ceramic rods meet at the focal point of ellipsoidal mirrors inside a fused silica tube, which controls the growth atmosphere. Halogen or xenon lamps are placed at the other focal points. Crystal growth begins by melting the rod tips to create a liquid bridge, or "floating zone," between the seed (bottom) rod and the feed (top) rod. This zone is moved upward by either lowering the rods or raising the mirrors [141]. As it moves, the melt cools and crystallizes on the seed rod, with the grain having the highest radial growth velocity continuing to develop.

In this thesis, the OFZ method was utilized to grow the crystal gallium garnet Yb:YGG crystal gallium garnet crystals. A detailed description of the growth process for these crystals can be found in the corresponding papers.

Success of the growth depends on the material quality, initial rod shape, and precise alignment of the seed and feed rods. The seed rod is securely fixed, while the feed rod can move independently. If the feed rod is rigidly mounted, high-quality, straight, and dense ceramic materials are needed, along with precise alignment. Starting with a crystalline, oriented seed aids in initial crystallization and prevents the molten liquid from being absorbed into a porous rod. However, oriented seeds are rarely available, so new material crystals are typically grown on ceramic seeds (figure 3.2) produced through a lengthy grain segregation process [141].

The stability of the growth process relies on material quality, starting rod shape, and precise alignment of the seed and feed rods. The seed rod is fixed to the lower shaft, while the feed rod can be adjusted vertically. The feed rod may be rigidly attached or loosely suspended.

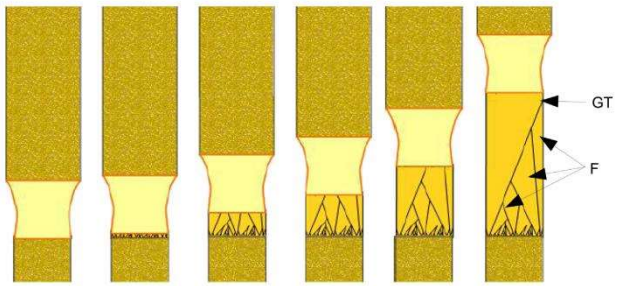

Figure 3.2. Schematic of the nucleation stages on ceramic rods and grains expansion. Individual grains can exhibit facets (F) on the crystal lateral side. After last secondary grain termination (GT), single crystal continues to grow [142].

3.1.2. Czochralski crystal growth

The Czochralski (Cz) crystal growth process, developed almost a century ago, [143] is a leading method in crystal growth. It is renowned in academia for precisely forming single-crystal cylindrical ingots of inorganic scintillating crystals, laser gain materials and is also applicable to organic crystals. This technique is used for growing semiconductors, oxides, fluorides, other halide crystals, and metals. Today, it is the main industrial method for producing nearly all congruently melting semiconductor materials and many oxide crystals.

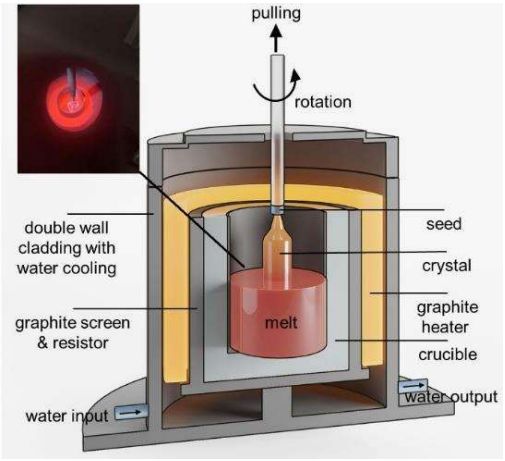

Figure 3.3. Schematic diagram of the Cz crystal growth process

Despite its apparent simplicity (as shown in figure.3.3 and 3.4), the Cz process requires precise control over many factors that impact crystal quality and commercial viability, as listed in Table 3.1. Most reports on the Cz growth of certain crystals lack detailed accounts of these variables. Therefore, the summary of growth results below is not a comprehensive description of the technology. However, many aspects of the crystal growth process are consistent and can be anticipated based on prior experience with other crystals, [144–146].

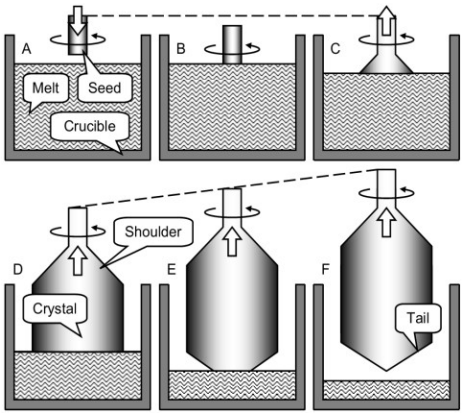

Figure 3.4. The Cz method involves few steps: (A) bringing the seed crystal near the overheated melt, (B) immersing the seed into the melt for thermal equilibration, (C) pulling the seed upward and increasing the crystal diameter to form the shoulder, (D) pulling the crystal to keep a constant diameter, (E) gradually decreasing the diameter to finish growth, and (F) separating the crystal from the melt and cooling it to room temperature [147].

Table 3.1. Cz growth parameters.

Item for Control	Details
Crucible	Material composition, corrosion, melting point, shape and dimensions, contaminations, rotation, displacement, etc.
Atmosphere	Composition, pressure, flow rate, etc
Seed	Structure, composition, orientation, dimensions, shape, etc.
Pulling	Pulling rate, rotation (rate, acceleration, direction) etc.
Thermal aspect	Heating source and its power, hot zone design and insulation materials, temperature gradients, automatic diameter control, etc.
Cost efficiency	Melt solidification fraction, cost of the crucible and the melt ingredients, cost of apparatus, time consumption for the preparation of starting materials, total time of the growth process and energy costs, etc.

In the CZ technique, undoped materials typically grow at a few millimeters per hour, but doped materials, especially for laser applications like neodymium-doped YAG, require slower growth rates of a few tenths of a millimeter per hour to avoid defects and ensure uniform dopant distribution. For thermally sensitive crystals like $LiNbO_3$ or $LaTiO_3$, an auxiliary annealing furnace may be used. Growth conditions vary by crystal type, and the CZ method is versatile, producing a wide range of single crystals, including: aluminates ($YAlO_3$, $LaMgAl_{11}O_{19}$), silicates (Y_2SiO_5, Gd_2SiO_5, Lu_2SiO_5), germanates ($Bi_4Ge_3O_{12}$, $Bi_{12}GeO_{20}$), vanadates (YVO_4), borates ($YCa_4B_3O_{10}$, $GdCa_4B_3O_{10}$), tungstates ($CaWO_4$), and fluorides (notably $LiYF_4$) [148–151]. In this work, the CZ technique has been used to grow the following crystals: Yb-doped the compositionally mixed YLuAG crystal−Tm:CLTGG crystal− the garnet Tm,Ho-doped CNGG crystal− Tm:YLF and the borate Yb:GdCB crystal. The growth process for these crystals is thoroughly explained in the related papers.

3.1.3. Low Thermal Gradient Czochralski Method.

The Low Thermal Gradient Czochralski (LTG-Cz) method (an example of LTG-Cz furnace is shown in figure 3.5) is a refined version of the conventional Cz process characterized by maintaining a significantly lower temperature gradient between the melt and the growing crystal. This method involves precisely controlling the thermal environment around the crystal growth zone to minimize thermal stress and reduce the occurrence of defects. Here's a detailed breakdown of its key aspects [152–154]:

- Reduced thermal gradient: In the LTG-Cz method, the temperature difference between the molten material and the crystallizing solid is carefully minimized. This is achieved by optimizing the heating elements, insulation, and crucible design to ensure a more uniform temperature distribution.
- Annealing furnace integration: For materials sensitive to thermal shocks, such as lithium niobate ($LiNbO_3$) or lanthanum titanate ($LaTiO_3$), an auxiliary annealing furnace is often integrated into the system. This helps to gradually cool the crystal and further reduce thermal stresses.
- Improved crystal quality: By reducing the thermal gradient, the LTG-Cz method helps in minimizing local supercooling phenomena, known as striations, which are common defects in crystals grown by the traditional Cz method. This leads to the production of crystals with higher structural integrity and uniformity.
- Homogeneous dopant distribution: For doped crystals, especially those used in laser applications (e.g., Nd-doped YAG), maintaining a low thermal gradient ensures a more uniform distribution of dopants. This is crucial for achieving high laser performance.

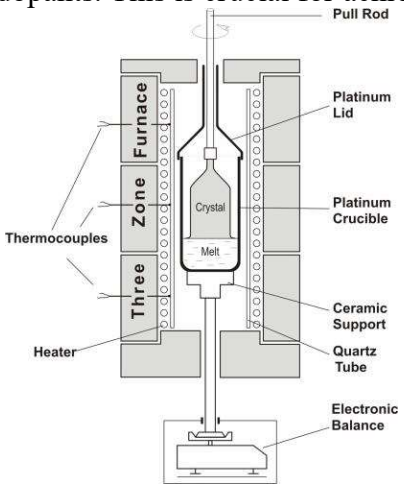

Figure 3.5. Scheme of the furnace for LTG-Cz technique [154].

The LTG-Cz method is especially advantageous for growing a diverse array of laser crystals, including garnets , silicates, germanates, molybdates, borates, tungstates, and fluorides[152]. These materials are highly valued in various laser systems due to their superior optical properties and stability. In this thesis, LTG-Cz method was used to grow the double molybdates gain media (Yb:KYMo, Tm: KYMo and Nd:CsGdMo)

In summary, the Low Thermal Gradient Czochralski method marks a significant advancement in crystal growth technology for laser applications. By meticulously controlling the thermal environment, this technique yields high-quality crystals with fewer defects and a more uniform distribution of dopants, thereby enhancing the performance of laser devices.

3.2. Crystal orientation

Many host crystals in this study lack a cubic structure and must be properly oriented for polarization-dependent spectroscopy. Optics involves studying how light changes when it enters and exits a material, focusing on variations in refractive index. Crystals are classified as isotropic if the refractive index is constant in all directions, and anisotropic if it varies with the direction of light propagation.

Anisotropic crystals are categorized into uniaxial (one optic axis) and biaxial (two optic axes) groups. An optic axis is a direction where light does not experience birefringence. When light travels in other directions, it splits into orthogonally polarized ordinary and extraordinary rays. Crystals in this thesis are also classified by crystallographic principles, described as periodic structures defined by repeatable fundamental cells with vectors and lengths a, b, and c.

A cubic crystal has equal lattice parameters lengths (a = b = c) and 90° angles between them. In a tetragonal system, a = b ≠ c with 90° angles. Hexagonal and trigonal crystals have a = b ≠ c with 90° angles for α and β, and 120° for γ. Orthorhombic crystals have different edge lengths (a ≠ b ≠ c) but 90° angles. The monoclinic system also has different edge lengths (a ≠ b ≠ c) with α = β = 90° and γ ≠ 90°. In the triclinic system, all edge lengths and angles are different.

The relationship between these classifications can be summarized as follows:

- Cubic systems are uniquely isotropic.
- Hexagonal, trigonal, and tetragonal systems have a **c**-axis as their source of anisotropy and optic axis, making them uniaxial crystals.
- Orthorhombic, monoclinic, and triclinic systems, which exhibit higher levels of anisotropy, possess two optic axes, and are referred to as biaxial crystals.

To determine the **c**-axis orientation in a uniaxial crystal that coincides with the π polarization, unpolarized light is used with two crossed polarizers. The first polarizer filters the light to vibrate parallel to its direction, and the second polarizer, oriented perpendicularly, causes light extinction. When the crystal is placed between them and rotated, light transmission varies.

In an isotropic crystal, when the crystal is placed between two crossed polarizers, light transmission remains unchanged regardless of rotation, resulting in zero transmission. However, an anisotropic crystal shows birefringence, allowing some light to pass through the analyzer based on the crystal's orientation during rotation.
For a uniaxial crystal, if the optic axis aligns with the light direction, the crystal acts isotropically, and light transmission is zero regardless of rotation. If the optic axis is not parallel, light passes through the second polarizer used as an analyzer, and transmitted intensity varies with rotation. A conoscopic lens between the crystal and the second polarizer can reveal the crystal axis direction through the emerging interference figure.
When the crystal is biaxial, a mere analysis of the polarization changes of the transmitted light is usually not enough to determine precisely the position of the optic axes. For that reason, there is another setup could be used consisted of a system of crossed polarizes coupled to Polarized Light Microscope equipped with a rotating stage and a conoscopic lens.

For crystallographic orientation, micro-X-ray diffraction (μXRD) was employed in this thesis for precise crystal orientation . μXRD determines an X-ray diffraction pattern (figure 3.6) based on crystal symmetry using a collimated, broad-spectrum X-ray beam. The crystal remains stationary, and specific wavelengths in the beam meet Bragg's law conditions for constructive interference.

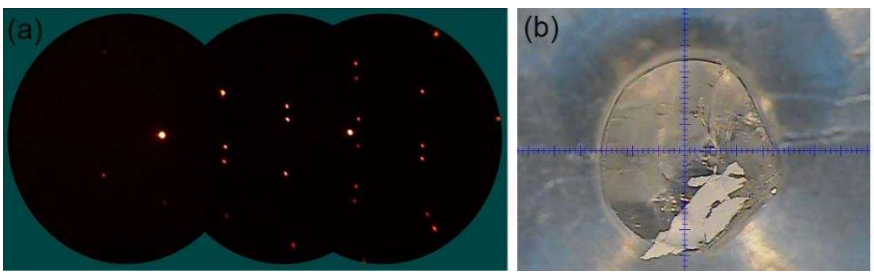

Figure 3.6. (a) General area detector diffraction system image exhibiting diffraction spots. (b) Image of a crystal collected at χ: 90°.

At the *Serveis de Recursos Cientifics i Tècnics* (*SRCiT*) of the URV, XRD measurements were performed using a Bruker-AXS D8-Discover diffractometer. This device features a parallel

incident beam, a vertical θ-θ goniometer, an XYZ motorized stage on a ¼ Eulerian cradle, and a General Area Diffraction System (GADDS). Samples are placed on the holder, and the area of interest is targeted with a video-laser focusing system. The X-ray collimator analyzes areas as small as 500 µm. Operating at 40 kV and 40 mA, it generates Cukα radiation. The VÅNTEC-500 GADDS detector, positioned 15 cm from the sample, collects frames in omega-scan mode (2D XRD patterns) over ~5-90° 2θ, with 60 seconds per frame. These frames are chi-integrated into conventional 2θ vs. intensity diffractograms. The diffraction peaks' coordinates in reciprocal space are used to calculate lattice parameters in real space, analyzed by computer programs. A few diffraction patterns with different orientations typically suffice to determine the crystal's exact crystallographic axes, essential for cutting and polishing samples for polarization-dependent spectroscopic or laser experiments.

3.3. Samples cutting and polishing

This process is conducted in two phases: the first phase involves cutting and shaping, while the second phase focuses on polishing. Both stages are performed in FiCMA's laboratory. Initially, the as-grown crystal is roughly cut using a disk saw, and then shaped to precise dimensions with a stainless-steel wire saw utilizing an abrasive fluid. The crystal can be formed into parallelepiped shapes, potentially cut at Brewster's angle for bulk crystals, or into thin slices a few millimeters thick. Subsequently, these shaped crystals are polished using a Logitech PM5 polisher, as shown in Figure 3.7(a).

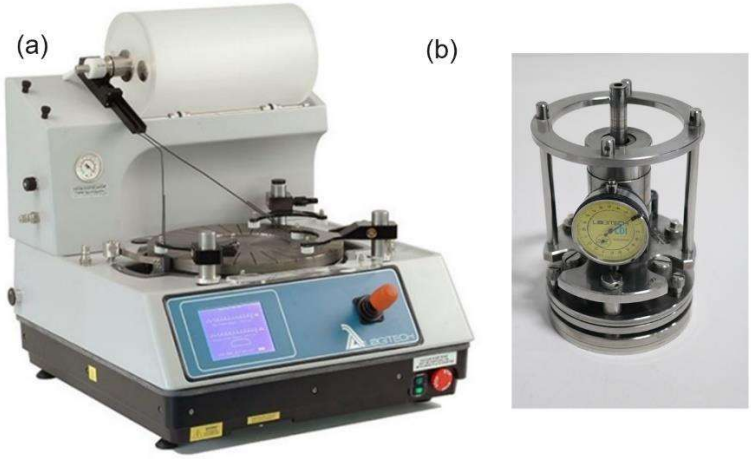

Figure 3.7. (a)Lapping and polishing machine (PM5 from Logitech; (b) Logitech Precision JIG

We start by mounting the crystal sample in the JIG device shown in Figure 3.7(b) and then place it into the Logitech PM5. The lapping process begins with a coarse alumina solution with a grain size of 9 µm, followed by a finer 3 µm alumina solution. After each step, the crystals are polished using a 1 µm deagglomerated calcined alumina solution. Figure 3.8 illustrates the surface condition of a garnet crystal under an optical microscope, both before and after polishing with the 1 µm deagglomerated calcined alumina solution. Sometime depend on the processed material, polished using 0.3 µm alumina solution is needed to get very high surface quality.

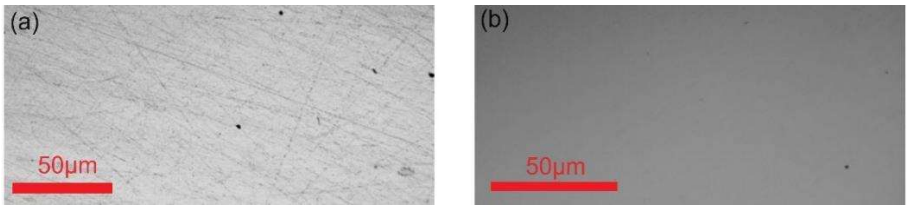

Figure 3.8. Crystal before and after polishing with a 1 µm deagglomerated calcined alumina solution.

3.4. Overview of characterization techniques

Various techniques have been applied to study the properties of materials, including physico-chemical and microstructural characterizations, as well as optical spectroscopy. They are listed in Table 3.2

Table 3.2. Summary of characterization methods used to study RE^{3+}-doped materials in this thesis.

Method	Abbrev.	Purpose
Structural characterization		
Powder X-ray diffraction	XRPD	Phase identification
Rietveld analysis		Structure refinement
Temperature-dependent XRD		Thermal expansion
Differential thermal analysis	DTA	Thermal behavior. Phase changes
Electron probe micro-analysis	EPMA	Dopant ion density
Micro-X-ray diffraction. Reciprocal space mapping. Rocking Curves	µXRD / RSM / RC	Microstructural characterizations: Phase and crystallographic orientation confirmation / lattice parameters and Lattice mismatch
Energy-Dispersive X-ray spectroscopy	EDX	Element mapping
Scanning electron microscopy	SEM	Morphology and Structural study
Confocal and Interferometric laser microscopy		Morphology and Structural study / Roughness measurements
Raman spectroscopy		Vibronic properties
Optical characterization		
Absorption spectroscopy		Absorption cross-section
Luminescence spectroscopy		Stimulated emission cross-sections
Luminescence kinetics		Luminescence lifetimes
Low-temperature spectroscopy	LT	Crystal-field splitting
Judd-Ofelt analysis	J-O	Transition probabilities

3.4.1. Structural characterization

3.4.1.1. X-ray diffraction

X-ray diffraction (XRD) is a nondestructive analytical technique used to study the atomic structure of crystalline materials. When X-rays of a specific wavelength strike a crystal, they interact with the regularly spaced atoms in its lattice, causing the atoms to vibrate and emit scattered X-rays. These scattered X-rays interfere both constructively and destructively, creating a distinct diffraction pattern that reveals information about the atomic arrangement within the crystal. This pattern appears as a series of spots or peaks on a detector, with their positions and intensities providing valuable insights into the lattice parameters, symmetry, and crystallographic orientation of the crystal.

By analyzing the diffraction pattern, the crystal structure is determined, its unit cell dimensions and atomic positions, which are crucial for understanding the material's properties and behavior. XRD is generally classified into three main types: single-crystal diffraction, powder X-ray diffraction, and micro-X-ray diffraction:

- Micro-X-ray diffraction (µXRD) provides detailed information about the atomic arrangement within a crystal, including precise bonding distances, angles, and molecular conformations. By rotating the crystal and collecting data from various crystallographic orientations, µXRD is typically used to determine lattice parameters, crystalline quality (mosaïcity), and crystallographic orientation. The resulting diffraction patterns are collected in reflection on the detector, appearing as a distribution of spots in reciprocal space. Each spot corresponds to the reflection of a family of

crystallographic planes, identified by their Miller Indices (hkl). The experimental setup was detailed in the previous section.

- Powder X-ray Diffraction (XRPD): XRPD is utilized for phase analysis of crystalline samples, including determining their crystalline nature, phase composition, and grain size measurements. This technique requires a polycrystalline sample with small, randomly distributed grain sizes. A fine powder of the material, consisting of numerous microcrystalline domains in random orientations, is created by finely milling the crystalline samples. When X-rays pass through this powder, they are diffracted by various crystalline domains, creating a diffraction pattern of rings on the detector. These rings correspond to different crystallographic planes within the powder. By analyzing this pattern, information about the crystal microstructure can be obtained and phase composition (nature, dosage, and size of the crystallites). For XRPD, it is common for the X-ray beam to be not perfectly monochromatic, with the Kα1 and Kα2 rays not separated, to achieve a more intense incident beam.
- Temperature-dependent XRD was employed to determine the thermal expansion coefficient of several single crystals studied in this thesis, allowing for predictions of their thermal expansion behavior.

3.4.1.2. Raman spectroscopy

The most prevalent scattering process observed in this context is Rayleigh scattering, where the scattered photon retains the same energy and wavelength as the incident photon, resulting in no net energy change for the molecule. However, Raman scattering, a less common but highly significant inelastic scattering process, involves an exchange of energy between the incident photon and the molecule. This energy exchange can occur in two distinct ways:

(i).Stokes Raman scattering: In this process, the molecule absorbs energy from the photon, causing an increase in the photon's wavelength (i.e., a decrease in its energy). This type of scattering is more commonly observed because most molecules in a sample are in their ground vibrational state, making it easier for them to gain energy.

(ii). Anti-Stokes Raman scattering: Conversely, in this process, the molecule loses energy to the photon, resulting in a decrease in the photon's wavelength (i.e., an increase in its energy). Anti-Stokes scattering is less common and typically less intense because it requires molecules to be in an excited vibrational state, which is less likely under normal conditions.

Due to the higher probability and intensity of Stokes Raman scattering, it is primarily measured in Raman spectroscopy to gather detailed information about the vibrational states of the molecules in a sample. The relationships and origins of Rayleigh, Stokes, and Anti-Stokes Raman scattering processes are visually depicted in Figure 3.9, providing a clear representation of these fundamental concepts.

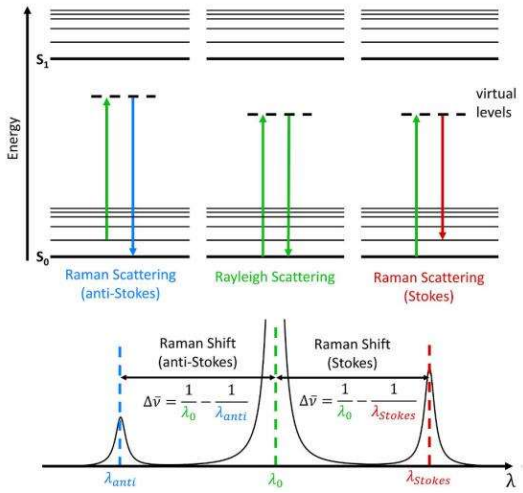

Figure 3.9. Jablonski diagram showing the origin of Rayleigh, Stokes and Anti-Stokes Raman Scattering [155].

In this PhD study, Raman spectra were obtained using a confocal Raman microscope (inVia, Renishaw) with a ×50 objective (Leica) and laser excitation sources (Ar^+ ion laser at 514 nm and He-Ne laser at 633 nm) also located at the SRCiT of the URV. Figure 3.10 displays the schematic and images of the InVia Raman spectrometer. The system includes a light source for excitation, a detector for capturing Raman scattered light, and an optical system for directing the excitation radiation to the sample, collecting the scattered light, and transmitting it to the detector.

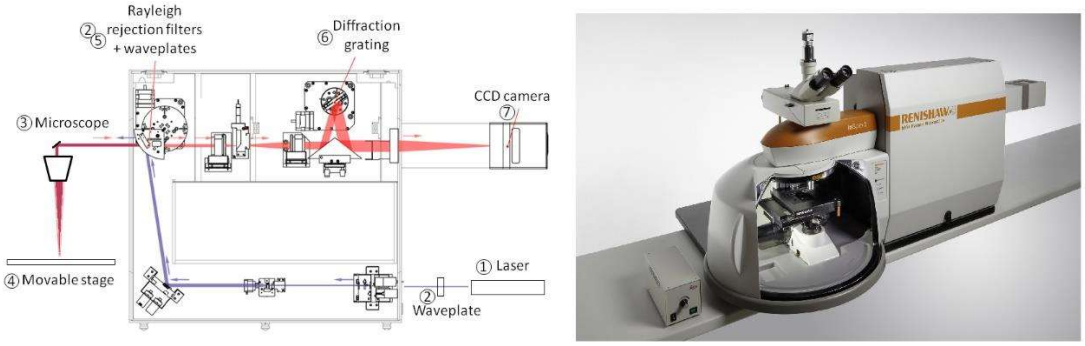

Figure 3.10. (a) Layout of Renishaw inVia confocal Raman spectrometer. The key components are highlighted. Adapted from Renishaw's documentation; (b) Renishaw Raman spectrometer available at the URV facility used for the analysis presented in this thesis.

3.4.2. Scanning electron microscopy

Scanning Electron Microscopy, SEM is a widely used technique for high-resolution surface analysis, offering excellent depth of field images of surface topography. It employs a highly focused scanning electron beam with an energy range of 0.5–30 kV. This beam interacts with the surface, generating low-energy secondary electrons influenced by the surface topography. By measuring these electrons' intensity relative to the scanning beam's position, a detailed surface image is created. The beam also produces backscattered electrons and X-rays, with backscattered electron intensity correlating to the sample's atomic number, providing qualitative elemental information. Figure 3.11 illustrates the basic SEM setup.

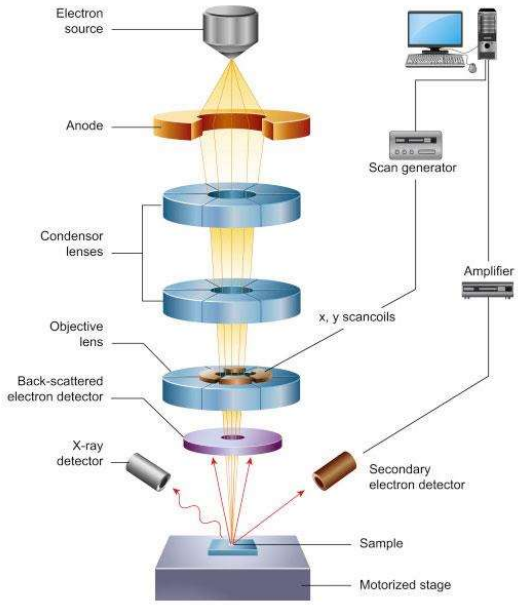

Figure 3.11. Basic SEM set-up and its electron path.

Within this PhD study, the SEM was applied for the morphological and microstructural study of layers from the cleaving $KY(MoO_4)_2$ crystals. These crystals were studied by SEM at the SRCiT using a JCM-7000 NeoScope Benchtop microscope (Jeol) with an integrated Energy Dispersive X-ray (EDX) module, see it in Figure 3.12. The accelerating voltage was 15 kV, the working distance was 13 mm, and the measurements were performed in a high-vacuum mode.

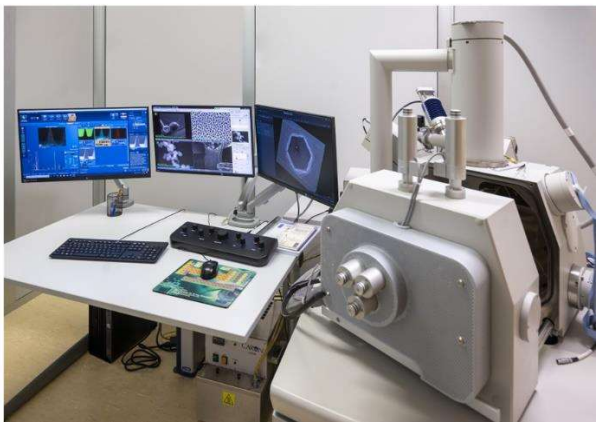

Figure 3.12. Image of the SEM used at SRCiT facility of the URV

3.4.3. Optical characterization

3.4.3.1. Optical Absorption

The capability of a material to absorb light is typically assessed using optical absorption spectroscopy. This analytical technique involves comparing the intensity of a monochromatic light beam passing through a sample with that of an unabsorbed reference beam of the same wavelength. By systematically varying the wavelength to cover the desired spectral range, absorption measurements can be obtained. Absorption spectroscopy has multiple applications, including determining the optimal pump wavelength, calculating absorption cross-sections, and providing insights into the lattice structure by examining the distribution of Stark sublevels within the absorption bands.

The shape, width, and, to some extent, the spectral position of rare-earth absorption bands are influenced by the interaction between the energy levels of the rare-earth ions and the local crystal field in which they are embedded. This interaction significantly affects the material's absorption characteristics.

To evaluate the transparency and absorption of the materials under study, transmission spectra were measured from the UV to the near-IR range using an UV/Vis/NIR spectrometer (Cary 5000). The resolution (spectral bandwidth, SBW) was 0.25 nm in the visible range and 0.7 nm in the near-IR, see it in Figure 3.13.

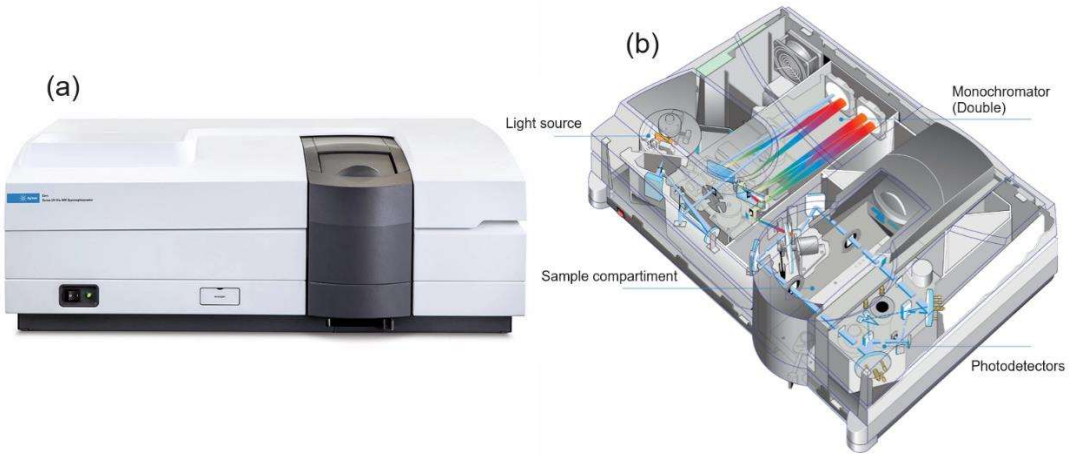

Figure.3.13. Carry 5000 spectrometer available at our lab FiCMA: (a) a photograph of the machine; (b) view of the different optical components inside the machine.

From the obtained transmission spectra, absorption spectra were recalculated using the Beer-Lambert law [156]:

$I(\lambda, d) = I_0(\lambda)e^{-\alpha(\lambda)d}$, Eq.3.1

where I is the transmitted intensity, I_0 is the incident intensity, α and d are the absorption coefficient and the sample thickness, respectively. Thus, the absorption coefficient can be expressed as follows:

$\alpha(\lambda) = \frac{1}{d} ln \frac{I_0(\lambda)}{I(\lambda,d)}$, Eq.3.2

With the doping concentration N_{dopant}, the absorption cross-section can be determined as follows:

$\sigma_{abs}(\lambda) = \frac{\alpha(\lambda)}{N_{dopant}}$, Eq.3.3

3.4.3.2. Luminescence (emission and lifetime measurements)

Atoms excited to high energy levels release energy by transitioning to lower levels. When excited by a high-temperature source, this emission is called atomic or optical emission. If light causes the excitation, it is called atomic fluorescence. Photoluminescence refers to energy released as light during these transitions, while non-radiative decay occurs without light emission.

The photoluminescence spectrum reveals transition energies, helping determine electronic energy levels. The intensity of photoluminescence indicates the rates of radiative and non-

radiative recombination. Photoluminescence identifies electronic transitions and their lifetimes. Under pulsed excitation, transient photoluminescence intensity shows the lifetime of nonequilibrium states, with emission intensity decreasing exponentially over time. The radiative lifetime (τ_{rad}) is the time it takes for emission intensity to fall to 1/e of its initial value, important for understanding electronic level depopulation and excitation dynamics. Analyzing this light provides extensive information about the photo-excited material.
The emissions spectra measured in the range visible-1200 nm were collected using AQ6373E Visible Wavelength Optical Spectrum Analyzer (OSA) from Yokogawa Electric Corporation, see it in Figure 3.14(a). This OSA come with very high wavelength resolution variable from 0.02 up to 10 nm in the range 350-1200 nm. For the emission in the ~2 µm, we used AQ6375E Long Wavelength OSA, from Yokogawa as well−see it in Figure 3.14(b) , come with high resolution up to 0.05 nm and High sensitivity down to -70 dBm in the range 1200-2400 nm.

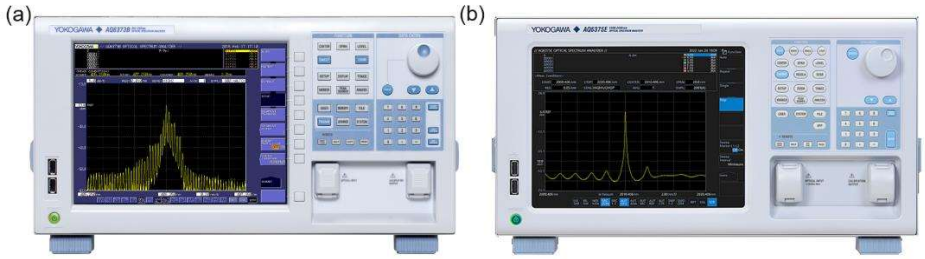

Figure 3.14. (a) AQ6373E visible wavelength OSA; (b) AQ6375E long wavelength OSA.

The luminescence lifetime was studied using a ns optical parametric oscillator (Horizon, Continuum), a 1/4 m monochomator (Oriel 77200), and an 8 GHz digital oscilloscope (DSA70804B from Tektronix). A photomultiplier tube was used for visible wavelengths, while an InGaAs detector was employed for NIR emissions. To prevent the reabsorption of emitted light from affecting the measured lifetimes, the samples were ground into a fine powder before testing.

3.4.3.3. Low-temperature spectroscopy

Low temperature (LT) spectroscopy is an important technique used to study the energy levels and transitions of rare-earth ions in various host materials. This method becomes particularly valuable when investigating the fine details of Stark splitting, which is the splitting of degenerate energy levels in a crystal field. Rare-earth ions, such as those from the lanthanide series, possess unique electronic configurations that result in rich and complex spectra. These ions typically have unfilled 4f orbitals, which are shielded by the outer 5s and 5p orbitals. This shielding effect causes the 4f electrons to be relatively unaffected by the surrounding crystal field, leading to sharp and well-defined spectral lines. However, in the presence of a crystal field, the degeneracy of the energy levels of rare-earth ions is lifted, resulting in Stark splitting. This phenomenon can provide detailed information about the local environment of the ions, including symmetry properties and the strength of the crystal field. Performing spectroscopy at low temperatures is crucial for several reasons:

1. **Reduced thermal broadening**: At higher temperatures, thermal vibrations cause broadening of spectral lines, which can obscure fine details. LT minimize these vibrations, leading to sharper spectral lines and better resolution of Stark components.
2. **Population of lower energy states**: Rare-earth ions have numerous closely spaced energy levels. At LT, only the lower energy states are significantly populated, simplifying the spectra and making it easier to assign and analyze Stark components.

3. **Increased sensitivity**: LT conditions often enhance the intensity of spectral lines, improving the signal-to-noise ratio and making it easier to detect weak transitions.

Cryogenic temperatures for luminescence and absorption were obtained by an Oxford closed-cycle helium CCC1104 cryostat, see the setup in figure.3.15.

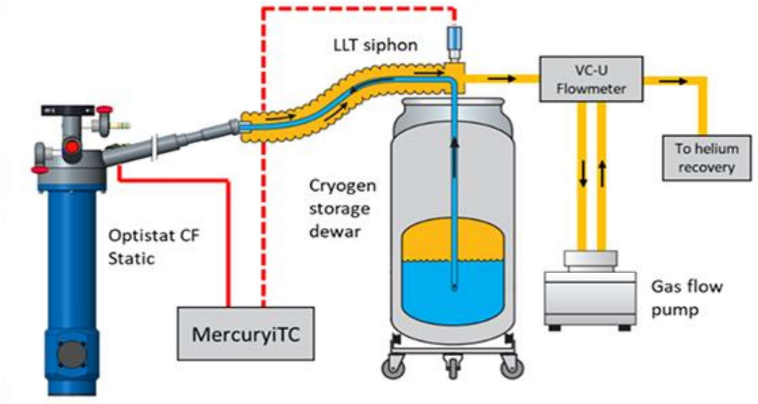

Figure 3.15. Helium cryostat experimental set-up

3.4.3.4. Judd-Ofelt (J-O) calculations

In this PhD work, the transition intensities of the RE^{3+} ions (specifically Tm^{3+} and Ho^{3+}) in different crystal hosts were analyzed using the Judd-Ofelt (J-O) formalism for electric-dipole (ED) contributions. Magnetic-dipole (MD) transitions (for $\Delta J = J - J' = 0, \pm 1$, except for $J = J' = 0$) were calculated separately using the Russell–Saunders approximation on RE^{3+} wave functions, assuming a free-ion model [157]. These calculations require dispersion curves of the laser crystal hosts. For anisotropic crystals, values are polarization averaged. The absorption oscillator strengths were determined from the measured absorption spectra:

$$\langle f_{exp}(JJ')\rangle = \frac{m_e c^2}{\pi e^2 N_{RE^{3+}} \langle\lambda\rangle^2} \langle\Gamma(JJ')\rangle; \text{ Eq.3.4}$$

where m_e and e represent the electron's mass and charge, respectively, c is the speed of light, $<\Gamma(JJ')>$ is the integrated absorption coefficient over the absorption band, and $\langle\lambda\rangle$ denotes the "center of gravity" of the absorption band.

According to the standard J-O theory, the ED line strengths for $J \rightarrow J'$ transitions, $S^{ED}(JJ')$, used for Ho^{3+} and Tm^{3+} ions in this study, are referenced in [158,159]:

$$S^{ED}_{calc}(JJ') = \sum_{k=2,4,6} U^{(k)} \Omega_k; \text{ Eq.3.5}$$

$$U^{(k)} = \langle (4f^n) SLJ || U^k || (4f^n) S'L'J' \rangle^2; \text{ Eq.3.6}$$

Let us consider the potential configuration interaction. If the interaction is only influenced by the lower-energy excited configuration of the opposite parity, the ED line strengths are given by [16]:

$$S^{ED}_{calc}(JJ') = \sum_{k=2,4,6} U^{(k)} \tilde{\Omega}_k; \text{ Eq.3.7}$$
$$\tilde{\Omega}_k = \Omega_k [1 + 2\alpha (E_J + E_{J'} - 2E_f^0)]; \text{ Eq.3.8}$$

In this context, the intensity parameters $\tilde{\Omega}_k$ are linear functions of the energies E_J and $E_{J'}$ of the two multiplets in the $J \rightarrow J'$ transition. E_f^0 is the mean energy of the $4f^n$ configuration, and $\alpha \approx 1/(2\Delta)$ is the average energy difference between the $4f^n$ and $4f^{n-1}5d^1$ configurations.

This approximation is known as the modified Judd-Ofelt (mJ-O) theory. In mJ-O theory, $\tilde{\Omega}_k$ parameters are converted to Ω_k parameters of the standard theory by assuming a high-energy $4f^{n-1}5d^1$ configuration, making the energy difference Δ approach infinity (or α approach zero).

The absorption oscillator strengths relate to the line strengths:

$$f^{\Sigma}_{\text{calc}}(JJ') = \frac{8}{3h(2J+1)\langle\lambda\rangle}\left(\frac{n^2+2}{\sqrt{9n}}\right)^2 S^{\text{ED}}_{\text{calc}}(JJ') + f^{\text{MD}}_{\text{calc}}(JJ'); \text{ Eq.3.9}$$

where h is the Planck constant, n is the refractive index of the crystal at $\langle\lambda\rangle$ and the superscript "Σ" stands for the total (ED+MD) value. In the standard J-O theory, there are three free parameters, (Ω_2, Ω_4, Ω_6), and in the mJ-O theory, there are four free parameters, (Ω_2, Ω_4, Ω_6 and α).

The intensity parameters are significant because they describe the strength of electric dipole transitions, which are typically parity forbidden in the $4f^n$ shell of a free ion. However, a non-centrosymmetric crystal field can mix states of opposite parity, lifting this restriction.
The calculation of these intensity parameters assumes: (i) ground $4f^n$ states are linear combinations of Russell-Saunders coupled states, (ii) ground $4f^n$ and excited $4f^{n-1}5d^1$ configurations are degenerate, with the excited configuration much higher in energy, (iii) all Stark sub-levels of the ground manifold are equally populated, and (iv) the local field approximation holds.
Under these conditions, the line strengths of electric dipole transitions follow a standard equation, and the same set of intensity parameters (Ω_k) applies to all transitions, aligning with weak configuration interaction (WCI) or the standard J-O theory. These parameters include odd-order crystal field terms and radial integrals of wavefunctions. While theoretically computable, they are usually fitted to experimental absorption data [19].

The mJ-O theory accounts for the varying energies of different multiplets in the ground configuration and their energy gaps relative to the excited $4f^{n-1}5d^1$ configuration. Thus, intensity parameters depend on the multiplets' energies and the average energy gap, as shown in Equations 3.7 and 3.8.
The standard J-O theory assumes the energy gap between the ground $4f^n$ configuration, and any excited configuration is much larger than the energies of the involved multiplets, which isn't valid for most trivalent rare-earth ions except Yb^{3+} and Ce^{3+}. This is particularly true for higher-lying $4f^n$ multiplets, requiring configuration interaction consideration for ions like Ho^{3+} and Tm^{3+} studied in this thesis. The discrepancy is especially noticeable in Pr^{3+} ions, where the standard J-O theory fails to explain experimental transition intensities, with further details available elsewhere. The probabilities of radiative spontaneous transitions for emission channels J → J′ are then determined from the corresponding line strengths in emission:

$$A^{\Sigma}_{\text{calc}}(JJ') = \frac{64\ \ ^4e^2}{3h(2J+1)\langle\lambda\rangle^3} n\left(\frac{n^2+2}{3}\right)^2 S^{\text{ED}}_{\text{calc}}(JJ') + A^{\text{MD}}_{\text{calc}}(JJ'); \text{ Eq.3.10}$$

Using the A_{calc} values, the total probabilities of spontaneous radiative transitions from the excited states (A_{tot}), the radiative lifetimes (τ_{rad}), and the luminescence branching ratios ($B(JJ')$) were determined for specific emission channels:

$$\tau_{rad} = \frac{1}{A_{tot}}, \text{ where } A_{tot} = \sum_{J'} A^{\Sigma}_{calc}(JJ'); \text{ Eq.3.11}$$

$$\beta(JJ') = \frac{A^{\Sigma}_{calc}(JJ')}{A_{tot}}$$; Eq.3.12

3.4.4. Laser experiments

3.4.4.1. Laser cavities

The laser experiments with single crystals discussed in this thesis were conducted using four different types of resonators. The first type is the two-mirror laser cavity, which includes two setups: the plane-plane (microchip) laser cavity, illustrated in figure.3.16(a), and the plane-concave (hemispherical) laser resonator, figure.3.16(b): in the microchip setup, the crystal gain medium is wrapped in in foil on all four lateral sides to enhance heat dissipation. It is secured in a copper holder cooled by circulating water. Both end facets of the crystal are polished to laser quality. This laser cavity comprises a flat pump mirror (PM) coated for high transmission (HT) at the pump wavelength and high reflection (HR) at the laser wavelength. The output couplers (OCs) are flat with partial transmission at the laser wavelength. Both cavity mirrors are positioned close to the crystal end faces. The microchip laser cavity offers the potential for miniaturization, power scaling and increased laser efficiency. For the hemispherical resonator, the laser is achieved by using a concave output coupler instead of a flat one with a typically used radius of curvature (RoC) of −25 to −75 mm. This setup provides the ability to tune the laser by utilizing a lyot filter.

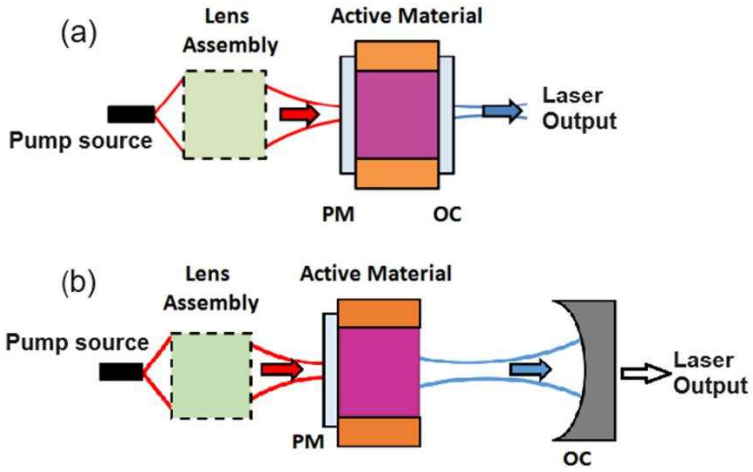

Figure 3.16. Two-mirror laser cavity: (a) the plane-plane (microchip) laser cavity; (b) plane-concave (hemispherical) laser resonator.

For cryogenic laser operations, an L-shaped cavity was used, as shown in figure 3.17. The LT laser experiments have been carried out at the HILASE Center, Institute of Physics the Czeck Republic. This setup includes:

- A concave rear mirror with HR coating at the laser wavelength and a RoC of -300 mm.
- A plane dichroic mirror with HR coating at the laser wavelength and high HT at the pump wavelength.
- AR coated plane-convex lens.
- A series of plane output couplers with partial transmission at the laser wavelength.

The pump beam is collimated and focused into the laser element using two AR-coated achromatic lenses. The crystal is placed in a vacuum chamber between the dichroic mirror and the intracavity lens, wrapped in in foil, and mounted in a copper holder for conduction cooling. To prevent condensation, the chamber is kept at a pressure of 10^{-5} mbar. Cryogenic temperatures

are achieved with a closed-cycle helium cryostat (CH-204, JANIS), providing 13.5 W cooling power at 100 K. A Lake Shore temperature controller (DT 670) with a silicon diode sensor and a 50 Ω heater monitors and maintains the sample temperature.

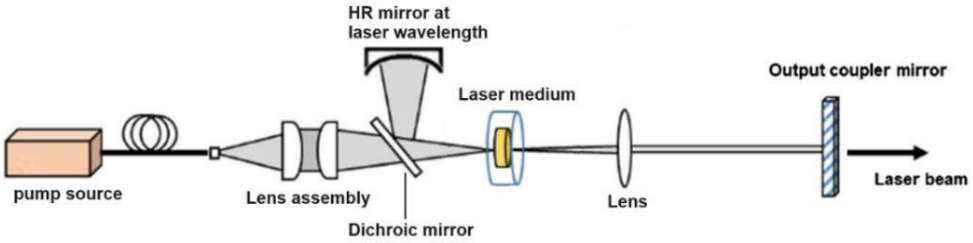

Figure 3.17. Schematic of the experimental setup for studying the cryogenic laser performance.

Another type of cavity was also utilized in this thesis, characterized as a 4-mirror astigmatically compensated X-folded linear cavity. These experiments were carried out at the Max Born Institute for Nonlinear Optics and Short Pulse spectroscopy (MBI) in Berlin, Germany. The configuration of this cavity is illustrated in figure.3.18. In this setup, a coated laser element is positioned at normal incidence between two folding concave mirrors, M1 and M2, with a RoC of 100 mm. When the crystal is uncoated, it can be placed at Brewster's angle to minimize losses and reflections for horizontal polarization pumping. A focusing pump beam is directed into the laser crystal through the folding mirror M1 with the aid of a focusing lens. For the CW operation, a flat, highly reflective mirror M3 is employed, along with a set of flat OCs, which can be either planar or plane-wedged, featuring partial transmission at the laser wavelength. Additionally, for the purpose of wavelength tuning experiments, a Lyot filter was incorporated near the output coupler. This filter allows precise control over the laser wavelength by adjusting the optical path length within the cavity. This setup is designed to ensure optimal performance and adaptability for a wide range of experimental conditions. For instance, it is highly suitable for use in mode-locked lasers, which can be achieved by incorporating additional components such as saturable absorbers and dispersion control optics into the cavity.

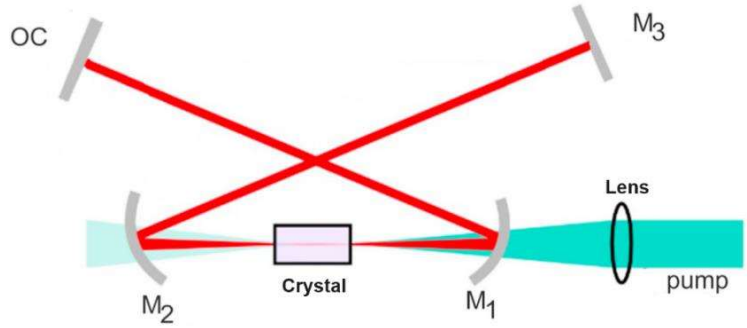

Figure 3.18. Astigmatically compensated X-folded linear cavity.

3.4.4.2. Pump sources

The pump sources utilized in the experiments can be categorized based on the type of active ion present in the laser gain medium:

Pump Sources for Yb^{3+} Ions:

- Yb:LuYAG Crystal: A continuous-wave Ti:sapphire laser (model 3900S, Spectra Physics), precisely tuned to 941.0 nm, operating in the fundamental transverse mode with a beam quality factor (M^2) close to 1, was employed to pump the Yb:LuYAG crystal for tunable CW operation. For power scaling experiments involving this crystal, a fiber-coupled InGaAs laser diode (LD) with a core diameter of 105

μm and a numerical aperture (N.A.) of 0.22 was used. The LD was stabilized using a VBG, which ensured an emission with a Full Width at Half Maximum (FWHM) of approximately 0.1 nm, centered precisely at 969.2 ± 0.1 nm. To maintain stability in the emission wavelength, the LD was temperature-controlled using a cooling chiller. This same LD was also employed during the cryogenic operation of the Yb:LuYAG crystal in laser mode.

-Yb:KYMo Crystal: A fiber-coupled InGaAs LD was used as the pump source, emitting unpolarized output at a central wavelength of approximately 968 nm. The LD had a fiber core diameter of 105 μm and N.A. of 0.22, making it suitable for efficiently pumping the Yb:KYMo crystal.

-Yb:GdCB Crystal: The pump source for the Yb:GdCB crystal was a multi-transverse mode, fiber-coupled InGaAs laser diode capable of emitting up to 50 W of unpolarized radiation at 976 nm. The fiber used had a core diameter of 105 μm and N.A. of 0.15. To ensure consistent performance over the entire operating range, the emission wavelength of the laser diode was stabilized by a VBG element with a linewidth of approximately 0.7 nm.

-Yb:YGG Crystal (Cryogenic CW Laser Operation): For the cryogenic CW laser operation of the Yb:YGG crystal, a 60 W laser diode (BWT Beijing LTD) was utilized. This diode was wavelength-locked at 968.8 nm with a narrow spectral bandwidth of 0.40 nm, thanks to an integrated VBG element. The laser light was coupled to a fiber with a core diameter of 105 μm and N.A. of 0.22, ensuring efficient pump delivery.

Pump Sources for Nd^{3+} Ions:

-Nd:CsGdMo Crystal: For the crystal doped with Nd^{3+} ions (Nd:CsGdMo), a continuous-wave Ti:sapphire laser (model 3900S, Spectra Physics) was used as the pump source. This laser delivered up to 3 W at a wavelength of 808.8 nm in the fundamental mode ($M^2 \approx 1$). The pump beam was polarized, and a half-wave plate was employed to adjust the polarization to align with the crystal's maximum absorption, ensuring optimal pump efficiency.

Pump Sources for Tm^{3+} Ions:

-Tm:KYMo Crystal: The Tm:KYMo crystal used in the CW laser operation was pumped by a fiber-coupled AlGaAs laser diode, emitting up to 17 W of unpolarized output at 802 nm. The LD featured a fiber core diameter of 200 μm and N.A. of 0.22, with an M^2 of 86.

-Tm:CLTGG Crystal: The pump source for the Tm:CLTGG crystal consisted of a fiber-coupled AlGaAs LD with a core diameter of 200 μm and N.A. of 0.22. This diode emitted unpolarized output at a central wavelength of 793 nm with an emission bandwidth of 5 nm, and an M^2 greater than 80.

-Tm:YLF Crystal (Cryogenic CW Laser Operation): For the cryogenic CW laser operation of the Tm:YLF crystal, a LD emitting at 793 nm (BWT Beijing LTD) was employed as the pump source. The diode's emission bandwidth was stabilized to 0.5 nm by a VBG element. The fiber-coupled diode had a core diameter of 105 μm and N.A. of 0.22, delivering a maximum output power of 25 W.

Pump Sources for Tm^{3+}/Ho^{3+} Codoped Systems:

-Tm,Ho:CNGG Crystal: For this crystal, the applied pump source was a narrow-band continuous-wave Ti:sapphire laser with a maximum output power of 3.6 W at 785.6 nm. The laser operated in the fundamental mode ($M^2 \approx 1$), ensuring a highly efficient and stable pump for the codoped crystal system.

3.4.4.3. Equipments used for laser characterization

The characterization of laser emission spectra at 1 μm was carried out using a compact spectrometer from Ocean Optics, specifically the USB 2000+ model, which offers a high spectral resolution of 0.3 nm. This device was essential for capturing detailed emission spectra during the experiments. Additionally, in certain experimental setups, an optical spectrum analyzer (OSA) device, the Ando

AQ6315-E, was employed to provide further spectral analysis and to ensure accurate measurement of the laser's optical output.

For the analysis of passively Q-switched pulses, an ultrafast silicon photodiode (model UPD-500-UP, manufactured by Alphalas) was utilized. This photodiode is notable for its 6 GHz bandwidth and an impressive rise time of less than 500 picoseconds, making it highly suitable for detecting rapid pulses with high precision. The pulses detected by the photodiode were then recorded and analyzed using a digital oscilloscope. The oscilloscope used for this purpose was the Teledyne LeCroy Wavesurfer, which features a bandwidth of 600 MHz and a sampling rate of 10 GS/s, enabling the accurate capture and detailed examination of the pulse characteristics.

When analyzing the spectral output of the laser at 2 μm, a different spectrometer, the WaveScan from APE, was employed to provide the necessary spectral resolution for this wavelength. Additionally, to study the far-field mode profile of the laser, a FIND-R-SCOPE near-infrared camera (model 85726) was used. This specialized camera allowed for the precise capture of the mode profile, which is crucial for understanding the spatial distribution of the laser beam in the far-field region.

CHAPTER 4

CHAPTER 4: Results

In this chapter, the results of our research on spectroscopy and continuous wave (CW) laser operation of various crystals are briefly presented. The lasers lie in the 1 µm and 2 µm spectral ranges. An overview of the laser emission characteristics is provided, including laser wavelength, slope efficiency, and laser tunability.

For a comprehensive understanding, detailed information on the crystal growth processes, the structural properties of the studied crystals, and in-depth spectroscopic analyses are available. Additionally, descriptions of the experimental setups used for laser operation, including the specific pump configurations and cavity geometries, as well as some specific conditions under which the lasers were tested (e.g. cryogenic temperature), can be found in the associated papers dedicated to each crystal, attached to this doctoral thesis. These papers delve into the methodologies and findings, offering valuable insights into the crystals 'properties and their implications for near infrared laser performance.

4.1. Spectroscopy and laser generation results of ions emitting at ~1 µm in crystals doped with Yb and Nd

4.1.1. The "Mixed" Yb:(Y, Lu)$_3$Al$_5$O$_{12}$ Garnet Crystal

A single crystal of ytterbium-doped mixed yttrium–lutetium aluminum garnet ($Y_{0.601}Lu_{0.233}Yb_{0.166})_3Al_5O_{12}$ (denoted as Yb:(Y,Lu)AG) was grown using the CZ method (Figure 4.1(a)) and studied for its spectroscopy and laser operation as shown in PAPER I. It has a cubic structure (space group $Ia\bar{3}d$, lattice parameter a = 11.9790(0) Å) similar to YAG ($Y_3Al_5O_{12}$) [160]. The crystal shows favorable properties for Yb^{3+} ion doping, with a broad absorption band around 940 nm well-aligned with the emissions of InGaAs laser diodes (see Figure 4.1(b)), a high σ_{SE} of 2.53 × 10^{-20} cm² at 1031 nm, and a luminescence lifetime of 1.063 ms. Gain profiles shift from 1048 nm to 1030 nm as the inversion ratio β increases Figure .4.1(c)), with a gain bandwidth of 7 nm at β = 0.10.

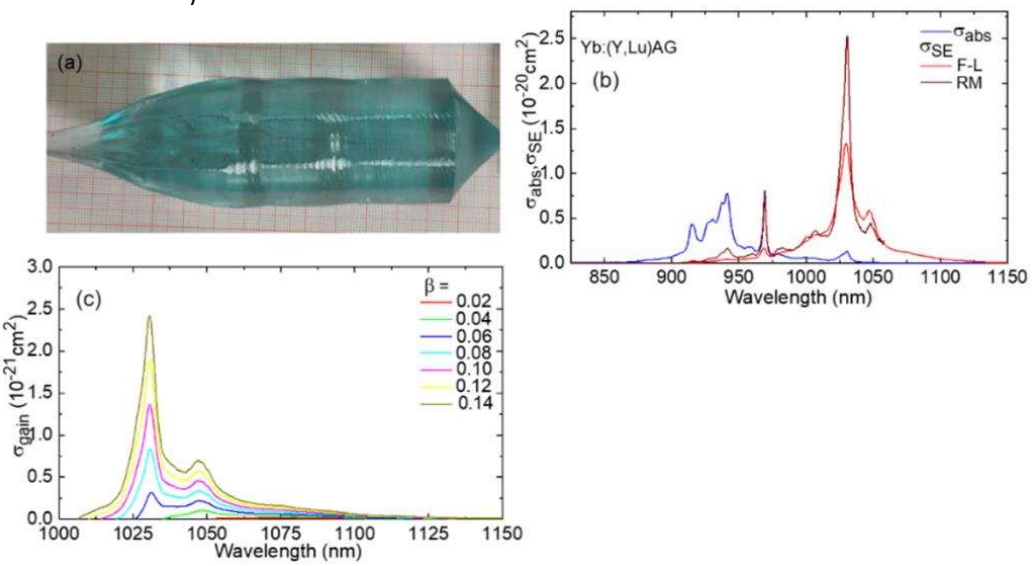

Figure 4.1.(a) A photograph of an as-grown Yb:(Y,Lu)AG crystal; (b) Transition cross-sections of Yb^{3+} ions (the $^2F_{7/2}\rightarrow{}^2F_{5/2}$ transition) in the Yb:(Y,Lu)AG crystal: absorption (σ_{abs}) and stimulated-emission (σ_{SE}) cross-sections calculated by F-L; Füchtbauer–Ladenburg equation and RM: reciprocity method; (c) gain cross-sections, $\sigma_{gain} = \sigma_{SE}–(1–\beta)\sigma_{abs}$, $\beta = N(^2F_{5/2})/N_{Yb}$

Efficient laser operation using a crystal doped with 16.6 at.% Yb^{3+} was successfully demonstrated under pumping utilizing a Ti: Sapphire laser. This setup, as illustrated in figure 4.2(a-b), was implemented within a hemispherical laser cavity, which led to an output power of

1.04 W within the 1.03 to 1.05 µm wavelength range. The system achieved a remarkable slope efficiency of 76.4%, coupled with a very low laser threshold of just 76 mW. Beyond these results, continuous wavelength tuning was also accomplished, covering a range of 51.6 nm between 1026.4 and 1078.0 nm. Further experiments explored diode-pumping in combination with microchip geometry, as depicted in figure 4.2(c-d). This approach enabled power scaling, resulting in a maximum output power of approximately 9 W around the 1.05 µm wavelength, maintaining a high slope efficiency of 76%. These findings indicate that this "mixed" crystal exhibits significant potential for the development of diode-pumped, power-scalable lasers operating near the 1 µm wavelength region, making it a promising candidate for future laser applications requiring high efficiency and scalability.

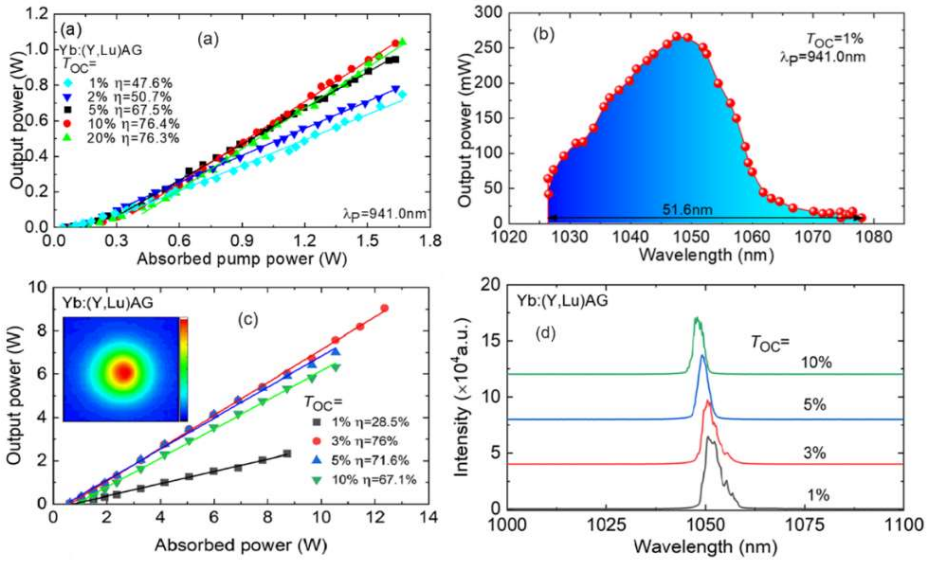

Figure 4.2.(a-b) Free-running Yb:(Y,Lu)AG laser pumped by Ti:Sipphire laser at 940 nm: (a) input-output dependences, (b) wavelength tuning curve of the Yb:(Y,Lu)AG laser; T_{OC} = 1%; (c-d) CW Yb:(Y,Lu)AG microchip laser: (c) input-output dependences, η −slope efficiency; inset: 2D spatial intensity profile of the laser output from a CW Yb:(Y, Lu)AG laser measured at P_{abs} = 11.44 W; (d) typical laser emission spectra measured at P_{abs} = 5.98 W.

4.1.2. Cleaving Yb:$KY(MoO_4)_2$ crystal

In PAPER II, a detailed study was conducted on another Yb-doped laser crystal, specifically KYMo with a doping concentration of 3 atomic percent of Yb^{3+} ions. This crystal was grown using the LTG-Cz method, resulting in transparent and colorless cylindrical crystals that exhibit an elliptical cross-section when viewed along the [010] and [001] crystallographic directions, as illustrated in figure 4.3(a). The crystals possess an orthorhombic crystal structure, belonging to the space group *Pbna*, which was precisely refined using the Rietveld method to confirm its structural characteristics. One of the notable properties of this crystal is its strong optical anisotropy, which refers to the directional dependence of its optical properties. Additionally, the crystal demonstrates perfect cleavage along the (100) plane, meaning that it can easily split along this plane, as depicted in figure 4.3(c). This cleavage characteristic is critical for applications requiring high-quality, flat surfaces.

The absorption properties of the crystal around the 1 µm wavelength are primarily attributed to the electronic transition between the $^2F_{7/2}$ and $^2F_{5/2}$ energy levels of the Yb^{3+} ions. Specifically, the σ_{abs} reaches a maximum of 1.77×10^{-20} cm² at a wavelength of 977.1 nm, which corresponds to the ZPL. The FWHM of this absorption peak is 19.6 nm when the light polarization is parallel to the b-axis (E||**b**). Furthermore, the σ_{SE} is measured at 3.70×10^{-20} cm² at a wavelength of

1008.0 nm, with a corresponding emission bandwidth of 37 nm for the same polarization, as shown in figure 4.3(b).
As detailed in PAPER II, the gain spectra of the crystal for light polarization E||**b** exhibit interesting behavior across different inversion ratios (β). For low inversion ratios (β < 0.03), the gain spectra are relatively flat and broad, covering a range from 1040 nm to 1100 nm. However, as the inversion ratio increases to intermediate values (0.05 < β < 0.10), a distinct peak emerges around 1039 nm. At even higher inversion ratios, a new peak appears near 1019 nm. Notably, at an inversion ratio of β = 0.15, the gain bandwidth narrows to 33.0 nm, indicating a concentration of gain within a specific wavelength range, as illustrated in figure 4.3(d). This behavior is significant for laser applications, as it influences the tunability and getting short pulses in mode locked regime.

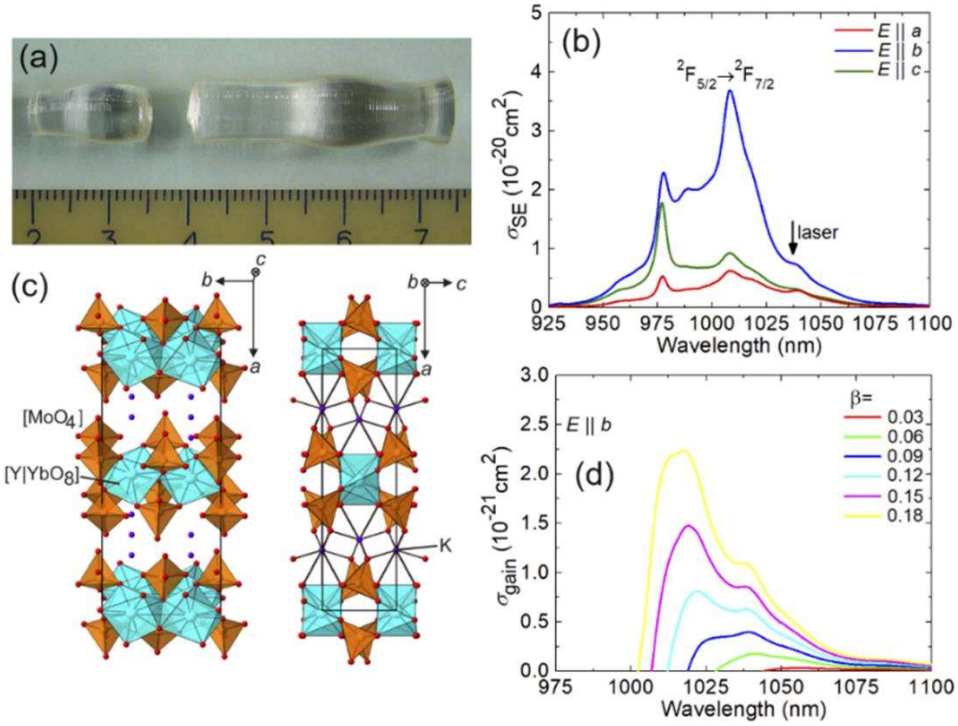

Figure 4.3. (a) A photograph of as-grown 3 at.% Yb:$KY(MoO_4)_2$ crystal. The growth direction is along the [100] direction; (b) σ_{SE}, for light polarizations E||**a**, **b** and **c**. The arrow indicates the observed laser wavelength, (c) three-dimensional view, a projection of the a-c plane and a-b plane ; (d) σ_{gain} spectra for light polarizations E||**b** .

A CW laser operation was successfully demonstrated using a thin crystal plate of Yb: $KY(MoO_4)_2$, which had a thickness of just 286 µm. This operation was achieved by pumping the crystal with a LD emitting at a wavelength of 968 nm, as illustrated in figure 4.4. The setup produced a maximum output power of 0.81 watts within the wavelength range of 1021 to 1044 nm. The laser exhibited a high slope efficiency of 76.4%. The Yb: KYMo crystals used in this setup show great potential for use in advanced laser systems, particularly in sub-nanosecond passively Q-switched microchip lasers. Furthermore, the thinness of the crystal makes it suitable for integration into thin-disk lasers configurations, a design that allows for efficient heat dissipation and high-power operation.

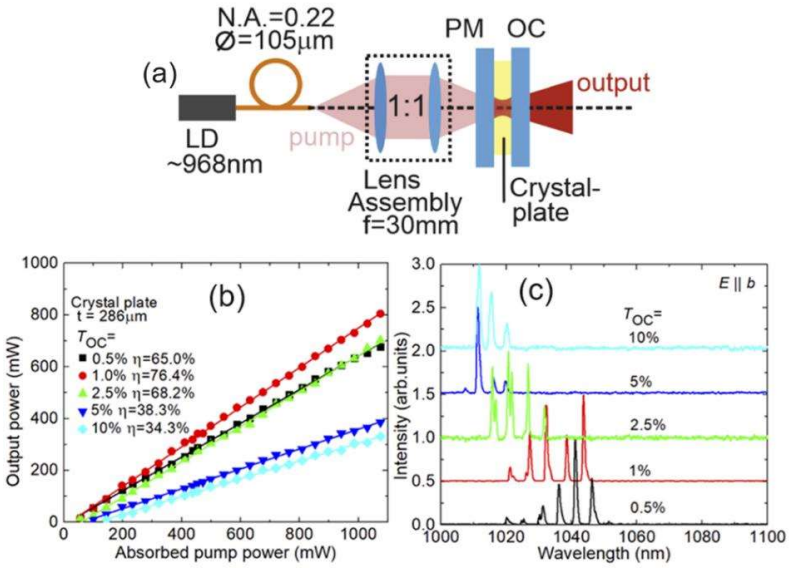

Figure 4.4. Diode-pumped Yb:$KY(MoO_4)_2$ cleaved crystal-plate microchip laser: (a) laser setup; (b) input output dependences; (c) typical laser emission spectra measured at P_{abs} = 1.0 W. The laser polarization is E|| **b**.

4.1.3. The disordered Yb:$Ca_3Gd_2(BO_3)_4$ crystal, Yb:GdCB

Yb^{3+} doped $Ca_3Gd_2(BO_3)_4$ (Yb: GdCB) emerges as a highly promising laser material, particularly noted for its broadband emission centered around 1 µm, as thoroughly discussed in PAPER III. This crystal was grown using the conventional Czochralski (CZ) method in an Ar atmosphere, a process that ensures high purity and quality in the resulting crystal. Upon inspection using a He-Ne laser, the crystal demonstrated exceptional optical clarity with no detectable defects, as illustrated in figure 4.5(a). The structural properties and chemical purity of the crystal were further validated through PXRD analysis, depicted in figure 4.5(b).

As an optically biaxial crystal, Yb: GdCB's spectral properties were meticulously analyzed across its three principal polarizations, aligned with the crystal axes a, b, and c. The absorption cross-section spectra corresponding to these polarizations are presented in figures 4.5(c), (d), and (e). The crystal's unique structure features multiple cationic sites labeled M1, M2, and M3. These sites exhibit distorted coordination geometries, with M1 showing VIII-fold and M2 and M3 displaying VII-fold coordination. These sites are randomly occupied by Ca^{2+}, Gd^{3+}, and Yb^{3+} cations, leading to significant inhomogeneous broadening of the Yb^{3+} ion absorption and emission bands. This broadening imparts a "glassy-like" spectroscopic behavior to the crystal, which is further distinguished by its pronounced polarization anisotropy in the stimulated-emission cross-section spectra. This anisotropy results in the linear polarization of the emitted laser light, with the polarization direction depending on the crystal's orientation, specifically E||**b** or E||**c**.

Furthermore, Yb: GdCB exhibits substantial Stark splitting of its ground state ($^2F_{7/2}$), measuring around 735 cm^{-1}. This large splitting, combined with a notably long fluorescence lifetime of 644 microseconds (as shown in figure 4.5(f)), makes this crystal particularly suitable for low-threshold laser operations. The Yb^{3+} ZPL in this crystal displays a broad absorption linewidth of approximately 7.3 to 7.5 nm at 976 nm, a feature that mitigates issues related to bandwidth and temperature drift commonly encountered in InGaAs LD used as pump source for Yb^{3+} ions. The σ_{SE} of Yb^{3+} in Yb: GdCB is calculated to be 0.42×10^{-20} cm^2 at a wavelength of 1025.1 nm, with light polarization aligned along the c-axis (E||**c**). This combination of properties underscores Yb: GdCB's potential as an efficient laser material.

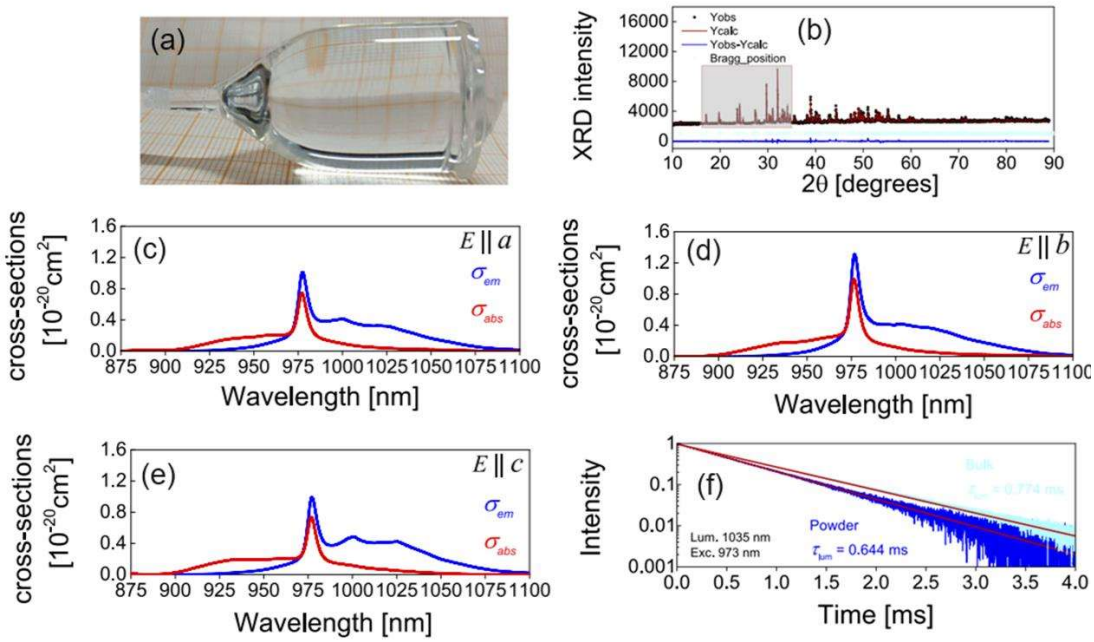

Figure.4.5. (a) Photograph of an as-grown 5 at. % Yb: GdCB crystal; (b) Rietveld refinement plots; (c-d-e) Polarized RT σ_{abs} and σ_{SE} spectra of Yb^{3+} in the Yb:GdCB crystal; (f) RT luminescence decay curve (bulk and powdered samples).

The CW laser performance of the Yb-doped GdCB crystal was thoroughly evaluated using high-power diode pumping at a wavelength of 976 nm. This evaluation specifically focused on three different orientations of the crystal, each aligned along one of the primary crystallographic axes. The detailed results of this assessment are visually represented in Figure 4.6 and are concisely summarized in Table 4.1 for quick reference.

One key finding from this study was observed with an a-cut crystal, which yielded a maximum output power of 5.58 watts at approximately 1057 nanometers. This output was achieved with a slope efficiency of 51.7%, under the condition of linear laser polarization E||**c**.

The performance of the Yb-doped GdCB crystal in this context demonstrated not only its capacity for power scaling but also its broad emission characteristics. These characteristics are particularly noteworthy as they suggest the crystal's potential for generating ultrashort laser pulses, with durations of less than 50 femtoseconds.

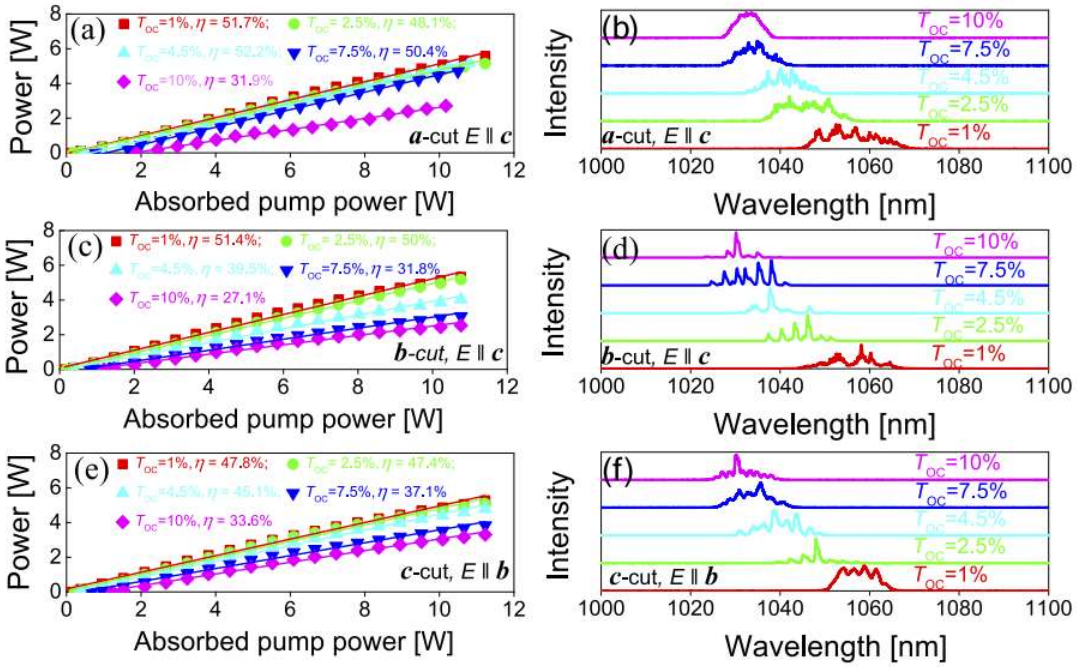

Figure.4.6. CW diode-pumped Yb:GdCB lasers: (a), (c) and (e) input – output dependences; (b), (d) and (f) typical spectra of laser emission. Crystal orientation and laser polarization: (a) and (b) a-cut, E||**c**; (c) and (d) b-cut, E||**c**; (e) and (f) c-cut, E||**b**.

Table 4.1. CW Diode-Pumped Laser Performance of 5 at.% Yb:GdCB Crystals with Different Orientations

Cut	Polarization	P_{out}, W	λ_L, nm	P_{th}, W	η_{opt}, %
a-cut	E ∥ ***c***	5.58	1045–1057	0.137	49.7
b-cut	E ∥ ***c***	5.33	1030–1058	0.137	49.8
c-cut	E ∥ ***b***	5.27	1030–1057	0.069	46.9

4.1.4. Yb:YGG cryogenic laser

In this thesis, we also explored the performance of ytterbium (Yb) lasers operating at a wavelength of 1 µm under cryogenic cooling conditions as well. Specifically, we investigated lasers utilizing a Yb-doped gallium garnet crystal, known as Yb:$Y_3Ga_5O_{12}$, or Yb:YGG for short. The findings from these experiments are comprehensively detailed in PAPER IV.

During the study, we conducted a thorough examination of the optical spectroscopy and continuous wave (CW) laser performance of the Yb:YGG crystal across a range of cryogenic temperatures. Notably, at a temperature of 120 K, the crystal demonstrated a maximum σ_{abs} of 1.7×10^{-20} cm², with a bandwidth of 2.4 nm centered at 970.5 nm, as discussed in PAPER IV. Additionally, the crystal exhibited a maximum σ_{SE} of 6.5×10^{-20} cm², accompanied by a 4.6 nm bandwidth centered at 1024 nm, as illustrated in Figure 4.7(a).

For the CW laser operation, we employed an L shaped laser cavity pumped by VBG-stabilized LD at 969 nm. At a temperature of 120 K, the laser output power was five times greater than that achieved at 200 K. At this optimal temperature, we recorded a slope efficiency of 87% and an optical-to-optical efficiency of 73%, as shown in Figure 4.7(b). Furthermore, the data presented in Figure 4.7(c) indicate that lower temperatures lead to increased slope efficiency while simultaneously reducing the laser threshold. Moreover, at the maximum output power, the laser beam maintained an excellent far-field Gaussian profile, as depicted in Figure 4.7(d).

This beam quality is essential for various precision applications, further highlighting the significance of operating Yb:YGG lasers under cryogenic conditions for enhanced performance.

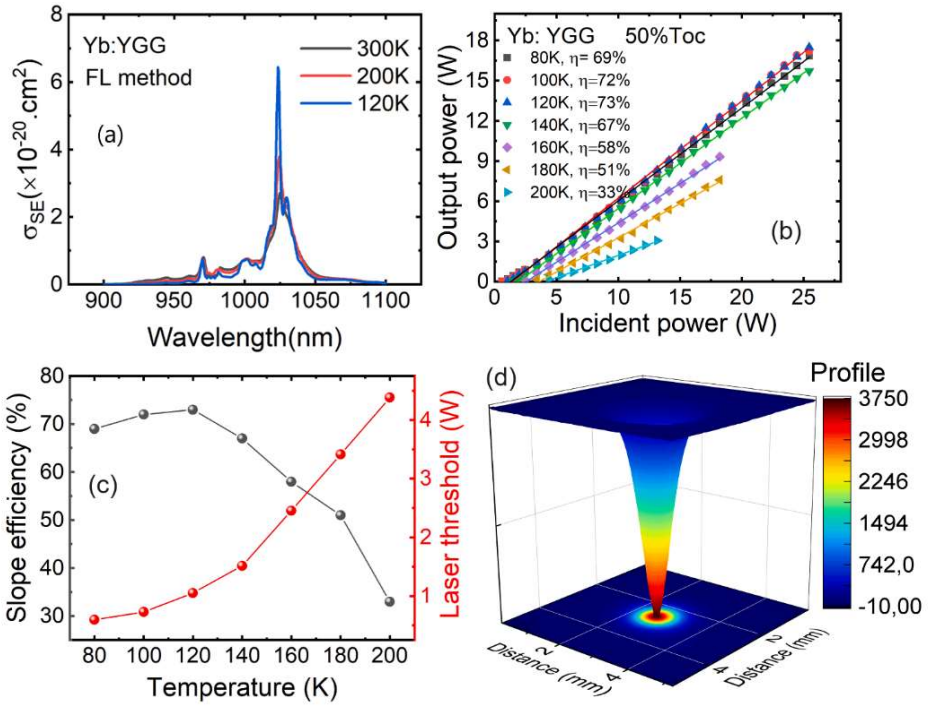

Figure.4.7. Yb: YGG cryogenic laser characteristic: (a) emission cross-sections at different temperatures; (b) Output power vs. incident power characteristics of the cryogenic Yb: YGG laser for various crystal temperatures; (c) Variation of slope efficiency at different temperatures; (d) Measured beam profile at maximum pump power using 50%T_{OC} at 120 K.

4.1.5. Cryogenic laser operation of a "mixed" Yb:(Y,Lu)AG garnet crystal

The final Yb-doped crystal explored in this PhD thesis is the Yb-doped "mixed" yttrium-lutetium aluminum garnet crystal (Yb:LuYAG). This material has demonstrated significant potential for the development of high-power lasers, making it a promising candidate for further research in this area. Although its performance at room temperature had been previously established in PAPER I, our research extended this investigation to include operations at cryogenic temperatures. We explored the laser's behavior in both CW and Q-switched regimes by utilizing an innovative laser cavity design, which is thoroughly detailed in PAPER V.

To better understand the laser's performance, we conducted a series of experiments on the CW cryogenic diode-pumped Yb:LuYAG laser, focusing on its input-output characteristics. We maintained a constant output coupler transmission (T_{OC} = 30%) and systematically varied the crystal temperature from 100 K to 200 K in 20 K increments, as illustrated in Figure 4.8(a). Through these experiments, we identified the optimal performance at a crystal temperature of 140 K, where the laser produced a maximum output power of 8.88 W at a wavelength of 1028.9 nm. At this temperature, the laser achieved a slope efficiency of 51% relative to the incident pump power and exhibited a laser threshold of 0.98 W.

We employed a volume Bragg grating (VBG)-stabilized laser diode pumping at 969 nm, which allowed us to achieve an even higher maximum output power of 10.65 W at 1029 nm with 50% T_{OC} (see it detailed in PAPER V). This was accomplished with a slope efficiency of 56% relative to the incident pump power, again at the optimal crystal temperature of 140 K. Notably, the optimal operating temperature and the laser output characteristics of the "mixed" Yb:LuYAG

crystal were comparable to those observed in Yb-doped LuAG crystals. However, Yb:LuYAG offers the distinct advantage of a simpler and more cost-effective growth process, making it an attractive alternative for large-scale production. Figure 4.8(b) presents a typical far-field beam profile at the maximum output power, revealing a perfectly circular beam with a Gaussian intensity distribution. This profile is indicative of excellent beam quality and confirms effective thermal management through cryogenic cooling, which is crucial for maintaining stable laser operation at high powers.

For the passively Q-switched cryogenic laser, we utilized a commercial high-quality Cr^{4+}:YAG-based saturable absorber (SA). In this configuration, the best pulse characteristics we achieved included an energy output of 0.15 mJ and a pulse duration of 201 ns, operating at a repetition rate of 39.7 kHz. The laser emitted light at a wavelength centered around 1028.9 nm, as illustrated in Figures 4.8(c) and 4.8(d). The detailed characteristics of the saturable absorber and its integration into the laser system are discussed in PAPER V.

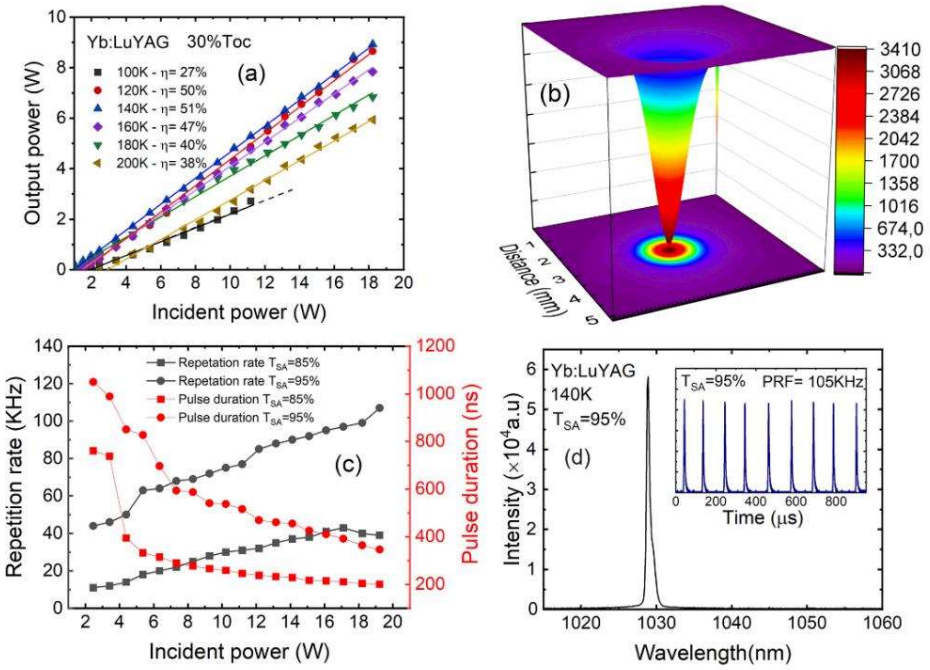

Figure 4.8. (a-b) CW diode-pumped cryogenic Yb:LuYAG laser: (a) input–output dependences for various crystal temperatures at a fixed T_{OC} of 30%; (b) a typical far-field beam profile captured at the maximum output power; (c-d) Passively Q-switched diode-pumped cryogenic Yb:LuYAG laser: (c) repetition rate and pulse duration ; (d) a typical laser spectrum, inset shows an oscilloscope trace of the corresponding pulse train, T_{SA}= 95%.

4.1.6. Monoclinic Nd: $CsGd(MoO_4)_2$ crystal with a layered structure

Other lasers that emit at wavelengths around 1 μm are typically based on neodymium (Nd^{3+}) ions. In the study discussed here, the crystal $CsGd(MoO_4)_2$, referred to as CsGdMo, was utilized as the host material for the Nd^{3+} ions. Detailed information about the crystal's structure, spectroscopic characteristics, and laser performance is thoroughly covered in PAPER VI.

For this research, a 3 at.% Nd:CsGdMo crystal was successfully grown using a flux method under LTG conditions, employing a modified version of the LTG-Cz technique. A seed crystal with a [001] orientation was used to initiate the growth process. The outcome was a crystal that was not only clear and transparent but also free from any cracks, as

demonstrated in Figure 4.9(a). This crystal belongs to the monoclinic crystal system, specifically the *P2/c* space group, with lattice parameters measured as a = 9.5239(4) Å, b = 5.0752(5) Å, c = 8.0580(7) Å, and an angle β = 91.157(9)°. Notably, the Nd:CsGdMo crystal exhibits perfect cleavage along the (100) plane, which is illustrated in Figure 4.9(b).

The study further explored the optical properties of the Nd^{3+} ions within the crystal by measuring polarized optical absorption and luminescence spectra, as shown in Figures 4.9(c-d). The maximum σ_{SE} for light polarization parallel to the b-axis (E||**b**) was found to be 29.0 × 10^{-20} cm² at a wavelength of 1065.9 nm, with a corresponding luminescence lifetime of 145 microseconds. Additionally, transition probabilities for the Nd^{3+} ions were calculated using a modified Judd-Ofelt (J-O) model, resulting in intensity parameters Ω_2 = 26.736, Ω_4 = 12.736, Ω_6 = 17.771 [10^{-20} cm²], and a radiative lifetime parameter α = 0.122 [10^{-4} cm], as further elaborated in PAPER VI. These findings provide valuable insights into the laser performance and potential applications of Nd:CsGdMo crystals.

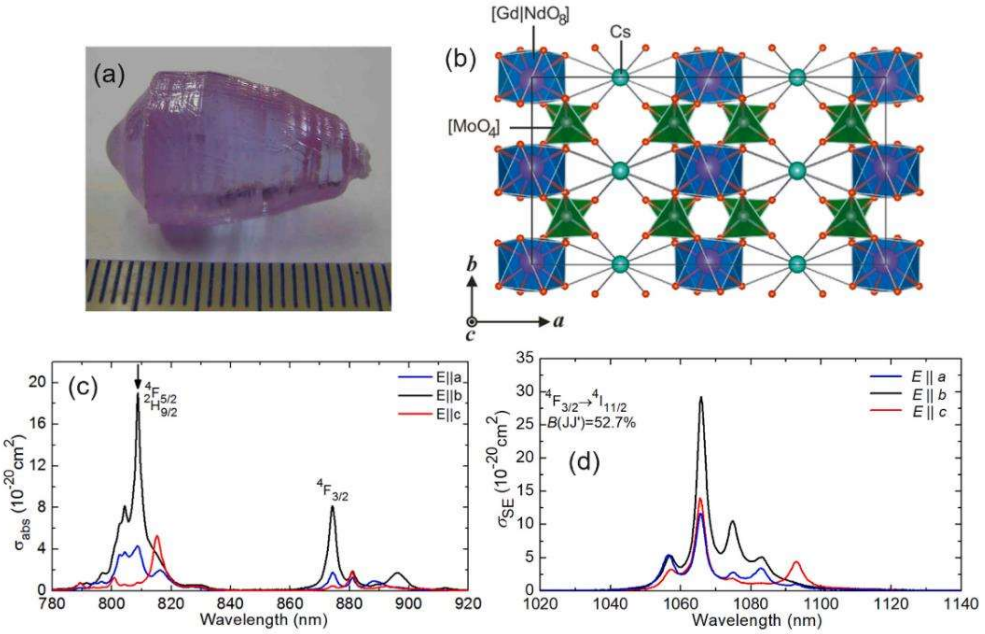

Figure.4.9.(a) Photographs of the as-grown 3 at.% Nd:CsGdMo, the growth direction is along the [001] axis; (b) Crystal structure: a view showing a supercell (2a×2b×2c) in projection to a-b plane; (c) σ_{abs} spectra for the $^4I_{9/2} \rightarrow {}^4F_{5/2} + {}^2H_{9/2}$ and $^4F_{3/2}$ transitions of Nd^{3+} for E||**a**, **b**, **c**; (d) σ_{SE} spectra of the $^4F_{3/2} \rightarrow {}^4I_{11/2}$ transition.

In PAPER VI, the first CW laser operation of mechanically cleaved crystal plate based on Nd:CsGdMo is demonstrated in a compact microchip-type laser cavity, the results are shown in Figure.4.10. The laser yielded a maximum output power of 0.54 W at 1066 nm, with a threshold of 70 mW, a slope efficiency (η) of 60.4%, and a linearly polarized output (E||**b**).

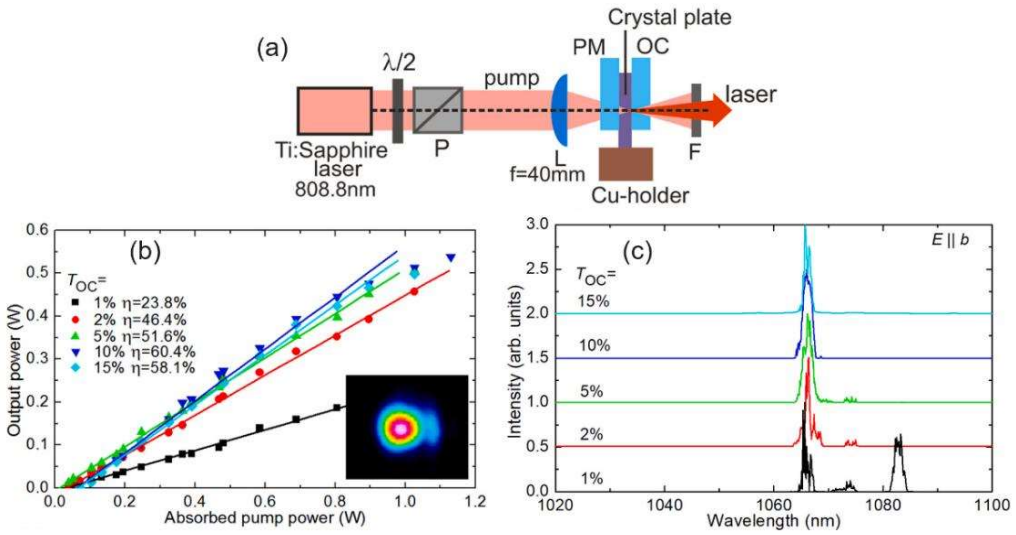

Figure 4.10. Nd:CsGdMo microchip laser: (a) Scheme of the Nd:CsGdMo microchip laser; (b) a) input-output dependences, η – slope efficiency, inset – far-field beam profile (T_{OC} = 10%, Pabs = 0.6 W); (c) typical laser emission spectra, P_{abs} = 0.9 W. The laser polarization is E||b. λ_P = 808.8 nm.

4.2. Spectroscopy and laser outcomes for ions emitting at ~2 µm in crystals doped and co-doped with Ho and Tm.

4.2.1. Cleaved single-crystal plates and films of Tm:$KY(MoO_4)_2$

Solid state lasers emitting at ~2 µm wavelength are for various applications. Two of the most effective ions for producing lasers in this wavelength range are Tm^{3+} and Ho^{3+}. Both ions offering unique advantages in efficiency and performance. Such lasers were investigated in this thesis by using different kind of laser crystal hosts. The cleaved Tm doped Potassium Yttrium double molybdate crystal (Tm:$KY(MoO_4)_2$, shortly Tm:KYMo) was one of the studied laser hosts. The results on the crystal structure, spectroscopy and laser performance on the latter crystal are presented in detail in PAPER VII.

The crystal growth process for Thulium-doped KYMo (Tm:KYMo) was carried out using the LTG-Cz method. The resultant crystal boule, doped with 3 at.% Tm, is shown in Figure 4.11(a). This crystal exhibits notable anisotropic thermal properties in the (100) plane, which results in a slight ellipticity in the cross-sectional shape of the crystal boule. The ellipticity is aligned with the principal crystallographic directions along the [010] and [001] axes, indicating the directional dependence of the thermal expansion coefficients. Figure 4.11(b) presents an SEM image of the fracture edge from a mechanically cleaved single-crystal plate of Tm:KYMo. The image distinctly reveals the crystal's natural cleavage characteristics, showing multiple "staircase-like" structures along the fracture edge. These steps run parallel to the **c**-axis within the (100) plane, which highlights the layered nature of the crystal structure. This is consistent with the orthorhombic crystal structure of Tm:KYMo, classified under the space group Pbna. The layered structure contributes to significant spectroscopic anisotropy, as demonstrated in Figures 4.11(c) and 4.11(d).

The spectroscopic properties of the crystal are of particular interest, especially the maximum σ_{SE} for the $^3F_4 \rightarrow {}^3H_6$ transition, which is measured to be 2.70×10^{-20} cm² at a wavelength of 1856 nm. This transition also exhibits a broad bandwidth exceeding 110 nm for light polarized along the E||b axis. The relatively long lifetime of the $^3F_4$ state, recorded at 2.29 ms, indicates

the potential for efficient lasing applications (refer to PAPER VII for more details). Furthermore, the mechanical cleavage of Tm:KYMo along the (100) plane allows for the generation of high-quality crystalline films and plates, which can be as thin as 70 µm. These thin films are crucial for various optical applications, as their thickness and smoothness contribute to the uniformity and quality of the emitted light. To predict the expected emission wavelength, σ_{gain} were calculated. The σ_{gain} spectra, particularly for high-gain light polarized along the E||**b** for the $^3F_4 \rightarrow {}^3H_6$ transition, as depicted in Figure 4.11(e), demonstrate smooth and broad spectral profiles, which are desirable for broad-spectrum laser outputs. Overall, these findings underscore the unique thermal, structural, and spectroscopic properties of Tm:KYMo, making it a promising candidate 2 µm lasers applications

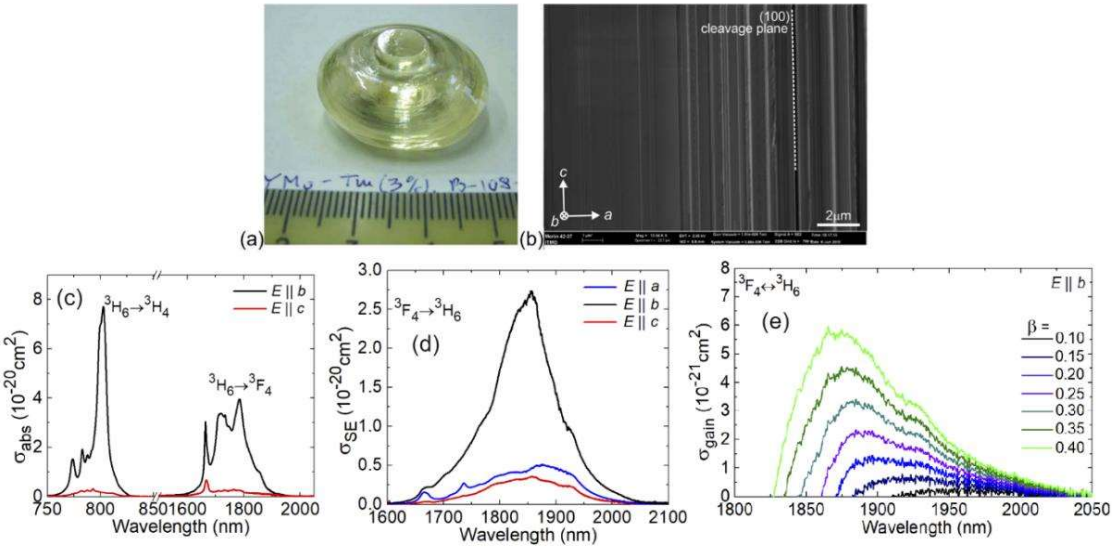

Figure 4.11. (a) Photograph of the as-grown 3 at.% Tm: KYMo crystal boule; (b) Scanning Electron Microscope (SEM) image of the side surface of a cleaved single-crystal film indicating the crystallographic directions; (c) σ_{abs} for the $^3H_6 \rightarrow {}^3F_4$ and $^3H_6 \rightarrow {}^3H_4$ transitions for polarizations E||**b** and E||**c**; (d) σ_{SE} for the $^3F_4 \rightarrow {}^3H_6$ transition; (d) σ_{gain} spectra for E||**b** for the $^3F_4 \rightarrow {}^3H_6$ transition.

For CW laser experiments, two distinct samples were prepared from a 3 at.% Tm:KYMo crystal. The crystal was mechanically cleaved along the (100) crystallographic plane using a precision thin razor blade, resulting in two samples of differing thicknesses. The first sample, referred to as the thin film, had a thickness of 70 ± 5 µm, while the second sample, termed the crystal plate, had a considerably greater thickness of 700 ± 10 µm. These thicknesses were accurately measured and verified using both a micrometer and SEM to ensure precision.

The initial experiment, illustrated in Figure 4.12(a) and (b), concentrated on evaluating the performance of the thicker crystal plate sample. During this experiment, the laser produced a maximum output power of 0.88 W within the wavelength range of 1840–1905 nm. This was achieved with a slope efficiency of 65.8. The laser threshold was recorded at 210 mW, with at T_{OC} set at 5%. However, it was observed that increasing the output coupling beyond this value resulted in a slight reduction in performance. This decline was attributed to upconversion losses, a phenomenon where some of the absorbed energy is lost through non-radiative processes rather than contributing to laser emission.

In the subsequent experiment, depicted in Figure 4.12(c) and (d), the focus shifted to the thinner sample, the 70 µm thin film. In this case, the laser managed to generate a maximum output

power of 131 mW, operating within the wavelength range of 1801–1872 nm. The slope efficiency for this configuration was determined to be 45.2%, and the laser threshold was significantly lower at 35 mW, with a T_{OC} of 1.5%. Notably, the emission from the thin film was found to be linearly polarized (E||**b**). It was also observed that increasing the output coupling led to a rise in the laser threshold, with the threshold increasing from 13 mW at a T_{OC} of 0.1% to 54 mW at a T_{OC} of 9%. Despite these increases, the thresholds remained relatively low, indicating that the thin film could achieve lasing with minimal input power, albeit with a trade-off in output power and efficiency.

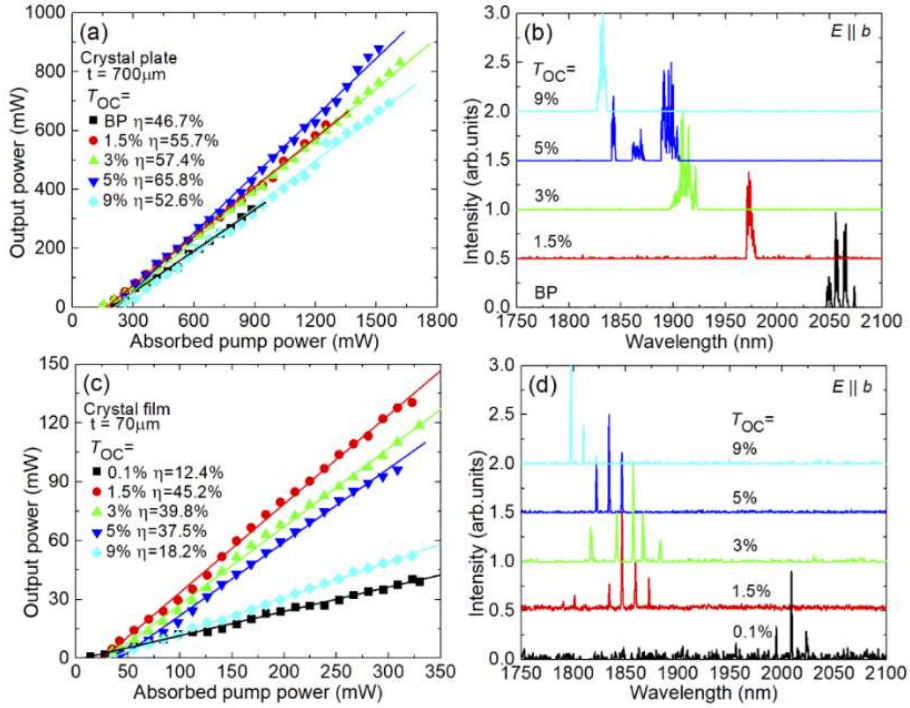

Figure.4.12. Diode-pumped laser performance of (100)-oriented cleaved (a,b) thin-film (thickness (*t*) = 70 μm) and (c,d) crystal-plate (t = 700 μm) 3 at.% Tm: KYMo crystal: (a,c) input-output dependences; (b,d) typical spectra of the laser emission measured at maximum P_{abs}.

4.2.2. Tm-doped calcium lithium tantalum gallium garnet (Tm:CLTGG)

Tantalum (Ta) garnet crystals represent a highly promising category of materials for doping with Tm^{3+} ions, particularly for applications in 2 μm lasers. In the study presented in PAPER VIII, we focused on the Tm^{3+} and Li^{+} codoped calcium tantalum gallium garnet, with the chemical formula $Ca_3Ta_{1.88}Li_{0.20}Ga_{2.80}O_{12}$ (Tm:CLTGG). This study not only demonstrated the 2 μm laser performance of the Tm:CLTGG crystal but also provided an in-depth analysis of its thermo-optical and spectroscopic properties, highlighting its potential for 2 μm laser applications.

The Tm:CLTGG crystal was synthesized using the Cz method, which is widely used for growing high-quality single crystals. The crystal adopts a cubic structure, as illustrated in Figure 4.13(a), with a space group $Ia\bar{3}d$ and a refined lattice constant of a = 12.5158(0) Å, determined through the Rietveld refinement method. A notable feature of this crystal is the structural disorder arising from the random distribution of Ta^{5+}, Ga^{3+}, and Li^{+} cations across the octahedral (16a) and tetrahedral (24d) lattice sites, as depicted in Figure 4.13(b). This disorder contributes to significant inhomogeneous broadening of the Tm^{3+} absorption and

emission bands, which is advantageous for generating wide gain spectra, as evidenced in Figures 4.13(c) and (d). Furthermore, the Tm:CLTGG crystal exhibits high thermal conductivity, measured at 4.33 $Wm^{-1}K^{-1}$, which is a critical parameter for efficient laser operation, as it facilitates the dissipation of heat generated during lasing. Raman spectroscopy studies reveal a low concentration of vacancies within the crystal lattice, which is attributed to the codoping with Li^{+} ions that provide charge compensation and stabilize the crystal structure.

Additionally, at a temperature of 10K, the crystal-field splitting of the Tm^{3+} multiplets was observed, offering insights into the electronic structure of the dopant ions within the host lattice. Transition probabilities for the observed electronic transitions were calculated using the Judd-Ofelt (mJ-O) theory, yielding intensity parameters $\Omega_2 = 5.185$, $\Omega_4 = 0.650$, $\Omega_6 = 1.068$ [10^{-20} cm^2], and an α parameter of 0.171 [10^{-4} cm]. These parameters are crucial for understanding the spectroscopic behavior of the Tm:CLTGG crystal and optimizing it for laser performance. The crystal-field splitting at 10K further reinforces the detailed understanding of the Tm^{3+} ion environment within the crystal, as discussed in PAPER VIII.

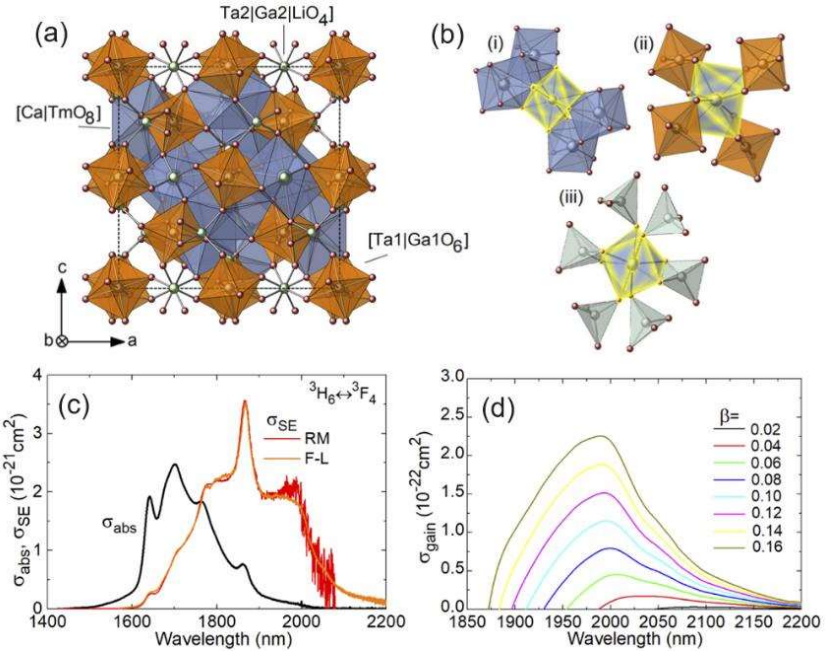

Figure 4.13. Crystal structure of Tm:CLTGG: (a) projection of the crystal structure parallel to the a-c plane, (b) the variety of cationic distributions around Ca^{2+}|Tm^{3+} ions occupying the dodecahedral 24c sites: nearest-neighbor cations at: (i) dodecahedral 24c sites, (ii) octahedral 16a sites and (iii) tetrahedral 24d sites; (c-d) $^3H_6 \leftrightarrow {}^3F_4$ transition of Tm^{3+} ions in CLTGG: (c) σ_{abs} and σ_{SE} spectra (d) gain cross-sections.

The first diode-pumped Tm:CLTGG laser was demonstrated, and the results are illustrated in Figure 4.14. A compact microchip laser cavity pumped by 793 nm- laser diode was used in laser experience in the CW regime . We achieved an output of 1.08 W around 2 µm with a slope efficiency of 23.8%. The structural disorder in the CLTGG crystal, due to the random distribution of Ta^{5+} and Ga^{3+} cations in the octahedral and tetrahedral sites, causes significant inhomogeneous spectral broadening of the Tm^{3+} ions. This disorder results in smooth and broad gain profiles with a 130 nm bandwidth extending beyond 2 µm, making Tm:CLTGG ideal for generating femtosecond pulses.

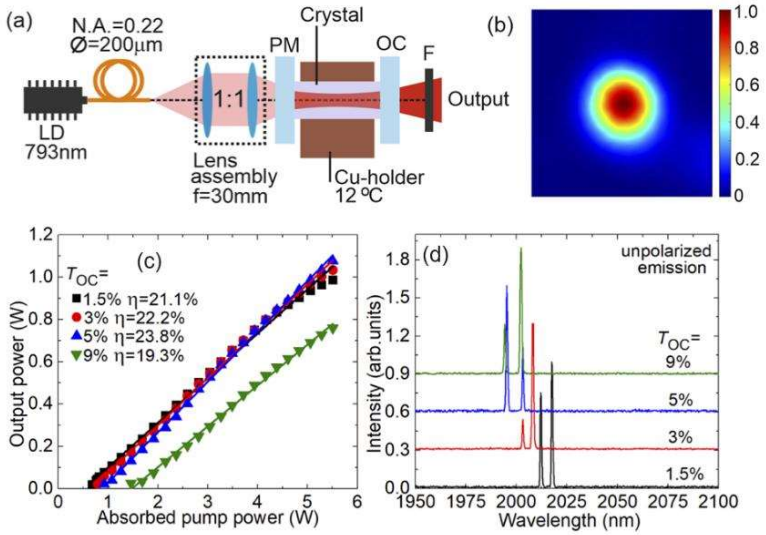

Figure 4.14. (a) Scheme of the diode-pumped compact Tm:CLTGG laser: LD – laser diode, PM – pump mirror, OC – output coupler, F – cut-on filter; (b) far-field output profile of the laser mode, T_{OC} = 5%, P_{abs} = 4.0 W; (c) input-output dependences; (d) typical spectra of unpolarized laser emission measured at maximum P_{abs}.

4.2.3. Disordered Tm^{3+}, Ho^{3+}-codoped CNGG garnet crystal

Another garnet crystal was examined for generating laser at ~2 µm. It's the disordered calcium niobium gallium garnet−$Ca_3(NbGa)_5O_{12}$ (denoted as CNGG), codoped with Tm and Ho. The codoping of Tm and Ho ions leverages the unique spectroscopic and energy transfer properties of both ions to enhance laser performance. Tm^{3+} ions absorb pump light at ~800 nm efficiently and transfer energy to Ho^{3+} ions, which then emit laser at ~2 µm. This energy transfer mechanism allows for efficient operation and high output power. This approach was discussed in detail in the paper related to this crystal, PAPER IX.

The Tm, Ho-codoped CNGG crystal was grown using the conventional Cz method. The resulting crystal boule, containing 2.64 at.% Tm and 0.55 at.% Ho, is depicted in Figure 4.15(a). Its cubic structure (space group $Ia\bar{3}d$ - O^{10}_h, a = 12.4952(1) Å) was refined using the Rietveld method, which revealed a random distribution of Ga^{3+} and Nb^{5+} cations across octahedral and tetrahedral sites, as shown in Figure 4.15(b). σ_{abs} for the $^3H_6 \rightarrow {}^3H_4$ transition of Tm^{3+} in Tm, Ho: CNGG are presented in Figure 4.15(c). The crystal showed a maximum σ_{abs} of 0.54×10^{-20} cm² at 786.3 nm and a FWHM of 28.4 nm.
For the $^5I_7 \leftrightarrow {}^5I_8$ transition of Ho^{3+}. The maximum σ_{SE} is 0.47×10^{-20} cm² at 2080.7 nm, Figure 4.15(d) . The gain bandwidth of Tm, Ho:CNGG around 2 µm exceeds 150 nm, and the thermal equilibrium decay time is 6.80 ms. The J-O theory, incorporating ICI approximations, was used to determine the transition probabilities for Ho^{3+}. Additionally, the energy transfer parameters between Tm^{3+} and Ho^{3+} were determined, further illustrating the effectiveness of this codoped crystal for ~2 µm-laser applications (see paper IX).

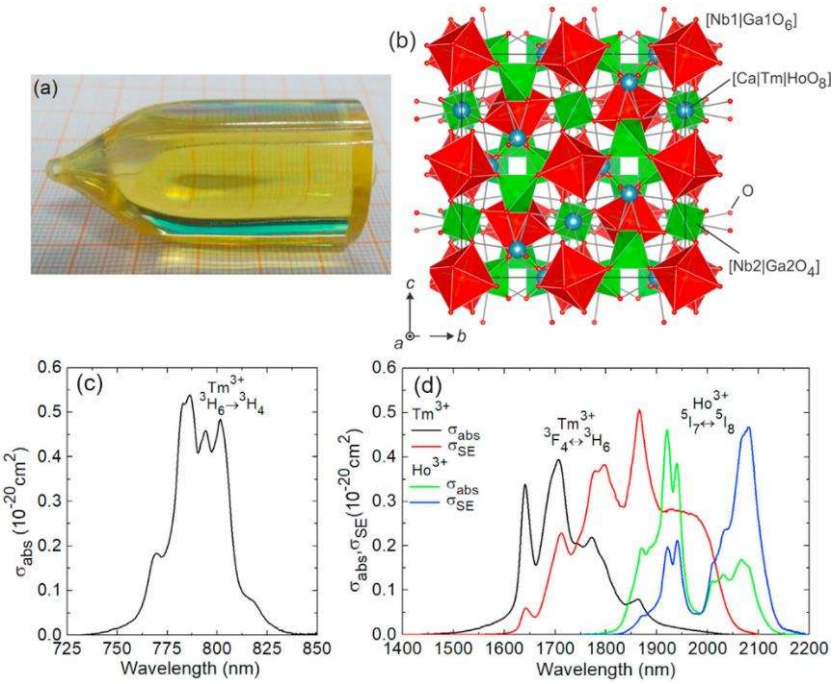

Figure.4.15. (a) Photograph of the as-grown Tm, Ho:CNGG crystal, the growth direction is along the [111] axis; (b) fragment of crystal structure in projection on the b-c plane; Spectroscopy of Tm^{3+} and Ho^{3+} ions in CNGG: (c) σ_{abs} spectrum for the $^3H_6 \rightarrow {}^3H_4$ Tm^{3+} transition; (d) σ_{abs} and σ_{SE} spectra for the $^3F_4 \leftrightarrow {}^3H_6$ (Tm^{3+}) and $^5I_7 \leftrightarrow {}^5I_8$ (Ho^{3+}) transitions.

A four-mirror X-shaped cavity was used to assess the laser performance of Tm, Ho:CNGG. The detailed description of this laser cavity is described in PAPER IX. Operating in a CW free-running regime, as illustrated in Figure 4.16(a) and (b), the laser produced 425 mW at 2083.7 nm with a slope efficiency of 22.9% for a 3.0% T_{OC}. The laser threshold showed a slight increase with higher output coupling, rising from 80 mW P_{abs} for 0.2% T_{OC} to 136 mW for 3.0% T_{OC}. The output power dependencies were linear, though power scaling was constrained by the available pump power.

To explore wavelength tuning capability of this laser, a Lyon filter was inserted into the cavity near the OC. Tuning characteristics were examined using T_{OCs} of 0.2% and 0.5%. The laser achieved continuous wavelength tuning from 1932.5 to 2142.1 nm with a 0.5% OC, and from 1940.3 to 2144.6 nm with a 0.2% OC, providing a tuning range exceeding 200 nm in both cases (measured at the zero-power level). The effective gain cross-section ($\sigma_{g,eff}$) spectra for Tm, Ho:CNGG were calculated to elucidate the observed wavelength tuning performance, as depicted in Figure 4.16(c).

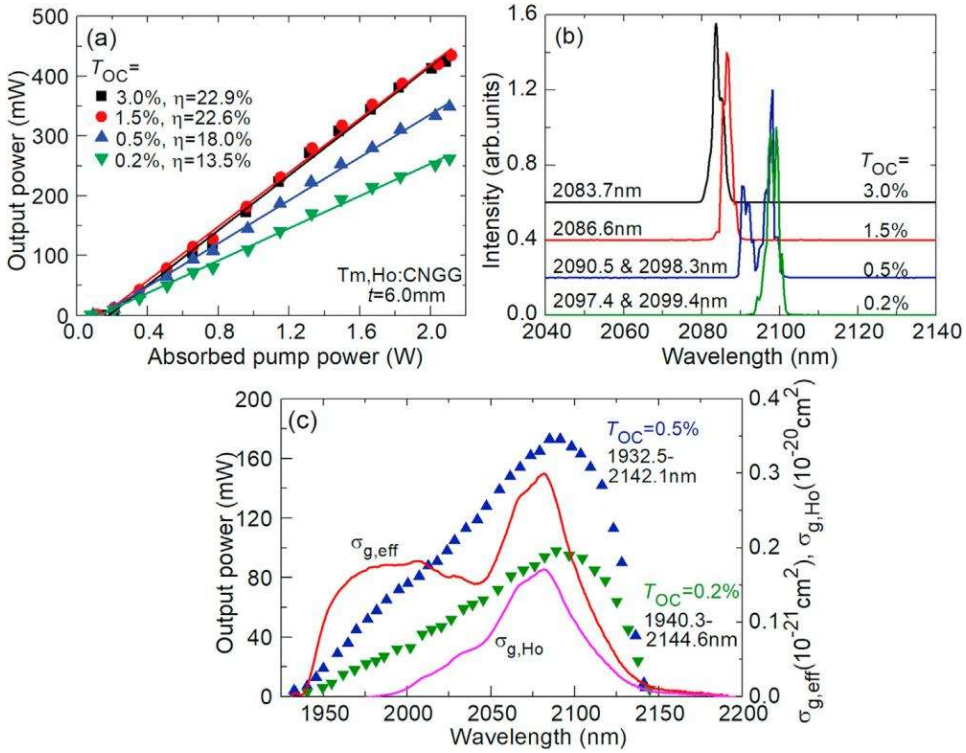

Figure.4.16. CW laser performance of the Tm,Ho:CNGG laser pumped by a Ti:Sapphire laser at 785.6 nm: (a,b) free-running operation, (a) input-output dependences (b) typical laser emission spectra; (c) calculated effective gain. The laser emission is linearly polarized.

4.2.4. Cryogenic Tm: $LiYF_4$ (shortly Tm: YLF) laser at ~ 2 µm

In solid-state lasers, cryogenic cooling of the laser medium is a technique employed to enhance the crucial thermo-optic properties of the laser crystal. This method significantly improves the thermal conductivity of the material, reduces the temperature-dependent variation in the refractive index, and decreases the thermal expansion coefficient of the crystal. By achieving these improvements, the cryogenic cooling approach effectively minimizes the adverse thermo-optic effects that can degrade laser performance. In the referenced study, referred to here as PAPER X, the influence of cryogenic cooling on the performance of a Tm:$LiYF_4$ (Tm:YLF) laser was investigated for the first time in the CW regime. This research marks a significant milestone as it explores the potential benefits of cryogenic cooling on Tm:YLF lasers, which are known for their application in many laser systems.

A successful cryogenic CW laser operation was achieved using a Tm:YLF crystal with a doping concentration of 5 atomic percent. The experimental setup employed a modular configuration, utilizing a VBG-stabilized LD as the pump source with a wavelength centered at 793 nm. The designed cavity is depicted in Figures 4.17(a-b). The laser resonator was designed as a compact microchip cavity specifically adapted for cryogenic temperatures. The cavity design included a plane pump mirror that was HR in the 1.8–2.1 µm wavelength range and HT around 800 nm. Various OCs with T_{OC} of 9%, 15%, and 30% at the desired emission wavelengths were utilized to optimize the laser performance. The active laser medium in this setup was a commercially available a-cut Tm:YLF crystal with 5 at.% doping. The crystal measured 2 mm in thickness with a 5×5 mm² aperture and was securely mounted in a copper holder. This configuration formed a compact plane–plane laser cavity housed within a modular chamber. Conductive cooling of the laser crystal was achieved by attaching the copper holder and the laser crystal to

the cold finger of a closed-cycle helium cryostat (model CH-204 by JANIS), capable of delivering a cooling power of 13.5 watts at 100 Kelvin (K).

At an operating temperature of 80 K, the experimental setup produced a maximum output power of approximately 6.5 W, achieving a slope efficiency of 38% relative to the incident pump power. The resulting laser beam exhibited excellent quality, as illustrated in Figure 4.17(c). As the temperature increased to 160 K, a slight blue shift in the laser wavelength was observed, indicating that at this temperature, a portion of the ground state electronic population contributed to a quasi-three-level laser operation, as shown in Figure 4.17(d). At lower temperatures, the Tm:YLF laser transitioned to a four-level operation, eliminating reabsorption losses. Additional absorption measurements of the crystal at 80 K, conducted under non-lasing conditions, revealed an absorption efficiency of 57%. This figure accounted for Fresnel losses on the crystal surface and a second pass of the pump light, which was partially reflected by the output coupler. This detailed investigation highlights the advantages of cryogenic cooling in enhancing the performance of Tm:YLF lasers. The findings contribute valuable insights into the design and optimization of high-performance laser systems utilizing cryogenic technology.

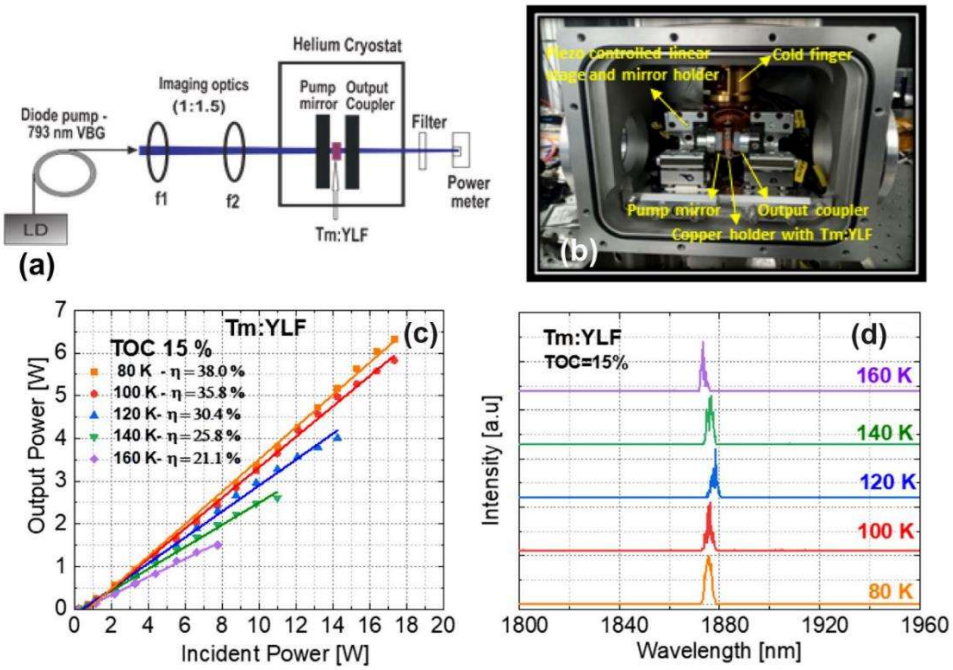

Figure 4.17. (a) Cryogenic compact laser setup; LD laser diode imaging optics—achromatic lenses (f1= 100 mm and f2= 150 mm); (b) Modular chamber used for the experiment; (c) Output power vs. input power characteristics of the cryogenic compact Tm: YLF laser for various crystal temperatures; (d) Corresponding output laser wavelengths.

CONCLUSIONS AND FUTURE WORK

CONCLUSIONS AND FUTURE WORK

Conclusions

This PhD Thesis has dealt with the fabrication and the characterization of novel and efficient lasers operating in the CW and passively *Q*-switched operation regimes, at RT and at cryogenic conditions, in the NIR at ~1 μm and ~2 μm. This was achieved by using novel laser crystalline materials as hosts for Nd, Yb for the wavelength ~1 μm and with Tm and/or Ho for the range ~2 μm. Different crystal growth methods (Cz method, OFZ method, LTG Cz method) were used to grow the studied gain media (compositionally mixed aluminate garnet, gallium garnets, double molybdates, oxoborates and fluorides crystals). The studied laser gain materials were chosen due to their ability to generate stable laser emission (polarized lasers for anisotropic crystals and unpolarized for the isotropic materials) and their high gain cross-sections, which make them suitable for achieving efficient and robust lasers devices in the NIR spectral range. Different characterization techniques (i.e., structural: XRD, Raman, etc..; spectroscopic: optical absorption, luminescence and luminescence lifetime) were performed to access the quality and suitability of the materials.

CW laser operation in the NIR at ~1 μm were successfully achieved using materials doped with Yb and Nd. The compositionally mixed Yb:$(Y,Lu)_3Al_5O_{12}$ aluminate garnet was grown by the Cz method. Its structural, vibronic, spectroscopic, and laser characteristics were thoroughly examined. The material displays favorable spectroscopic properties for Yb^{3+} ion doping, featuring a broad absorption band near 940 nm that aligns well with the emission from InGaAs laser diodes. In microchip geometry, power scaling was achieved, resulting in an output power of about 9 W at approximately 1.05 μm, with a slope efficiency of 76%. This mixed Yb:$(Y,Lu)_3Al_5O_{12}$ holds significant potential for developing diode-pumped, power-scalable lasers operating at 1 μm. The double molybdate crystal Yb:KYMo with layered structure was also studied in this thesis. This crystal demonstrated strong polarization anisotropy in the transition cross-sections of the Yb^{3+} ions and had an ideal natural cleavage along the (100) crystallographic plane. Utilizing a 3 at.% Yb:KYMo crystal-plate, a diode-pumped microchip laser achieved a watt-level output with a slope efficiency of 76.4%, nearing the Stokes limit. Yb:GdCB oxoborate is an attractive laser crystal due to its broadband emission around ~1 μm. This material boasts multiple cationic sites with distorted VIII-fold and VII-fold coordination, which are irregularly filled by Ca^{2+} and $Gd^{3+}|Yb^{3+}$ cations. This results in a highly significant inhomogeneous broadening of Yb^{3+} ions' absorption and emission bands, creating a "glassy-like" spectroscopic behavior. Yb: GdCB laser was tested under high-power diode pumping at 976 nm across three crystal orientations along the crystallographic axes. The optimum results were obtained using **a**-cut sample, where we achieved maximum output power of 5.58 W at 1057 nm, with a slope efficiency of 51.7% and linear laser polarization (E||**c**).

1 μm lasers based on Yb-doped garnet gain medium operated at cryogenic temperature showed a great capability of power scalability with excellent laser beam profile. The CW cryogenic laser operation with the Yb:YGG gallium garnet crystal succeeded to record a maximum output power of 17.50 W at 120 K with a slope efficiency of 87% with respect to the absorbed power. Indeed, Yb:$(Y,Lu)_3Al_5O_{12}$ crystal is attractive for the development of high-power diode-pumped cryogenic lasers emitting at ~ 1030 nm. This crystal at the optimum cryogenic temperature generated near 10 W of CW laser output power. By employing Cr^{4+}:YAG based saturable

absorbers, for the passively *Q*-switched cryogenic laser, the best pulse characteristics (energy/duration) were 0.15 mJ/201 ns at a repetition rate of 39.7 KHz.

The monoclinic Nd:CsGdMo, with a space group *P2/c*, is a promising double molybdate compound for laser applications at ~1 μm. This material has a layered crystal structure that facilitates perfect cleavage along the (100) plane, making it easy to fabricate high-quality optical crystal plates and potentially thin crystal films with thicknesses down to hundreds of microns, which are ideal for thin-disk lasers. Using a thin plate that was mechanically cleaved from this crystal, an efficient CW laser operation was demonstrated in a microchip-type laser cavity. This laser achieved an output of up to 0.54 W at 1066 nm with a high slope efficiency of 60.4%, a low laser threshold of 70 mW, and linearly polarized emission.

Lasers operating in the NIR spectrum, doped with trivalent Tm and Ho ions, excel at producing efficient lasing within the eye-safe region near 2 μm. The orthorhombic double molybdate crystal known as Tm:KYMo stands out as a particularly effective material for lasers within this spectrum due to its straightforward growth process, high doping capacity, intense, broad, and highly polarized absorption and emission bands, along with its Raman activity. The layered structure of KYMo enhances the anisotropy of its optical characteristics, facilitating the growth of high-quality laser crystal plates and films with varying thicknesses from several millimeters to a few tens of microns. This characteristic is particularly advantageous for applications in microchip and thin-disk lasers. Employing the as-grown Tm: KYMo, 2 μm CW laser operation was achieved in single-crystal plates (sub-mm) and films (sub-100 μm) with 65.8% slope efficiency and nearly watt-level output in passively cooled microchip cavity. Another novel material, Tm:CLTGG, was investigated in this thesis, showcasing broad emission properties around 2 μm. The first diode-pumped laser from this crystal reached 1.08 W at approximately 2 μm with a 23.8% slope efficiency. The Tm^{3+} ions in CLTGG showed notable inhomogeneous spectral broadening, a result of structural disorder from the random placement of Ta^{5+} and Ga^{3+} cations across octahedral and tetrahedral lattice sites, leading to broad and smooth gain profiles (bandwidth: 130 nm) that extend up to about 2.2 μm, making the Tm:CLTGG crystal ideal for femtosecond pulse generation.

The Tm and Ho-co-doped disordered CNGG garnet is well-suited for generating broadly tunable lasers that emit slightly over 2 μm, thanks to its unique spectroscopic features. These include (i) a wide and smooth emission spectrum near 2 μm, (ii) an efficient and predominantly direct energy transfer from Tm to Ho, (iii) a relatively lengthy lifetime of Ho's upper laser level, with the thermal equilibrium lifetime of the Tm and Ho system, facilitating a relatively low threshold for laser operation, and (iv) contributions from both Tm^{3+} and Ho^{3+} ions that extend the gain spectrum across more than 150 nm. Operating in CW (free running) regime, this laser delivered 425 mW at 2083.7 nm with a 22.9% efficiency and managed more than 200 nm of continuous tuning of the emission wavelength. Furthermore, in cryogenic conditions at 80 K, a CW laser operation was efficiently carried out in a Tm:YLF crystal in microchip geometry, reaching a maximum output power of 6.5 W and a slope efficiency of 66% relative to absorbed power, maintaining an excellent beam profile.

Perspectives & future work

Laser waveguides operating in CW and mode-locked regimes.

The results of this PhD Thesis are promising for future research aimed at developing compact laser waveguide devices capable of operating in either CW or mode-locked regimes. There is a significant demand for ultra-compact laser systems suitable for practical applications.

Recent developments have demonstrated that waveguides etched directly into laser gain media represent a top method for miniaturizing solid-state lasers. Through the use of femtosecond direct laser writing (fs-DLW), these technologies facilitate the tight confinement of the laser beam in channel waveguides of micrometer scale, thus ensuring high efficiency and stable single-mode performance. Moreover, ultrafast laser waveguides that operate at high repetition rates in mode-locked regimes reaching MHz/GHz-levels can be efficiently developed from a compact and fundamentally mode-locked laser setups. Such laser systems are indispensable for various advanced scientific fields, including astronomy, metrology with frequency combs, and on-chip integrated photonics.

Thin-disk lasers for high power laser applications.

Thin-disk lasers doped with Tm, Ho, or Yb are at the forefront of high-power laser technology, offering unique advantages for a range of demanding applications. Some of the developed gain media will be studied for thin-disk lasers due to their unique advantages such as high absorption cross-sections or high thermal conductivity that may reduce the required number of passes of the pump through the active medium and reduce the complexity of the existing thin-disk lasers. These lasers utilize a thin, disk-shaped gain medium, which significantly enhances thermal management and enables efficient heat dissipation. The geometry of thin-disk lasers is particularly advantageous for high-power operation, as it minimizes thermal lensing and allows for higher output powers without compromising beam quality.

REFERENCES

References

1. K. Scholle, E. Heumann, and G. Huber, "Single mode Tm and Tm,Ho:LuAG lasers for LIDAR applications," Laser Phys. Lett. **1**(6), 285–290 (2004).
2. N. Sugimoto, K. Chan, N. Sims, and D. K. Killinger, "Eye-safe 2.1-μm Ho lidar for measuring atmospheric density profiles," Opt. Lett. **15**(6), 302–304 (1990).
3. J. Rothhardt, S. Hädrich, J. C. Delagnes, E. Cormier, and J. Limpert, "High Average Power Near-Infrared Few-Cycle Lasers," Laser Photon. Rev. **11**(4), 1700043 (2017).
4. L. Mahler and A. Tredicucci, "Photonic engineering of surface-emitting terahertz quantum cascade lasers," Laser Photon. Rev. **5**(5), 647–658 (2011).
5. J. Shemshad, S. M. Aminossadati, and M. S. Kizil, "A review of developments in near infrared methane detection based on tunable diode laser," Sensors Actuators B Chem. **171**–**172**, 77–92 (2012).
6. J. A. Wahr, K. K. Tremper, S. Samra, and D. T. Delpy, "Near-Infrared spectroscopy: Theory and applications," J. Cardiothorac. Vasc. Anesth. **10**(3), 406–418 (1996).
7. V. Petrov, M. C. Pujol, X. Mateos, Ò. Silvestre, S. Rivier, M. Aguiló, R. M. Solé, J. Liu, U. Griebner, and F. Díaz, "Growth and properties of $KLu(WO_4)_2$, and novel ytterbium and thulium lasers based on this monoclinic crystalline host," Laser Photon. Rev. **1**(2), 179–212 (2007).
8. B. Zohuri, "Laser Weapons," Dir. Energy Weapons 47–77 (2016).
9. Q. Ji, S. Zong, and J. Yang, "Application and development trend of laser technology in military field," History of science and technology, **12**(1), 32–40 (2020).
10. B. Jiang, S. Zhu, L. Ren, L. Shi, and X. Zhang, "Simultaneous ultraviolet, visible, and near-infrared continuous-wave lasing in a rare-earth-doped microcavity," Advanced Photonics **4**(4) **4**(4), 046003 (2022).
11. H. Nie, F. Wang, J. Liu, K. Yang, K. Yang, B. Zhang, B. Zhang, J. He, and J. He, "Rare-earth ions-doped mid-infrared (2.7–3 μm) bulk lasers: a review [Invited]," Chinese Opt. Lett. **19**(9), 091407- (2021).
12. Z. Liu, A. Ikesue, and J. Li, "Research progress and prospects of rare-earth doped sesquioxide laser ceramics," J. Eur. Ceram. Soc. **41**(7), 3895–3910 (2021).
13. M. K. Hossain, S. Hossain, M. H. Ahmed, M. I. Khan, N. Haque, and G. A. Raihan, "A Review on Optical Applications, Prospects, and Challenges of Rare-Earth Oxides," ACS Appl. Electron. Mater. **3**(9), 3715–3746 (2021).
14. T. Zhong and P. Goldner, "Emerging rare-earth doped material platforms for quantum nanophotonics," Nanophotonics **8**(11), 2003–2015 (2019).
15. E. A. Anashkina, "Laser Sources Based on Rare-Earth Ion Doped Tellurite Glass Fibers and Microspheres," Fibers 2020, **8**(5), 30 (2020).
16. G. Charalampides, K. I. Vatalis, B. Apostoplos, and B. Ploutarch-Nikolas, "Rare Earth Elements: Industrial Applications and Economic Dependency of Europe," Procedia Econ. Financ. **24**, 126–135 (2015).
17. M. K. Hossain, M. I. Khan, and A. El-Denglawey, "A review on biomedical applications, prospects, and challenges of rare earth oxides," Appl. Mater. Today **24**, 101104 (2021).
18. S. Luo, X. Yan, Q. Cui, B. Xu, H. Xu, and Z. Cai, "Power scaling of blue-diode-pumped Pr:YLF lasers at 523.0, 604.1, 606.9, 639.4, 697.8 and 720.9 nm," Opt. Commun. **380**, 357–360 (2016).
19. J. Galbraith, T. Galvin, I. Tamer, H. Neurath, T. Spinka, A. Church, B. A. Reagan, E. Sistrunk, and G. Huete, "Demonstration of a compact, multi-joule, diode-pumped Tm:YLF laser," Opt. Lett. **46**(20), 5096–5099 (2021).
20. S. Ye, X. Zhou, S. Huang, S. Huang, H. Nie, H. Nie, J. Bian, T. Li, T. Li, K. Yang, K. Yang, J. He, J. He, J. He, B. Zhang, and B. Zhang, "Cascade MIR Ho:YLF laser at 2.1 μm and 2.9 μm," Opt. Lett. **47**(21), 5642–5645 (2022).
21. G. D. Gautam and A. K. Pandey, "Pulsed Nd:YAG laser beam drilling: A review," Opt. Laser Technol. **100**, 183–215 (2018).
22. L. Hu, D. He, H. Chen, X. Wang, T. Meng, L. Wen, J. Hu, Y. Xu, S. Li, Y. Chen, W. Chen, S. Chen, J. Tang, and B. Wang, "Research and development of neodymium phosphate laser glass for high power laser application," Opt. Mater. (Amst). **63**, 213–220 (2017).

23. B. Azadgoli and R. Y. Baker, "Laser applications in surgery," Ann. Transl. Med. **4**(23), (2016).
24. Y. Saydjari, T. Kuypers, and N. Gutknecht, "Laser Application in Dentistry: Irradiation Effects of Nd:YAG 1064 nm and Diode 810 nm and 980 nm in Infected Root Canals—A Literature Overview," Biomed Res. Int. **2016**(1), 8421656 (2016).
25. K. Chen, D. Xu, Y. Sun, J. Li, C. Yan, S. Liu, Y. Wang, K. Zhong, J. Yao, and J. Yao, "1064 nm laser pumped optical parametric oscillator based on BaGa4Se7 crystal at 1 kHz repetition rate," Opt. Laser Technol. **171**, 110455 (2024).
26. X. Lei, J. Ma, H. Liu, Z. Wang, G. Jin, and Y. Yu, "Compact, thermally boosted direct pumped Nd:MgO:PPLN, mid-infrared self-optical parametric oscillator," Opt. Laser Technol. **180**, 111405 (2025).
27. K. Zhong, "Laser Performance of Neodymium- and Erbium-Doped GYSGG Crystals," Cryst. 2019, Vol. 9, Page 220 **9**(4), 220 (2019).
28. G. Olivi and M. Olivi, "Laser–Hard Tissue Interaction," Lasers Restor. Dent. 51–85 (2015).
29. S. Wachsmann-Hogiu, A. J. Annala, and D. L. Farkas, "Laser Applications in Biology and Biotechnology," Handb. Laser Technol. Appl. 321–344 (2021).
30. S. Parker, M. Cronshaw, E. Anagnostaki, V. Mylona, E. Lynch, and M. Grootveld, "Current Concepts of Laser–Oral Tissue Interaction," Dent. J. 2020, Vol. 8, Page 61 **8**(3), 61 (2020).
31. B. M. Walsh, "Review of Tm and Ho materials; spectroscopy and lasers," Laser Phys. **19**(4), 855–866 (2009).
32. S. Cimino, V. Favilla, G. I. Russo, A. Saita, G. Sortino, T. Castelli, M. Veroux, M. Madonia, and G. Morgia, "Pneumatic Lithotripsy versus Holmium:YAG Laser Lithotripsy for the Treatment of Single Ureteral Stones: A Prospective, Single-Blinded Study," Urol. Int. **92**(4), 468–472 (2014).
33. A. J. Marks and J. M. H. Teichman, "Lasers in clinical urology: State of the art and new horizons," World J. Urol. **25**(3), 227–233 (2007).
34. S. Thomas, J. Pensel, R. Engelhardt, W. Meyer, and A. G. Hofstetter, "The pulsed dye laser versus the Q-switched Nd:YAG laser in laser-induced shock-wave lithotripsy," Lasers Surg. Med. **8**(4), 363–370 (1988).
35. J. Helou, I. Maatouk, M. A. Hajjar, and R. Moutran, "Evaluation of Nd:YAG laser device efficacy on onychomycosis: a case series of 30 patients," Mycoses **59**(1), 7–11 (2016).
36. T. Mizuno, T. Kase, T. Shiina, M. Mita, N. Namiki, H. Senshu, R. Yamada, H. Noda, H. Kunimori, N. Hirata, F. Terui, and Y. Mimasu, "Development of the Laser Altimeter (LIDAR) for Hayabusa2," Space Sci. Rev. **208**(1–4), 33–47 (2017).
37. K. Scholle, E. Heumann, and G. Huber, "Single mode Tm and Tm,Ho:LuAG lasers for LIDAR applications," Laser Phys. Lett. **1**(6), 285–290 (2004).
38. U. Wandinger, "Introduction to Lidar," Lidar 1–18 (2005).
39. A. Comerón, C. Muñoz-Porcar, F. Rocadenbosch, A. Rodríguez-Gómez, and M. Sicard, "Current Research in Lidar Technology Used for the Remote Sensing of Atmospheric Aerosols," Sensors 2017, **17**(6), 1450 (2017).
40. X. Bi, "LiDAR Technology," Unmanned Syst. Technol. 67–103 (2021).
41. M. N. Favorskaya and L. C. Jain, "Overview of LiDAR Technologies and Equipment for Land Cover Scanning," Intell. Syst. Ref. Libr. **122**, 19–68 (2017).
42. A. M. Wallace, A. Halimi, and G. S. Buller, "Full Waveform LiDAR for Adverse Weather Conditions," IEEE Trans. Veh. Technol. **69**(7), 7064–7077 (2020).
43. S. Ishii, H. Iwai, H. Fukuoka, T. Isikawa, M. Aoki, K. Mizutani, R. Otsuka, and A. Sato, "2 μm Doppler wind lidar with a Tm:fiber-laser-pumped Ho:YLF laser," Opt. Lett. Vol. 43, Issue 2, pp. 202-205 **43**(2), 202–205 (2018).
44. S. Ishii, A. Sato, M. Aoki, K. Akahane, S. Nagano, K. Nakagawa, K. Sato, and H. Okamoto, "Development of Tm,Ho: YLF laser for future space-based doppler wind lidar," https://doi.org/10.1117/12.2324388 **10779**, 13–19 (2018).
45. F. Mörz, A. Steinmann, T. Steinle, M. Nägele, H. Linnenbank, and H. Giessen, "Compact harmonic cavity optical parametric oscillator for optical parametric amplifier seeding," Opt. Express, **28**(17), 25000–25006 (2020).
46. C. L. Tang, W. R. Bosenberg, U. Takashi, R. J. Lane, and L. K. Cheng, "Optical Parametric Oscillators," Proc. IEEE **80**(3), 365–374 (1992).

47. J. M. Melkonian, A. Godard, M. Lefebvre, and E. Rosencher, "Pulsed optical parametric oscillators with intracavity optical parametric amplification: A critical study," Appl. Phys. B Lasers Opt. **86**(4), 633–642 (2007).
48. S. X. Xia, C. H. Yang, G. Li, G. L. Zhu, B. Q. Yao, and Z. T. Lei, "Growth of high quality non-linear optical crystal zinc germanium phosphide for Mid-infrared optical parametric oscillator," Laser Phys. **21**(8), 1366–1370 (2011).
49. S. Cheng, X. Zhang, X. Kong, T. Liu, J. Yan, T. Prikhna, Y. Shang, Z. Lei, and C. Yang, "Enhanced near-infrared optical transmission in zinc germanium phosphide crystals via precise magnesium doping," Phys. Chem. Chem. Phys. **26**(24), 17282–17291 (2024).
50. N. Dalloz, T. Robin, B. Cadier, C. Kieleck, M. Eichhorn, and A. Hildenbrand-Dhollande, "High power Q-switched Tm^{3+}, Ho^{3+}-codoped 2µm fiber laser and application for direct OPO pumping," Proc. SPIE, Fiber Lasers XVI: Technology and Systems, **10897**, 90–97 (2019).
51. G. L. Zhu, Y. L. Ju, C. H. Zhang, B. Q. Yao, and Y. Z. Wang, "High-power, high-quality ZGP OPO pumped by a Tm,Ho:$GdVO_4$ laser," Laser Phys. **20**(6), 1341–1343 (2010).
52. E. P. Chicklis, C. A. Miller, P. A. Budni, J. R. Mosto, L. A. Pomeranz, and M. L. Lemons, "Efficient mid-infrared laser using 1.9-µm-pumped Ho:YAG and $ZnGeP_2$ optical parametric oscillators," JOSA B, **17**(5), 723–728 (2000).
53. M. Piotrowski, M. A. Medina, M. A. Medina, M. Schellhorn, G. Spindler, and A. Hildenbrand-Dhollande, "Effects of pump pulse energy and repetition rate on beam quality in a high-power mid-infrared $ZnGeP_2$ OPO," Opt. Express, **29**(2), 2577–2586 (2021).
54. K. Wang, M. Gao, S. Yu, J. Ning, Z. Xie, X. Lv, G. Zhao, and S. Zhu, "A compact and high efficiency intracavity OPO based on periodically poled lithium niobate," Sci. Reports 2021 111 **11**(1), 1–8 (2021).
55. B. Nandy, S. C. Kumar, M. Ebrahim-Zadeh, and M. Ebrahim-Zadeh, "Yb-fiber-pumped high-average-power picosecond optical parametric oscillator tunable across 1.3−1.5 µm," Opt. Express, **30**(10), 16340–16350 (2022).
56. S. K. Sarkar, "Lasers in Materials Processing and Synthesis," Handbook on Synthesis Strategies for Advanced Materials, 791–831 (2022).
57. L. Li, "The advances and characteristics of high-power diode laser materials processing," Opt. Lasers Eng. **34**(4–6), 231–253 (2000).
58. J. Dutta Majumdar and I. Manna, "Laser material processing," Int. Mater. Rev. **56**(5–6), 341–388 (2011).
59. J. Dutta Majumdar and I. Manna, "Laser processing of materials," Sadhana - Acad. Proc. Eng. Sci. **28**(3–4), 495–562 (2003).
60. J. Min, H. Wan, B. E. Carlson, J. Lin, and C. Sun, "Application of laser ablation in adhesive bonding of metallic materials: A review," Opt. Laser Technol. **128**, 106188 (2020).
61. T. Y. Fan, "Quasi-Three-Level Lasers," 189–203 (1993).
62. R. J. Beach, "Optimization of Quasi-Three Level End-Pumped Q-Switched Lasers," IEEE J. Quantum Electron. **31**(9), 1606–1613 (1995).
63. D. C. Brown and V. A. Vitali, "Yb:YAG kinetics model including saturation and power conservation," IEEE J. Quantum Electron. **47**(1), 3–12 (2011).
64. C. A. Wang, T. Y. Fan, P. Lacovara, H. K. Choi, and R. L. Aggarwal, "Room-temperature diode-pumped Yb:YAG laser," Opt. Lett. Vol. 16, Issue 14, pp. 1089-1091 **16**(14), 1089–1091 (1991).
65. L. I. Ivleva, T. T. Basiev, I. S. Voronina, P. G. Zverev, V. V. Osiko, and N. M. Polozkov, "$SrWO_4$:Nd^{3+} – new material for multifunctional lasers," Opt. Mater. (Amst). **23**(1–2), 439–442 (2003).
66. J. Lu, T. Murai, K. Takaichi, T. Uematsu, K. Misawa, M. Prabhu, J. Xu, K. Ueda, H. Yagi, T. Yanagitani, A. A. Kaminskii, and A. Kudryashov, "72 W Nd:$Y_3Al_5O_{12}$ ceramic laser," Appl. Phys. Lett. **78**(23), 3586–3588 (2001).
67. N. P. Barnes, M. E. Storm, P. L. Cross, and M. W. Skolaut, "Efficiency of Nd Laser Materials with Laser Diode Pumping," IEEE J. Quantum Electron. **26**(3), 558–569 (1990).
68. F. Chen, J. Sun, R. Yan, and X. Yu, "Reabsorption cross section of Nd^{3+}-doped quasi-three-level lasers," Sci. Reports 2019 91 **9**(1), 1–8 (2019).
69. L. F. Johnson, "Optical Maser Characteristics of Rare-Earth Ions in Crystals," J. Appl. Phys.

34(4), 897–909 (1963).
70. J. A. Cairo, L. G. Deshazer, and J. Nella, "Characteristics of Room-Temperature 2.3-μm Laser Emission from Tm^{3+} in YAG and $YAlO_3$," IEEE J. Quantum Electron. **11**(11), 874–881 (1975).
71. P. F. Moulton, "Spectroscopic and laser characteristics of Ti:Al_2O_3," JOSA B, **3**(1), 125–133 (1986).
72. Y. Tang, J. Xu, Y. Tang, and J. Xu, "High Power Tunable Tm^{3+}-fiber Lasers and Its Application in Pumping Cr^{2+}:ZnSe Lasers," Front. Guid. Wave Opt. Optoelectron. (2010).
73. H. Yang, J. Zhang, D. Luo, H. Lin, H. Chen, D. Shen, and D. Tang, "Optical properties and laser performance of Ho:LuAG ceramics," Phys. status solidi c **10**(6), 903–906 (2013).
74. E. P. Chicklis, C. S. Naiman, R. C. Folweiler, D. R. Gabbe, H. P. Jenssen, and A. Linz, "High-Efficiency Room-Temperature 2.06-μm Laser Using Sensitized Ho^{3+}:YLF," Appl. Phys. Lett. **19**(4), 119–121 (1971).
75. K. Scholle, S. Lamrini, P. Koopmann, P. Fuhrberg, K. Scholle, S. Lamrini, P. Koopmann, and P. Fuhrberg, "2 μm Laser Sources and Their Possible Applications," Front. Guid. Wave Opt. Optoelectron. (2010).
76. A. A. Lagatsky, F. Fusari, S. V. Kurilchik, V. E. Kisel, A. S. Yasukevich, N. V. Kuleshov, A. A. Pavlyuk, C. T. A. Brown, and W. Sibbett, "Optical spectroscopy and efficient continuous-wave operation near 2 μm for a Tm,Ho:KYW laser crystal," Appl. Phys. B Lasers Opt. **97**(2), 321–326 (2009).
77. E. W. Barrera, M. C. Pujol, J. J. Carvajal, X. Mateos, R. Solé, J. Massons, A. Speghini, M. Bettinelli, C. Cascales, M. Aguiló, and F. Díaz, "White light upconversion in Yb-sensitized (Tm, Ho)-doped $KLu(WO_4)_2$ nanocrystals: the effect of Eu incorporation," Phys. Chem. Chem. Phys. **16**(4), 1679–1686 (2013).
78. F. Díaz, N. Kuleshov, U. Griebner, X. Mateos, P. Loiko, J. M. Serres, K. Yumashev, M. Aguiló, and V. Petrov, "Microchip laser operation of Tm,Ho:$KLu(WO_4)_2$ crystal," Opt. Express, **22**(23), 27976–27984 (2014).
79. S. Y. Choi, I. Buchvarov, M. H. Kim, F. Díaz, U. Griebner, F. Rotermund, X. Mateos, V. Aleksandrov, A. Gluth, and V. Petrov, "Tm,Ho:$KLu(WO_4)_2$ laser mode-locked near 2 μm by single-walled carbon nanotubes," Opt. Express, **22**(22), 26872–26877 (2014).
80. F. Fusari, A. A. Lagatsky, M. D. Dawson, S. Calvez, C. T. A. Brown, W. Sibbett, V. E. Kisel, N. V. Kuleshov, and S. V. Kurilchik, "Femtosecond pulse operation of a Tm,Ho-codoped crystalline laser near 2 μm," Opt. Lett. **35**(2), 172–174 (2010).
81. J. A. Gupta, A. A. Lagatsky, M. D. Dawson, S. Calvez, C. T. A. Brown, X. Han, M. D. Serrano, C. Zaldo, W. Sibbett, and C. Cascales, "Femtosecond (191 fs) $NaY(WO_4)_2$ Tm,Ho-codoped laser at 2060 nm," Opt. Lett. **35**(18), 3027–3029 (2010).
82. Z. Pan, X. Zhang, X. Mateos, A. Härkönen, S. Suomalainen, D. Shen, J. Xu, M. Guina, U. Griebner, Y. Zhao, P. Loiko, X. Xu, Y. Wang, W. Zhou, and V. Petrov, "87 fs mode-locked Tm,Ho:$CaYAlO_4$ laser at ~2043 nm," Opt. Lett. **43**(4), 915–918 (2018).
83. Y. Zhang, J. E. Bae, Z. Pan, S. Y. Choi, J. Sotor, F. Rotermund, X. Mateos, H. Yuan, J. M. Serres, U. Griebner, Y. Zhao, P. Loiko, X. Dai, H. Cai, Y. Wang, M. Kowalczyk, and V. Petrov, "Sub-80 fs mode-locked Tm,Ho-codoped disordered garnet crystal oscillator operating at 2081 nm," Opt. Lett. **43**(20), 5154–5157 (2018).
84. Y. Zhang, J. E. Bae, Z. Pan, S. Y. Choi, W. Chen, F. Rotermund, X. Mateos, H. Yuan, J. M. Serres, D. Shen, U. Griebner, Y. Zhao, P. Loiko, L. Wang, X. Dai, H. Cai, Y. Wang, W. Zhou, and V. Petrov, "67-fs pulse generation from a mode-locked Tm,Ho:CLNGG laser at 2083 nm," Opt. Express, **27**(3), 1922–1928 (2019).
85. I. F. Elder and M. J. P. Payne, "Lasing in diode-pumped Tm:YAP, Tm,Ho:YAP and Tm,Ho:YLF," Opt. Commun. **145**(1–6), 329–339 (1998).
86. F. Díaz, N. Kuleshov, U. Griebner, X. Mateos, P. Loiko, J. M. Serres, K. Yumashev, M. Aguiló, and V. Petrov, "Microchip laser operation of Tm,Ho:$KLu(WO_4)_2$ crystal," Opt. Express, **22**(23), 27976–27984 (2014).
87. T. H. Maiman, "Stimulated Optical Radiation in Ruby," Nat. 1960 1874736 **187**(4736), 493–494 (1960).
88. H. Bruesselbach and D. S. Sumida, "A 2.65-kW Yb: YAG single-rod laser," IEEE J. Sel. Top.

Quantum Electron. **11**(3), 600–603 (2005).
89. S. J. McNaught, H. Komine, S. Benjamin Weiss, R. Simpson, A. M. F. Johnson, J. Machan, C. P. Asman, M. Weber, G. C. Jones, M. M. Valley, A. Jankevics, D. Burchman, M. McClellan, J. Sollee, J. Marmo, and H. Injeyan, "100 kW Coherently Combined Slab MOPAs," Conf. Lasers Electro-Optics/International Quantum Electron. Conf. (2009), Pap. CThA1 CThA1 (2009).
90. G. Huber, C. Kränkel, and K. Petermann, "Solid-state lasers: status and future [Invited]," JOSA B, **27**(11), B93–B105 (2010).
91. A. Giesen, H. Hügel, A. Voss, K. Wittig, U. Brauch, and H. Opower, "Scalable concept for diode-pumped high-power solid-state lasers," Appl. Phys. B Lasers Opt. **58**(5), 365–372 (1994).
92. G. Huber, C. Kränkel, and K. Petermann, "Solid-state lasers: status and future [Invited]," JOSA B, **27**(11), B93–B105 (2010).
93. M. Eilchi, P. Parvin, M. Eilchi, and P. Parvin, "Gain Saturation in Optical Fiber Laser Amplifiers," Fiber Laser (2016).
94. M. Dammak, R. Maalej, M. Kamoun, and J. L. Deschanvres, "Crystal field analysis of erbium doped yttrium oxide thin films in C2 and C3i sites," Phys. status solidi **239**(1), 193–202 (2003).
95. P. O. Petit, P. Goldner, B. Viana, J. Boudeile, J. Didierjean, F. Balembois, F. Druon, and P. Georges, "Diode pumping of Yb^{3+}:$CaGdAlO_4$," Proc. SPIE, Solid State Lasers and Amplifiers III, **69980Z**, 248–253 (2008).
96. S. E. Sarkisov, V. A. Yusim, and Y. V. Pisarevsky, "Study of the Formation of Radiation-Stimulated Impurity Defects in CaF2 Crystals Activated by Trivalent Rare-Earth Ions," Crystallogr. Reports **68**(1), 79–87 (2023).
97. U. Demirbas, M. Kellert, J. Thesinga, Y. Hua, S. Reuter, F. X. Kärtner, and M. Pergament, "Comparative investigation of lasing and amplification performance in cryogenic Yb:YLF systems," Appl. Phys. B Lasers Opt. **127**(3), 1–10 (2021).
98. T. Y. Fan, D. J. Ripin, R. L. Aggarwal, J. R. Ochoa, B. Chann, M. Tilleman, and J. Spitzberg, "Cryogenic Yb^{3+}-doped solid-state lasers," IEEE J. Sel. Top. Quantum Electron. **13**(3), 448–458 (2007).
99. Y. P. Podmar'kov, N. A. Raspopov, A. N. Savchenko, and M. P. Frolov, " Dynamics of the intracavity absorption in the spectrum of a Co:MgF_2 laser emitting for up to 1 ms ," Quantum Electron. **29**(3), 223–225 (1999).
100. T. J. Carrig, "Transition-metal-doped chalcogenide lasers," J. Electron. Mater. **31**(7), 759–769 (2002).
101. S. Slimi, V. Jambunathan, G. Zin Elabedine, H. Yu, H. Zhang, W. Chen, R. Maria Solé, M. Aguiló, F. Díaz, M. Smrz, T. Mocek, and X. Mateos, "Spectroscopic and lasing characteristics of Yb:YGG at cryogenic temperatures," Opt. Laser Technol. **167**, 109713 (2023).
102. Z. Song, Z. Xia, and Q. Liu, "Insight into the Relationship between Crystal Structure and Crystal-Field Splitting of Ce^{3+} Doped Garnet Compounds," J. Phys. Chem. C **122**(6), 3567–3574 (2018).
103. C. Liu, Z. Xia, M. S. Molokeev, and Q. Liu, "Synthesis, Crystal Structure, and Enhanced Luminescence of Garnet-Type $Ca_3Ga_2Ge_3O_{12}$:Cr^{3+} by Codoping Bi^{3+}," J. Am. Ceram. Soc. **98**(6), 1870–1876 (2015).
104. Z. Pan, P. Loiko, Y. Wang, Y. Zhao, H. Yuan, K. Tang, X. Dai, H. Cai, J. M. Serres, S. Slimi, E. Ben Salem, E. Dunina, A. Kornienko, L. Fomicheva, J. L. Doualan, P. Camy, W. Chen, U. Griebner, V. Petrov, M. Aguiló, F. Díaz, R. M. Solé, and X. Mateos, "Disordered Tm^{3+},Ho^{3+}-codoped CNGG garnet crystal: Towards efficient laser materials for ultrashort pulse generation at ~2 μm," J. Alloys Compd. **853**, 157100 (2021).
105. E. Castellano-Hernández, M. D. Serrano, R. J. Jiménez Riobóo, C. Cascales, C. Zaldo, A. Jezowski, and P. A. Loiko, "Na Modification of Lanthanide Doped $Ca_3Nb_{1.5}Ga_{3.5}O_{12}$-Type Laser Garnets: Czochralski Crystal Growth and Characterization," Cryst. Growth Des. **16**(3), 1480–1491 (2016).
106. T. Wu, L. Wang, Y. Shi, T. Xu, H. Wang, J. Fang, J. Ni, H. He, C. Wang, B. Wan, D. Ding, Z. Zhou, Q. Liu, Q. Li, J. Yu, X. Huang, O. Shichalin, and E. K. Papynov, "Fast $(Ce,Gd)_3Ga_2Al_3O_{12}$ Scintillators Grown by the Optical Floating Zone Method," Cryst. Growth Des. **22**(1), 180–190 (2022).

107. X. Li, K. Eremeev, P. Loiko, Y. Zhou, Y. Zhang, J. Liu, Z. Pan, A. Braud, J. L. Doualan, S. Slimi, R. M. Solé, X. Mateos, P. Camy, and H. Xu, "Spectroscopy of Yb^{3+},Ho^{3+},Eu^{3+}-codoped calcium niobium gallium garnet (CNGG) crystal," Opt. Mater. (Amst). **144**, 114360 (2023).
108. Z. Han, D. Sun, H. Zhang, J. Luo, C. Quan, L. Hu, K. Dong, M. Cheng, G. Chen, and Y. Hang, "Investigation on the Growth and Properties of Six Garnet Single Crystals with Large Lattice Constants," Cryst. Res. Technol. **56**(5), 2000221 (2021).
109. Z. Han, D. Sun, H. Zhang, J. Luo, C. Quan, L. Hu, K. Dong, M. Cheng, G. Chen, and Y. Hang, "Investigation on the Growth and Properties of Six Garnet Single Crystals with Large Lattice Constants," Cryst. Res. Technol. **56**(5), 2000221 (2021).
110. E. Castellano-Hernández, M. D. Serrano, R. J. Jiménez Riobóo, C. Cascales, C. Zaldo, A. Jezowski, and P. A. Loiko, "Na Modification of Lanthanide Doped $Ca_3Nb_{1.5}Ga_{3.5}O_{12}$-Type Laser Garnets: Czochralski Crystal Growth and Characterization," Cryst. Growth Des. **16**(3), 1480–1491 (2016).
111. M. Kubiak, W. Piekarska, and S. Stano, "Modelling of laser beam heat source based on experimental research of Yb:YAG laser power distribution," Int. J. Heat Mass Transf. **83**, 679–689 (2015).
112. P. V. Klevtsov and R. F. Klevtsova, "Polymorphism of the double molybdates and tungstates of mono- and trivalent metals with the composition $M^+R^{3+}(EO_4)_2$," J. Struct. Chem. **18**(3), 339–355 (1977).
113. J. M. Cano-Torres, M. Rico, X. Han, M. D. Serrano, C. Cascales, C. Zaldo, V. Petrov, U. Griebner, X. Mateos, P. Koopmann, and C. Kränkel, "Comparative study of crystallographic, spectroscopic, and laser properties of Tm^{3+} in $NaT(WO_4)_2$ (T=La, Gd, Y, and Lu) disordered single crystals," Phys. Rev. B - Condens. Matter Mater. Phys. **84**(17), 174207 (2011).
114. V. Petrov, M. C. Pujol, X. Mateos, Ò. Silvestre, S. Rivier, M. Aguiló, R. M. Solé, J. Liu, U. Griebner, and F. Díaz, "Growth and properties of $KLu(WO_4)_2$, and novel ytterbium and thulium lasers based on this monoclinic crystalline host," Laser Photon. Rev. **1**(2), 179–212 (2007).
115. T. T. Basiev, A. A. Sobol, Y. K. Voronko, and P. G. Zverev, "Spontaneous Raman spectroscopy of tungstate and molybdate crystals for Raman lasers," Opt. Mater. (Amst). **15**(3), 205–216 (2000).
116. X. Mateos, P. Loiko, J. M. Serres, K. Yumashev, U. Griebner, V. Petrov, M. Aguiló, and F. Díaz, "Efficient Micro-Lasers Based on Highly Doped Monoclinic Double Tungstates," IEEE J. Quantum Electron. **53**(3), (2017).
117. A. Volokitina, P. Loiko, E. Vilejshikova, X. Mateos, E. Dunina, A. Kornienko, N. Kuleshov, and A. Pavlyuk, "Eu^{3+}:$KY(MoO_4)_2$: A novel anisotropic red-emitting material with a layered structure," J. Alloys Compd. **762**, 786–796 (2018).
118. Q. Tan, Y. Lin, X. Gong, Y. Huang, Z. Luo, and Y. Chen, "Polarized spectral characteristics of Nd^{3+}:$KY(MoO_4)_2$ crystal with perfect cleavage planes: a promising microchip gain medium," JOSA B, **24**(3), 496–503 (2007).
119. J. Zhang, X. Wang, X. Zhang, X. Zhao, X. Liu, and L. Peng, "Microwave synthesis of $NaLa(MoO_4)_2$ microcrystals and their near-infrared luminescent properties with lanthanide ion doping (Er^{3+}, Nd^{3+}, Yb^{3+})," Inorg. Chem. Commun. **14**(11), 1723–1727 (2011).
120. Y. Wei, C. Su, H. Zhang, J. Shao, and Z. Fu, "Thermal sensor and optical heater of upconversion phosphor: Yb^{3+}/Er^{3+} co-doped $KY(MoO_4)_2$," Phys. B Condens. Matter **525**, 149–153 (2017).
121. W. Guo, Y. Lin, X. Gong, Y. Chen, Z. Luo, and Y. Huang, "Spectroscopic properties of Pr^{3+}:$KY(MoO_4)_2$ crystal as a visible laser gain medium," J. Phys. Chem. Solids **69**(1), 8–15 (2008).
122. J. Hanuza, L. Macalik, W. Ryba-Romanowski, E. Mugeński, R. Cywiński, K. Witke, W. Piltz, and P. Reich, "Physicochemical properties of Dy^{3+} in single $KY(MoO_4)_2$ crystal (electron absorption, emission, IR, Raman, and magnetic data)," J. Solid State Chem. **73**(2), 488–501 (1988).
123. P. Loiko, A. Pavlyuk, S. Slimi, R. M. Solé, E. Ben Salem, E. Dunina, A. Kornienko, P. Camy, U. Griebner, V. Petrov, F. Díaz, M. Aguiló, and X. Mateos, "Growth, spectroscopy and laser operation of monoclinic Nd:$CsGd(MoO_4)_2$ crystal with a layered structure," J. Lumin. **231**,

117793 (2021).
124. V. I. Kut'ko, "Dynamics of layered Jahn–Teller crystals of rare-earth compounds (Review)," Low Temp. Phys. **31**(1), 1–31 (2005).
125. N. V Ivannikova, L. P. Kozeeva, and A. A. Pavlyuk, "Solubility and growth of $CsGd(MoO_4)_2$ single crystals," Inorg. Mater. (Engl. Transl.); (United States) **24:3**, (1988).
126. A. A. Pavlyuk, L. I. Kozeeva, K. G. Folin, V. G. Gladyshev, V. S. Gulyaev, V. S. Pivtsov, A. A. Kaminskij, N. I. A. i E. AN SSSR, and M. I. K. AN SSSR, "Generation of stimulated radiation at the $^4F_{3/2}$ yields $^4I_{11/2}$ transition of Nd^{3+} ions in $RbNd(WO_4)_2$ and $CsNd(MoO_4)_2$," Izv. Akad. Nauk SSSR, Neorg. Mater.; **19:5**, (1983).
127. W. Zhao, Y. S. Huang, Z. Bin Lin, B. Wei, F. W. Wang, M. Xu, X. Zhao, Q. H. Zheng, and W. W. Zhou, "Spectra and energy levels of a layered Yb^{3+}:$CsGd(MoO_4)_2$ crystal with perfect cleavage: a candidate for microchip lasers," RSC Adv. **5**(44), 34730–34736 (2015).
128. L. V. Gudzenko, M. B. Kosmyna, A. N. Shekhovtsov, W. Paszkowicz, A. Sulich, J. Z. Domagała, P. A. Popov, and S. A. Skrobov, "Crystal Growth and Glass-Like Thermal Conductivity of $Ca_3RE_2(BO_3)_4$ (RE = Y, Gd, Nd) Single Crystals," Cryst. 2017, Vol. 7, Page 88 **7**(3), 88 (2017).
129. K. M. Kosyl, W. Paszkowicz, R. Minikayev, A. N. Shekhovtsov, M. B. Kosmyna, M. Chrunik, and A. N. Fitch, "Site-occupancy scheme in disordered $Ca3RE_2(BO_3)_4$: A dependence on rare-earth (RE) ionic radius," Acta Crystallogr. Sect. B Struct. Sci. Cryst. Eng. Mater. **77**(3), 307–308 (2021).
130. Y. Xiao, M. Ju, H. Yuan, and Y. Yeung, "Unveiling the Local Structure and Luminescence Mechanism of Er^{3+}-Doped $LiYF_4$: A Promising Near-Infrared Laser Crystal," J. Phys. Chem. C **125**(32), 18015–18021 (2021).
131. I. M. Ranieri, L. C. Courrol, A. F. Carvalho, L. Gomes, and S. L. Baldochi, "Growth of YLF:Yb:Tm:Nd for optical applications," J. Mater. Sci. **42**(7), 2309–2313 (2007).
132. R. L. Aggarwal, D. J. Ripin, J. R. Ochoa, and T. Y. Fan, "Thermo-optic properties of laser crystals in the 100-300 K temperature range: $Y_3Al_5O_{12}$ (YAG), $YAlO_3$ (YALO) and $LiYF_4$ (YLF)," Proc. SPIE, Solid State Lasers XIV: Technology and Devices **5707**, 165–170 (2005).
133. B.-Q. Yao, P.-B. Meng, Y.-L. Ju, G. Li, and Y.-Z. Wang, "Comparison of Tm:YLF and Tm:YAP in thermal analysis and laser performance," JOSA B, **28**(8), 1866–1873 (2011).
134. S. S. Dossa and J. J. Derby, "Modeling optical floating zone crystal growth in a high-pressure, single-lamp furnace," J. Cryst. Growth **591**, 126723 (2022).
135. P. Ramesh Babu, I. Bhaumik, S. Ganesamoorthy, S. Kalainathan, R. Bhatt, A. K. Karnal, and P. K. Gupta, "Investigation of magnetic property of $GdFeO_3$ single crystal grown in air by optical floating zone technique," J. Alloys Compd. **631**, 232–236 (2015).
136. F. Rey-García, R. Ibáñez, L. A. Angurel, F. M. Costa, and G. F. d. la Fuente, "Laser Floating Zone Growth: Overview, Singular Materials, Broad Applications, and Future Perspectives," Cryst. **11**(1), 38 (2020).
137. S. M. Koohpayeh, D. Fort, and J. S. Abell, "The optical floating zone technique: A review of experimental procedures with special reference to oxides," Prog. Cryst. Growth Charact. Mater. **54**(3–4), 121–137 (2008).
138. J. L. Schmehr, M. Aling, E. Zoghlin, and S. D. Wilson, "High-pressure laser floating zone furnace," Rev. Sci. Instrum. **90**(4), 43906 (2019).
139. P. Gille and Y. Grin, "Crystal growth of intermetallics," Cryst. Growth Intermet. 1–282 (2018).
140. F. Rey-García, R. Ibáñez, L. A. Angurel, F. M. Costa, and G. F. d. la Fuente, "Laser Floating Zone Growth: Overview, Singular Materials, Broad Applications, and Future Perspectives," Cryst. **11**(1), 38 (2020).
141. H. A. Dabkowska and A. B. Dabkowski, "Crystal Growth of Oxides by Optical Floating Zone Technique," Springer Handb. Cryst. Growth 367–391 (2010).
142. H. A. Dabkowska, A. B. Dabkowski, R. Hermann, J. Priede, and G. Gerbeth, "Floating Zone Growth of Oxides and Metallic Alloys," Handb. Cryst. Growth Bulk Cryst. Growth Second Ed. **2**, 281–329 (2015).
143. G. Müller, "The Czochralski Method - where we are 90 years after Jan Czochralski's invention," Cryst. Res. Technol. **42**(12), 1150–1161 (2007).
144. C. D. Brandle, "Czochralski growth of oxides," J. Cryst. Growth **264**(4), 593–604 (2004).

145. M. Vegad and N. M. Bhatt, "Review of some Aspects of Single Crystal Growth Using Czochralski Crystal Growth Technique," Procedia Technol. **14**, 438–446 (2014).
146. "Crystal Growth Technology," Cryst. Growth Technol. (2003).
147. A. Yoshikawa, V. Chani, and M. Nikl, "Czochralski Growth and Properties of Scintillating Crystals," Zesz. Hist. Politech. Warsz. (z. 16), 135--149 (2014).
148. I. Tupitsyna, A. Dubovik, A. Yakubovskaya, P. Mateychenko, V. Baumer, K. Brylyova, T. Sheina, O. Hryshyna, S. Pirro, S. S. Nagorny, and S. Nisi, "Growth of samarium doped zinc tungstate crystals by the Czochralski method," J. Cryst. Growth **586**, 126632 (2022).
149. N. Sarukura, T. Nawata, H. Ishibashi, M. Ishii, and T. Fukuda, "Czochralski Growth of Oxides and Fluorides," Handb. Cryst. Growth Bulk Cryst. Growth Second Ed. **2**, 131–168 (2015).
150. P. H. Haumesser, R. Gaumé, J. M. Benitez, B. Viana, B. Ferrand, G. Aka, and D. Vivien, "Czochralski growth of six Yb-doped double borate and silicate laser materials," J. Cryst. Growth **233**(1–2), 233–242 (2001).
151. L. Gheorghe, V. Lupei, A. Lupei, C. Gheorghe, C. Varona, P. Loiseau, G. Aka, D. Vivien, and B. Ferrand, "Czochralski growth and characterization of neodymium-doped strontium lanthanum aluminate (ASL:Nd) single crystals," J. Cryst. Growth **277**(1–4), 410–415 (2005).
152. V. N. Shlegel, Y. A. Borovlev, D. N. Grigoriev, V. D. Grigorieva, F. A. Danevich, N. V. Ivannikova, A. G. Postupaeva, and Y. V. Vasiliev, "Recent progress in oxide scintillation crystals development by low-thermal gradient Czochralski technique for particle physics experiments," J. Instrum. **12**(08), C08011 (2017).
153. E. M. Trukhanov, K. B. Fritzler, A. P. Vasilenko, A. V. Kolesnikov, P. V. Kasimkin, and V. A. Moskovskih, "Dislocation structure of Ge crystals grown by low thermal gradient Czochralski technique," J. Cryst. Growth **468**, 457–461 (2017).
154. Y. A. Borovlev, N. V. Ivannikova, V. N. Shlegel, Y. V. Vasiliev, and V. A. Gusev, "Progress in growth of large sized BGO crystals by the low-thermal-gradient Czochralski technique," J. Cryst. Growth **229**(1–4), 305–311 (2001).
155. M. Prochazka, "Basics of Raman Scattering (RS) Spectroscopy," 7–19 (2016).
156. H. Abitan, H. Bohr, and P. Buchhave, "Correction to the Beer-Lambert-Bouguer law for optical absorption," Appl. Opt. **47**(29), 5354–5357 (2008).
157. V. V. OVSYANKIN, "Spectroscopy of Collective States and Cooperative Transitions in Disordered Rare-Earth Activated Solids," **21**, 343–480 (1987).
158. G. S. Opelt, "Intensities of Crystal Spectra of Rare-Earth Ions," J. Chem. Phys. **37**(3), 511–520 (1962).
159. B. R. Judd, "Optical Absorption Intensities of Rare-Earth Ions," Phys. Rev. **127**(3), 750 (1962).
160. H. Canibano, A. Ródenas, D. Jaque, A. G. Petrosyan, G. Boulon, Y. Guyot, A. Brenier, and A. Eganyan, "Growth, spectroscopic, and laser properties of Yb^{3+}-doped $Lu_3Al_5O_{12}$ garnet crystal," JOSA B, **23**(4), 676–683 (2006).

List Of Publications

1. List of journal publications related to this thesis

The findings presented in this thesis are drawn from the following peer-reviewed journal articles. The listed of the papers related to this thesis is shown below. Due to copyright regulations, the publications can be accessed directly from the respective journals' websites using the mentioned DOI link.

Paper 1
Status: Published
S. Slimi, P. Loiko, M. Pan, P. Lehoux, V. Jambunathan, M. Smrz, T. Mocek, Y. Wang, W. Chen, V. Petrov, R.M. Solé, M. Aguiló, F. Díaz, P. Camy, X. Mateos, *"Growth, Structure, Spectroscopy, and Laser Operation of a "Mixed" Yb:$(Y,Lu)_3Al_5O_{12}$ Garnet Crystal"*, Cryst. 13 (2023) 1588.
DOI: https://doi.org/10.3390/CRYST13111588.

Paper 2
Status: Published
A. Volokitina, A. Volokitina, P. Loiko, A. Pavlyuk, J.M. Serres, **S. Slimi**, E. Ben Salem, E. Kifle, U. Griebner, V. Petrov, L. Wang, W. Chen, R.M. Solé, M. Aguiló, F. Díaz, X. Mateos, *"Spectroscopy and efficient laser operation of cleaving Yb:$KY(MoO_4)_2$ crystal"*, Opt. Mater. Express, 10 (2020) 2356–2369.
DOI: https://doi.org/10.1364/OME.400894.

Paper 3
Status: Published
Z. Pan, Z. Pan, Z.-L. Lin, P. Loiko, G. Zhang, H.-J. Zeng, W.-Z. Xue, P. Camy, V. Petrov, **S. Slimi**, X. Mateos, F. Díaz, H. Lin, L. Wang, W. Chen, W. Chen, *"Polarized spectroscopy and diode-pumped laser operation of disordered Yb:$Ca_3Gd_2(BO_3)_4$ crystal"*, Opt. Mater. Express, 12 (2022) 673–684.
DOI: https://doi.org/10.1364/OME.449829.

Paper 4
Status: Published
S. Slimi, V. Jambunathan, G. Zin Elabedine, H. Yu, H. Zhang, W. Chen, R. Maria Solé, M. Aguiló, F. Díaz, M. Smrz, T. Mocek, X. Mateos, *"Spectroscopic and lasing characteristics of Yb:YGG at cryogenic temperatures"*, Opt. Laser Technol. 167 (2023) 109713.
DOI: https://doi.org/10.1016/J.OPTLASTEC.2023.109713.

Paper 5
Status: Published
S. Slimi, V. Jambunathan, M. Pan, Y. Wang, W. Chen, P. Loiko, R.M. Solé, M. Aguiló, F. Díaz, M. Smrz, T. Mocek, X. Mateos, *"Cryogenic laser operation of a "mixed" Yb:LuYAG garnet crystal"*, Appl. Phys. B Lasers Opt. 129 (2023) 1–7.
DOI: https://doi.org/10.1007/S00340-023-07999-9/TABLES/1.

Paper 6
Status: Published
P. Loiko, A. Pavlyuk, **S. Slimi**, R.M. Solé, E. Ben Salem, E. Dunina, A. Kornienko, P. Camy, U. Griebner, V. Petrov, F. Díaz, M. Aguiló, X. Mateos, *"Growth, spectroscopy and laser operation of monoclinic Nd:$CsGd(MoO_4)_2$ crystal with a layered structure"*, J. Lumin. 231 (2021) 117793.
DOI: https://doi.org/10.1016/J.JLUMIN.2020.117793.

Paper 7
Status: Published
P. Loiko, A. Volokitina, J.M. Serres, V. Trifonov, A. Pavlyuk, **S. Slimi**, E. Ben Salem, R.M. Sol, M. Aguil, F. Diáz, X. Mateos, *"Laser operation of cleaved single-crystal plates and films of Tm:$KY(MoO_4)_2$"*, Opt. Express, 28 (2020) 9039–9048.

DOI: https://doi.org/10.1364/OE.384260.

Paper 8
Status: Published
A. Alles, Z. Pan, P. Loiko, J.M. Serres, **S. Slimi**, S. Yingming, K. Tang, Y. Wang, Y. Zhao, E. Dunina, A. Kornienko, P. Camy, W. Chen, L. Wang, U. Griebner, V. Petrov, R.M. Solé, M. Aguiló, F. Díaz, X. Mateos, *"Tm^{3+}-doped calcium lithium tantalum gallium garnet (Tm:CLTGG): novel laser crystal"*, Opt. Mater. Express, 11 (2021) 2938–2951.
DOI: https://doi.org/10.1364/OME.435238.

Paper 9
Status: Published
Z. Pan, P. Loiko, Y. Wang, Y. Zhao, H. Yuan, K. Tang, X. Dai, H. Cai, J.M. Serres, **S. Slimi**, E. Ben Salem, E. Dunina, A. Kornienko, L. Fomicheva, J.L. Doualan, P. Camy, W. Chen, U. Griebner, V. Petrov, M. Aguiló, F. Díaz, R.M. Solé, X. Mateos, *"Disordered Tm^{3+},Ho^{3+}-codoped CNGG garnet crystal: Towards efficient laser materials for ultrashort pulse generation at ~2 μm"*, J. Alloys Compd. 853 (2021) 157100.
DOI: https://doi.org/10.1016/J.JALLCOM.2020.157100.

Paper 10
Status: Published
A. Alles, V. Jambunathan, **S. Slimi**, J.M. Serres, M. Aguiló, F. Díaz, X. Mateos, M. Smrz, T. Mocek, *"Cryogenic Tm:$LiYF_4$ laser around 2 μm"*, Appl. Phys. B Lasers Opt. 129 (2023) 1–5.
DOI: https://doi.org/10.1007/S00340-023-07970-8/FIGURES/4.

2. List of secondary journal publications

Paper 11
Status: Published
X. Li, K. Eremeev, P. Loiko, Y. Zhou, Y. Zhang, J. Liu, Z. Pan, A. Braud, J.L. Doualan, **S. Slimi**, R.M. Solé, X. Mateos, P. Camy, H. Xu, *"Spectroscopy of Yb^{3+},Ho^{3+},Eu^{3+}-codoped calcium niobium gallium garnet (CNGG) crystal"*, Opt. Mater. (Amst). 144 (2023) 114360.
DOI: https://doi.org/10.1016/J.OPTMAT.2023.114360.

Paper 12
Status: Published
L. Zhang, L. Basyrova, P. Loiko, P. Camy, Z. Lin, G. Zhang, **S. Slimi**, R.M. Solé, X. Mateos, M. Aguiló, F. Díaz, E. Dunina, A. Kornienko, U. Griebner, V. Petrov, L. Wang, W. Chen, W. Chen, *"Growth, structure, and polarized spectroscopy of monoclinic Er^{3+}:$MgWO_4$ crystal"*, Opt. Mater. Express, 12 (2022) 2028–2040.
DOI: https://doi.org/10.1364/OME.449649.

Paper 13
Status: Published
Z. Pan, P. Loiko, **S. Slimi**, H. Yuan, Y. Wang, Y. Zhao, P. Camy, E. Dunina, A. Kornienko, L. Fomicheva, L. Wang, W. Chen, U. Griebner, V. Petrov, R.M. Solé, F. Díaz, M. Aguiló, X. Mateos, *"Tm,Ho:Ca(Gd,Lu)AlO_4 crystals: Crystal growth, structure refinement and Judd-Ofelt analysis"*, J. Lumin. 246 (2022) 118828.
DOI: https://doi.org/10.1016/J.JLUMIN.2022.118828.

Paper 14
Status: Published

K. Subbotin, P. Loiko, **S. Slimi**, A. Volokitina, A. Titov, D. Lis, E. Chernova, S. Kuznetsov, R.M. Solé, U. Griebner, V. Petrov, M. Aguiló, F. Díaz, P. Camy, E. Zharikov, X. Mateos, *"Monoclinic zinc monotungstate Yb^{3+},Li^{+}:$ZnWO_4$: Part I. Czochralski growth, structure refinement and Raman spectra"*, J. Lumin. 228 (2020) 117601.
DOI: https://doi.org/10.1016/J.JLUMIN.2020.117601.

Paper 15
Status: Published
S. Slimi, P. Loiko, K. Bogdanov, A. Volokitina, R.M. Solé, M. Aguiló, F. Díaz, E. Ben Salem, X. Mateos, *"Structure and luminescent properties of Dy^{3+} activated $NaLa_9(SiO_4)_6O_2$ yellow-emitting phosphors for application in white LEDs"*, J. Alloys Compd. 896 (2022) 163109.
DOI: https://doi.org/10.1016/J.JALLCOM.2021.163109.

Paper 16
Status: Published
S. Slimi, P. Loiko, A. Volokitina, K. Bogdanov, R.M. Solé, M. Aguiló, F. Díaz, E. Ben Salem, X. Mateos, *"Structure, optical properties and preferential site substitution of Eu^{3+} activated $Ca_8NaBi(PO_4)_6F_2$ red emitting phosphors prepared by modified Pechini process"*, J. Lumin. 241 (2022) 118523.
DOI: https://doi.org/10.1016/J.JLUMIN.2021.118523.

Paper 17
Status: Published
A. Badri, **S. Slimi**, M. Guergueb, H. Kahri, X. Mateos, *"Green synthesis of copper oxide nanoparticles using Prickly Pear peel fruit extract: Characterization and catalytic activity"*, Inorg. Chem. Commun. 134 (2021) 109027.
DOI: https://doi.org/10.1016/J.INOCHE.2021.109027.

Paper 18
Status: Published
I. Mokni, A. Badri, **S. Slimi**, K. Omri, P. Loiko, R.M. Solé, M. Aguiló, F. Díaz, X. Mateos, M. Ben Amara, *"Synthesis and characterization of a novel alkali mixed magnesium-aluminum phosphate with a layered structure–$KMgAl(PO_4)_2$"*, J. Mol. Struct. 1248 (2022) 131535.
DOI: https://doi.org/10.1016/J.MOLSTRUC.2021.131535.

Paper 19
Status: Published
A. Badri, **S. Slimi**, I. Mokni, N. Dege, R. Maria Solé, M. Aguiló, F. Díaz, X. Mateos, M. Ben Amara, *"Synthesis, crystals structures and theoretical studies of novel alkali copper indium orthophosphates $ACuIn(PO_4)_2$ (A = Na, K and Rb)"*, J. Solid State Chem. 318 (2023) 123757.
DOI: https://doi.org/10.1016/J.JSSC.2022.123757.

Paper 20
Status: Published
M. Methamem, **S. Slimi**, I. Jendoubi, J.B.C. Castelló, M.F. Zid, X. Mateos, N.F. Bourguiba, *"Structural study, spectroscopic characterization, DFT calculations and electrical properties of manganese (II) organic-inorganic hybrid material $(C_8H_{14}N_2)_2[MnCl_4(H_2O)_2]Cl_2$"*, J. Mol. Struct. 1278 (2023) 134894.
DOI: https://doi.org/10.1016/J.MOLSTRUC.2022.134894.

Paper 21
Status: Published

A. Douzi, **S. Slimi**, E. Madirov, A. Turshatov, B.S. Richards, R.M. Solé, M. Aguiló, F. Díaz, E. Ben Salem, X. Mateos, *"Structure and luminescence properties of Dy^{3+} doped quaternary tungstate $Li_3Ba_2Gd_3(WO_4)_8$ for application in wLEDs"*, RSC Adv. 13 (2023) 23772–23787.
DOI: https://doi.org/10.1039/D3RA02501B.

Paper 22
Status: Published
Z. Zhang, A. Douzi, **S. Slimi**, E. Madirov, A. Arouri, V. Llamas, J. Maria Serres, R. Maria Solé, M. Aguiló, F. Díaz, E. Ben Salem, A. Turshatov, B.S. Richards, X. Mateos, *"Optical properties and Judd-Ofelt analysis of a novel Red-Emitting monoclinic $Li_3Ba_2Gd_3(WO4)_8$: Eu^{3+} phosphor"*, Inorg. Chem. Commun. 162 (2024) 112230.
DOI: https://doi.org/10.1016/J.INOCHE.2024.112230.

Paper 23
Status: Published
I. Mokni, **S. Slimi**, A. Badri, R. Maria Solé, M. Aguiló, F. Díaz, B. Ayed, X. Mateos, *"$Sr_6Y(PO_4)_5$: Nd^{3+} a novel whitlockite-type phosphor for optical temperature sensing applications: Synthesis and luminescence properties"*, Ceram. Int. 50 (2024) 22936–22946.
DOI: https://doi.org/10.1016/J.CERAMINT.2024.04.018.

Paper 24
Status: Published
A. Douzi, **S. Slimi**, P. Loiko, V. Llamas, J.M. Serres, R.M. Solé, M. Aguiló, F. Díaz, E. Ben Salem, X. Mateos, *"Temperature sensing by means of a near-infrared luminescent $Ca_8NaBi(PO_4)_6F_2$:Nd^{3+} fluorapatite phosphor"*, J. Mater. Sci. Mater. Electron. 35 (2024) 1–16.
DOI: https://doi.org/10.1007/S10854-024-12587-4/FIGURES/12.

Paper 25
Status: Submitted, under revision
S.Slimi, H.Yu, H.Zhang,C.Kränkel, P.Loiko, R..Solé, M.Aguiló, F.Díaz, W.Chen, U.Griebner, V.Petrov and X.Mateos, *"Growth, structure, spectroscopy, and laser operation of Ho-doped yttrium gallium garnet crystal"*.
Journal: Opt. Express (https://opg.optica.org/oe/home.cfm).

Paper 26
Status: Submitted, under revision
Z.Zhang, Y.Shen, **S.Slimi**, X.Mateos, S.Wang, *"Study on Photoluminescence Properties and Temperature Sensing of Pr^{3+}-Doped $Li_3Ba_2Gd_3(WO_4)_8$ Quaternary Tungstate"*.
Journal: Ceramics International (https://www.sciencedirect.com/journal/ceramics-international).

3. List of conference papers

Conference 01
Status: Published
S. Slimi, V. Jambunathan, G.Z. Elabedine, H. Yu, H. Zhang, W. Chen, R.M. Solé, M. Aguiló, F. Díaz, M. Smrz, T. Mocek, X. Mateos, Spectroscopy and Laser Operation of Yb:LuGG Crystal at Cryogenic temperatures, 2023 Conf. Lasers Electro-Optics Eur. Eur. Quantum Electron. Conf. CLEO/Europe-EQEC 2023. (2023).
DOI: https://doi.org/10.1109/CLEO/EUROPE-EQEC57999.2023.10231662.

Conference 02
Status: Published

G.Z. Elabedine, Z. Pan, P. Loiko, H. Chu, D. Li, A. Nady, K. Subbotin, S. Pavlov, P. Camy, A. Braud, **S. Slimi**, R.M. Solé, M. Aguiló, F. Díaz, W. Chen, V. Petrov, X. Mateos, Growth, Spectroscopy and Laser Operation of Disordered Tm,Ho:$NaGd(MoO_4)_2$ Crystal, Laser Congr. 2023 (ASSL, LAC), Pap. AW1A.4, (2023).
DOI: https://doi.org/10.1364/ASSL.2023.AW1A.4.

Conference 03
Status: Published
N.G. Boetti, D. Pugliese, M. Segura, **S. Slimi**, P. Loiko, G. Perrone, D. Janner, M. Ceballos, F. Diaz, M. Aguilo, X. Mateos, J. Lousteau, Dy^{3+}- and Pr^{3+}-doped phosphate glass optical fibres for laser emission at visible wavelengths, 2023 Conf. Lasers Electro-Optics Eur. Eur. Quantum Electron. Conf. CLEO/Europe-EQEC 2023. (2023).
DOI: https://doi.org/10.1109/CLEO/EUROPE-EQEC57999.2023.10231668.

Conference 04
Status: Published
D. Pugliese, M. Segura, N.G. Boetti, J. Lousteau, G. Perrone, D. Janner, **S. Slimi**, P.A. Loiko, M. Ceballos, X. Mateos, Dy^{3+}-doped phosphate glass optical fibers for 577 nm wavelength fiber lasers, Proceedings 12573, Specialty Optical Fibres (Conference Presentation); 125730A (2023).
DOI: https://doi.org/10.1117/12.2665269.

Conference 05
Status: Published
S. Slimi, V. Jambunathan, M. Pan, Y. Wang, W. Chen, P. Loiko, R.M. Solé, M. Aguiló, F. Díaz, M. Smrz, T. Mocek, X. Mateos, Spectroscopy and continuous-wave laser operation of Yb:YGG crystal at cryogenic temperatures, Opt. Adv. Photonics Congr. 2022 (2022), Pap. AM3A.5. (2022).
DOI: https://doi.org/10.1364/ASSL.2022.AM3A.5.

Conference 06
Status: Published
A. Volokitina, P. Loiko, A. Pavlyuk, **S. Slimi**, R.M. Sole, M. Aguilo, F. DIaz, X. Mateos, Growth and Polarized Spectroscopy of Red-Emitting Monoclinic Eu:$CsGd(MoO_4)_2$ Crystal with a Layered Structure, 2021 Conf. Lasers Electro-Optics Eur. Eur. Quantum Electron. Conf. CLEO/Europe-EQEC (2021).
DOI: https://doi.org/10.1109/CLEO/EUROPE-EQEC52157.2021.9542333.

Conference 07
Status: Published
L. Basyrova, P. Loiko, L. Zhang, Z. Lin, G. Zhang, **S. Slimi**, V. Petrov, U. Griebner, R.M. Solé, M. Aguiló, F. Díaz, P. Camy, X. Mateos, L. Wang, W. Chen, Polarized Spectroscopy and Eye-Safe Laser Operation of Monoclinic Er^{3+}:$MgWO_4$ Crystal, Laser Congr.2021, Pap. ATh1A.4. (2021).
DOI: https://doi.org/10.1364/ASSL.2021.ATH1A.4.

Conference 08
Status: Published
A.A. Volokitina, K.A. Subbotin, P.A. Loiko, A.I. Titov, D.A. Lis, **S. Slimi**, R.M. Sole, S.P. David, V. Jambunathan, A. Lucianetti, T. Mocek, U. Griebner, V. Petrov, M. Aguilo, F. Diaz, X. Mateos, E. Zharikov, Spectroscopic Study and First Laser Operation of Monoclinic Yb^{3+},Li^{+}:$ZnWO_4$ Crystal, Proc. - Int. Conf. Laser Opt. 2020, ICLO 2020. (2020).
DOI: https://doi.org/10.1109/ICLO48556.2020.9285913.

Conference 09
Status: Published

A. Volokitina, P. Loiko, A. Pavlyuk, J.M. Serres, **S. Slimi**, E. Ben Salem, R.M. Solé, M. Baranov, E. Kifle, M. Aguiló, F. Díaz, U. Griebner, V. Petrov, X. Mateos, Efficient laser operation in cleaved single-crystal plates of Yb:$KY(MoO_4)_2$: A novel molybdate compound, Proceedings Volume 11357, Fiber Lasers and Glass Photonics: Materials through Applications II; 113571T (2020).
DOI: https://doi.org/10.1117/12.2555416.

Conference 10
Status: Published
P. Loiko, A. Volokitina, J.M. Serres, V. Trifonov, A. Pavlyuk, **S. Slimi**, E. Ben Salem, R.M. Solé, M. Aguiló, F. Díaz, X. Mateos, Laser Operation of Cleaved Single-Crystal Plates and Films of Tm:$KY(MoO_4)_2$, Laser Congr. 2019 (ASSL, LAC, LS&C) (2019), Pap. JTu3A.38. Part F139-ASSL 2019 (2019).
DOI: https://doi.org/10.1364/ASSL.2019.JTU3A.38.

Conference 11
Status: Published
S. Slimi, V. Jambunathan, M. Pan, Y. Wang, W. Chen, P. Loiko, R.M. Solé, M. Aguiló, F. Díaz, M. Smrz, T. Mocek, X. Mateos, Y. Fan, D.J. Ripin, R. Aggarwal, J.R. Ochoa, B. Chann, M. Tilleman, Cryogenic Laser Operation of a "Mixed" Yb:YLuAG Garnet Crystal, EPJ Web Conf. 267-01033 (2022).
DOI: https://doi.org/10.1051/EPJCONF/202226701033.

UNIVERSITAT ROVIRA I VIRGILI
Novel infrared solid-state lasers based on lanthanide doped crystalline materials
SAMI SLIMI